SURFACE MICRO-DISCHARGE (SMD) - ANALYSIS OF THE ANTIMICROBIAL EFFECT AND THE PLASMA CHEMISTRY

Dissertation

der Fakultät für Physik

der Ludwig-Maximillians-Universität München

zur Erlangung des Grades eines

Doktors der Naturwissenschaften

vorgelegt von

Jin Jeon

geboren am 27. 09. 1984 in Seoul/Südkorea

München

2014

Erstgutachter : **Prof. Dr. Dr. h.c. Gregor Morfill**

Zweitgutachter : **Prof. Dr. Markus Thoma**

Datum der mündlichen Prüfung : **21.01.2015**

Abstract

There is an urgent need for an efficient technology of disinfection and sterilization in view of the alarming dimensions health care-associated infections (HAIs) have reached. Cold atmospheric pressure plasma (CAP) can be utilized for hygienic and medical purposes, in particular in surface decontamination applications, and provides a promising alternative to the conventionally used sterilization techniques. Surface Micro-Discharge (SMD) offers a technology for generating CAP that can be applied to wide areas.

In the present work, I investigate the plasma chemistry involved in the inactivation of microorganisms by application of the SMD in order to optimize the antimicrobial effect. For this purpose, different strains of vegetative bacteria and bacterial endospores are exposed to the SMD with experimental parameters such as the gas composition, power input, treatment duration and humidity varied. At the same time, the concentration of ozone produced by the SMD is monitored, and its correlation with the antimicrobial efficacy is investigated.

I demonstrate that the bactericidal effect of the SMD on both the Gram-negative *Escherichia coli* and Gram-positive *Enterococcus mundtii* is similar and strongly correlates with the ozone concentration. The sporicidal effect on *Geobacillus stearothermophilus* is crucially affected by the humidity, whereas the ozone concentration appears to have no influence. In addition, I investigate the dynamic behavior of ozone produced by the SMD by varying the geometry and the time interval for the plasma generation and by igniting the plasma in two subsequent phases with different frequencies. Possible explanations for the obtained results are provided.

This work fortifies the role of SMD as an efficient sterilization method and discloses diverse possibilities for optimizing the antimicrobial effect.

Acknowledgements

First of all, I would like to thank Prof. Gregor Morfill for his support and supervision. I have enjoyed being a member in his plasma healthcare group with its impressive nation- and worldwide network. I want to thank Prof. Markus Thoma and Dr. Julia Zimmermann for their support and readiness to help. I would like to express my heartfelt thanks to Dr. Tetsuji Shimizu, who helped me through tough situations and essentially contributed to my publications and this thesis. I want to thank Tobias Klämpfl for good discussions and for his support. Many thanks to all the colleagues from both plasma healthcare and complex plasmas groups for supporting me, especially Dr. Yangfang Li, Dr. Anindita Mitra, Dr. Wolfram Bunk, Bernd Steffes, Dr. Hans-Ulrich Schmidt, Tanja Rosentreter, Dr. Georg Isbary, Dr. Satoshi Shimizu, and Dr. Tim Maisch. I would like to thank Dong Li, Angelika Langer, Silvia Goldbrunner and other members of the MPE for their administrative work.

An dieser Stelle möchte ich mich herzlich bei meiner Familie, Onkel Manfred, meinem Bruder Seung und Tante Sook, für ihre Unterstützung bedanken.

CONTENTS

Chapter 1

Introduction

1.1 Definition of Plasma

Plasma is often referred to as the fourth state of matter. In the solid state, the atoms, molecules and ions are arranged at fixed locations and build up a lattice. As more heat is added to the system the interparticle bonds in the matter loosen and the system finds itself in liquid state. As the liquid matter is heated further, the system changes into gaseous state. The interparticle bonds become negligible compared to the kinetic energy of the system, and the particles can move freely. As the internal energy of a gaseous system is increased beyond their ionization energy, the neutral gas particles can be ionized and charge carriers, i.e. electrons and ions, can move freely. A particle system that contains freely movable charge carriers is called plasma.

The first use of the term plasma goes back to Irving Langmuir (1881 - 1957). He associated the positive column of a DC gas discharge, the quasi-neutral part of the discharge comprising electrons, ions and neutral gas particles, with the blood plasma that carries different kinds of species including red and white blood cells and germs [1].

Today, it is known that the most part of the visible matter in the universe is constituted by plasma, in particular hydrogen plasma. Intergalactic, interstellar and interplanetary plasmas, the solar wind, solar coronas and stars, such as the Sun, red giants and white dwarfs, are examples for the astrophysical plasmas. The ionosphere, the plasmasphere and the van Allen radiation belts of the Earth's atmosphere comprise plasma. Man-made plasmas are generated in fusion reactors, in laboratory and technical discharges and for plasma processings.

The elementary plasma parameters extend over many orders of magnitude: The particle density ranges from $\sim 1\ \mathrm{m}^{-3}$ for intergalactic plasmas to $\sim 10^{37}\ \mathrm{m}^{-3}$ for white dwarfs. The temperature ranges from $\sim 10^3$ K for laboratory and technical discharges

to $\sim 10^8$ K for fusion reactors and star core. High magnetic fields of up to 10^4 T have been observed from white dwarfs .

1.2 Categorization of Plasma

1.2.1 Ideal Plasma

If the mean thermal kinetic energy $E_{kin} = \frac{3}{2}k_B T$ exceeds the mean Coulomb potential energy $E_{pot} = \frac{e^2}{4\pi\epsilon_0} n^{-\frac{1}{3}}$, the system can be called an ideal plasma. The ratio of the potential energy to the kinetic energy, the coupling parameter Γ_c, is given by the following equation for electrons

$$\Gamma_c = \frac{e^2}{4\pi\epsilon_0 \bar{r}} \frac{1}{k_B T_e} = \frac{e^2}{4\pi\epsilon_0 k_B T_e} \sqrt[3]{\frac{4\pi n_e}{3}} \tag{1.1}$$

with the Wigner-Seitz radius $(4\pi n_e/3)^{-1/3}$ used as the mean interparticle distance $\bar{r}$. For the ions of the ionization state z, the charge, the temperature and the particle density need to be changed accordingly. Hence, an ideal plasma is given if $\Gamma_c \ll 1$.

1.2.2 Thermal and Non-Thermal Plasma

In a thermal plasma, all charged and neutral particles are in a thermal equilibrium, i.e. electrons, ions and neutrals have the same temperature ($T_e \approx T_i \approx T_n$). Most of the astrophysical plasmas are thermal plasmas. Man-made thermal plasmas are produced mainly in fusion reactors and in arc discharges. Because of the typically high energy and energy flux density, the arc discharge is widely used in diverse areas of engineering e.g. for welding, cutting, waste destruction, in arc furnaces, arc lamps,

as shutters in electric circuits and in surface modification by thermal plasma chemistry (via quenching) [2].

In a non-thermal plasma, alternatively nonequilibrium, low temperature or cold plasma, the electrons are at a much higher temperature than the ions ($T_e \gg T_i$), which have in general the same temperature as the neutral background gas particles ($T_i \approx T_n$). Since the mass of ions and neutral particles is much larger than of electrons, the particle system as a whole is at room temperature. This condition can be obtained, for example, by applying an external electric field with a high voltage (HV) at radio-frequency (RF) using opposed electrodes at a typical distance of $\sim$ mm. The ions cannot follow the high frequency of the external field due to their heavy mass and small mobility. Hence, the ions are hardly accelerated and the ion temperature remains at the level of the background gas, i.e. at room temperature. On the contrary, the electrons are able to follow the RF of the external electric field and gain energy according to the applied input power.

1.2.3 Low-Pressure and Atmospheric Pressure Plasma

Non-thermal plasma can be sub-categorized into atmospheric pressure and low pressure plasma applications. The advantages of the processing at low pressure include a high energy yield and precision due to the small number of collisions and a high purity of the processed plasma gas. Low-pressure non-thermal plasmas are used particularly for materials processing, e.g. in the plasma-enhanced chemical vapor deposition (PECVD). However, the need for a vacuum system induces several drawbacks such as higher expenses, longer operation times and larger space requirements that make the plasma setup unwieldy and immobile.

The generation and application of non-thermal plasma at atmospheric pressure allow the treatment of vacuum-sensitive materials, e.g. living tissues. The plasma generator can be modified according to the requirements in a versatile way. For example,

the plasma can be generated and applied in an open volume and portable devices can be designed.

1.3 Relevant Parameters of Plasma Physics

Debye Length

In a plasma, a single charge is screened by the neighboring opposite charges. As a consequence, the Coulomb force is attenuated, which is quantified by the Debye length

$$\lambda_D = \sqrt{\frac{\epsilon_0 k_B T_e}{n_e e^2}}$$

where T_e is the electron temperature and n_e the number density of electrons.

Plasma Parameter

The *plasma parameter*

$$N_D = \frac{4\pi}{3} n_e \lambda_D$$

gives the number of electrons in a sphere with the radius of Debye length.

Plasma Frequency

The characteristic oscillation of the charge carriers around their equilibrium positions is described by the plasma frequency

$$\omega_p^2 = \omega_{pe}^2 + \omega_{pi}^2$$

where ω_{pe} and ω_{pi} are the plasma frequency of electrons and ions, respectively, and defined as

$$\omega_{pe} = \sqrt{\frac{n_e e^2}{\epsilon_0 m_e}} \quad \text{and} \quad \omega_{pi} = \sqrt{\frac{n_i Z_i^2 e^2}{\epsilon_0 m_i}},$$

where ϵ_0 is the vacuum permittivity, n_i the number density of ions, m_e and m_i the mass of electrons and ions, respectively, and Z_i the charge number of ions. The plasma frequency ω_p can be approximated by the electron plasma frequency ω_{pe} because of the large mass ratio of ions to electrons. Electromagnetic waves with a frequency greater than the plasma frequency can traverse the plasma. At lower frequencies, the wave is reflected by the plasma.

Degree of Ionization

The degree of ionization is defined as the ratio of the number density of ions to the total number density of the system

$$\alpha_i = \frac{n_i}{n_i + n_n} \approx \frac{n_i}{n_n}$$

where n_i and n_n are the number densities of ions and neutrals, respectively. If the system is in the thermodynamic equilibrium, the density ratio of the ions with different degrees of ionization is given by the Saha equation:

$$\frac{n_{z+1} \cdot n_e}{n_i} = \frac{g_{z+1}}{g_z} \frac{2}{\lambda^3} \exp\left[-\frac{\chi_z}{k_B T}\right] \tag{1.2}$$

n_z and n_{z+1} are the ion densities and g_z and g_{z+1} the degeneracies for the states of ionization z and $z+1$, respectively. χ_z is the ionization energy for the ionization state z, k_B the Boltzmann's constant, T the temperature and

$$\lambda = \sqrt{\frac{h^2}{2\pi m_e k_B T}}$$

the thermal de Broglie wavelength of an electron, with h the Planck's constant and m_e the mass of an electron. In low-temperature laboratory plasmas, the typical degree of ionization is between 10^{-7} and 10^{-5}.

From the plasma setups used in this thesis, as will be described in the following chapters, the electron temperature was estimated $\sim$ 700 K and the electron density at 10^{14} - 10^{15} cm^{-3}, leading to the Debye length of $\sim 10^{-1}$, the plasma parameter $\sim 10^{7}$ - 10^{8} and the electron plasma frequency of $\sim$ MHz. With the number density of air $\sim$ 10^{-21} cm^{-3}, the degree of ionization in the plasma volume was estimated below 10^{-6}.

1.4 The Importance of Hygiene

1.4.1 Nosocomial Infections

Infections that occur within 48 hours after the admission to a medical facility is called nosocomial infections or alternatively hospital-acquired or health care-associated infections (HAIs). According to Klevens et al., the estimated number of the annual nosocomial infections in the U.S. in 2002 was approximately 1.7 million and was higher than the number of infections with any notifiable disease [3]. The estimated number of deaths associated with the nosocomial infections was approximately 99 000 and outweighed several top ten causes of death in U.S. In a recent study, Magill et al. reported that approximately 4% of the patients in acute care hospitals in U.S. had acquired one or more nosocomial infections in 2011 [4]. They estimated that there were nearly 650 000 patients with nosocomial infections nationwide.

According to a report by the European Centre for Disease Prevention and Control, the estimated number of the nosocomial infections in acute care hospitals in the European Union and Croatia was 3.2 million patients per year in 2011 - 2012 [5]. It

was assumed that approximately 6% of patients in acute care hospitals had acquired nosocomial infections. The Hospital in Europe Link for Infection Control through Surveillance (HELICS) estimates that approximately 5 million nosocomial infections occur in acute care hospitals in Europe annually, leading to 135 000 deaths per year [6]. Country-specific studies estimated 125 000 patients in Belgium [7], 46 000 patients in Finland [8] and 321 000 patients in Great Britain [9] with nosocomial infections. In Germany, 10 000 to 15 000 deaths were estimated from 400 000 to 600 000 nosocomial infections in 2006 [10].

The most common pathogens from nosocomial infections are coagulase-negative *staphylococci*, *Staphylococcus aureus*, *Enterococcus* species, *Candida* species, *Escherichia coli* species, *Klebsiella* species and *Pseudomonas aeruginosa*. Additionally, multidrug-resistant pathogens as methicillin-resistant *S. aureus* (MRSA), vancomycin-resistant *Enterococcus* (VRE) and carbapetem-resistant *P aeruginosa* are among the most frequently isolated pathogens from nosocomial infections [5, 11].

A particularly high risk of infection was found during surgeries and invasive treatments e.g. via catheter, mechanical ventilation and intubation [3, 5]. The major sites of nosocomial infections are Pneumonia, at the urinary tract, at surgical sites and in the bloodstream. Patients in acute care hospitals or in intensive care units (ICUs) generally have a weakened immune system which often increases the incidence and mortality for the nosocomial infection [12]. The large numbers of nosocomial infections give rise to tremendous costs for the health care system. Especially, the infection with antibiotic-resistant bacteria extends the hospitalization, increases the risk of death and requires costly treatments with toxic antibiotics. The estimated overall medical costs of nosocomial infections range from 30 to 45 billion dollars per year in U.S. [13]. The HELICS estimates that the annual economic burden of nosocomial infections in Europe is €13 - 24 billion [6]. Reed and Kemmerly calculated an additional medical cost of $ 650 - 134 602 due to the infection with antibiotic-resistant bacteria depending on the site of infection [14].

1.4.2 Surgical Hand Antisepsis

Considering the large numbers of infections, costs and deaths, the prevention of nosocomial infections is of great importance. The proper hand disinfection of the medical staff is as essential as the effective sterilization of invasive and non-invasive tools used in medical facilities.

Widmer observed that 35% of sterile gloves have tiny punctures after 2 hours of surgery [15]. Doebbeling et al. found that even unused gloves do not fully prevent bacterial contamination of hands [16]. Furthermore, there have been reports about infections by contaminated hands of the surgical team despite wearing sterile gloves [17–19]. The European Prevalence of Infection in Intensive Care estimated that 40% of nosocomial infections come from poor hand hygiene [20]. There are many different handrub formulations for the surgical hand preparation. The World Health Organization's (WHO) Guidelines and Hand Hygiene in Health Care recommends formulations comprising alcohol (ethanol/isopropyl alcohol), hydrogen peroxide and gylcerol [21]. Depending on the formulation, hand rubbing from 30 seconds to 5 minutes are required. However, skin irritation, dermatitis, dryness and allergic reaction are frequent side-effects from using alcohol-based handrubs [22, 23]. As pointed out by Morfill et al., the medical staff is confronted with 60 - 100 hand disinfections a day, which would lead to a daily disinfection time of 3 to 8 hours in total [24].

1.5 Conventional Sterilization Techniques

Effective sterilization is important for invasive as well as non-invasive tools, as the contamination can be transmitted in diverse ways [21]. For the sterilization of invasive tools in medical facilities, there are several commonly used techniques.

1.5.1 Heat

Heat is the oldest and best recognized sterilizing agent. It is assumed that heat induces a denaturation and/or coagulation of macromolecules, especially proteins and enzymes, and causes oxidative damage especially by free radicals. Moreover, it is possible that a heat shock induces the apoptosis of cells. The application of dry heat can impair the electrolyte balance due to the absence of water and thereby cause toxic effect.

Boiling water or saturated steam is used for moist heat sterilization. Basically, water is not a good sterilizing agent because of its relatively low boiling temperature. But its availability and the economical and environmental advantages favor using water. Moist heat sterilization is quicker than dry heat sterilization because of the greater heat conductivity of water/steam and the additional heat transfer during condensation. The most common method is performed inside a pressure vessel (e.g. autoclave) using saturated steam at 121°C or 132°C. The typical sterilization duration varies between several minutes and 60 minutes depending on the temperature, mechanism and object species. The main drawbacks of using hot steam are the corrosion of the metal and sharp instruments and erosion e.g. of glass surfaces. Another major drawback is the strong increase of water's vapor pressure at high temperature. According to the data from the Dortmund Data Bank [25], a temperature increase from 140°C to 160°C entails a pressure increase from 3.6 to 6.1 bar. A further temperature increase by 20°C to 180°C results in a pressure of 9.6 bar.

The high pressure requirements make the moist heat sterilization technique dangerous and impracticable at temperatures above 132°C. If higher temperatures are required, dry heat sterilization with air as medium is used instead. Moreover, dry heat is capable of penetrating materials that are impenetrable for steam and water vapor. It is a prevalent belief that the primary mechanism of the sterilization by dry heat, including incineration, is an oxidation process. Since air has a much lower heat conductivity

than steam, the sterilization by dry heat takes much more time than by moist heat. The suggested sterilization time depends on the temperature and varies from 60 minutes at 170°C to "overnight" at 121°C [26]. Oag found an abrupt increase of the sporicidal efficacy by dry heat at 160°C, significantly reducing the required sterilization time above this temperature [27]. Generally, the dry heat sterilization is recommended only if steam is not applicable due to the expected surface damage as mentioned above or due to impermeability (e.g. for petrolatum, oils and powders) [26].

The general drawbacks of the heat sterilization are the inapplicability to heat sensitive materials and the deleterious effects to the treated material surfaces (corrosion, erosion and oxidation).

1.5.2 Gaseous Biocidal Chemicals

The sterilization using gaseous chemicals can be performed at relatively low temperatures of $\sim$ 35°C to 80°C [28]. The sterilizing agents can be subdivided into alkylating and oxidizing chemicals. Commonly used alkylating chemical agents are ethylene oxide (C_2H_4O), propylene oxide (C_3H_6O), formaldehyde (CH_2O) and beta-propiolactone ($H_4C_3O_2$). Commonly used oxidizing agents are hydrogen peroxide (H_2O_2), peracetic acid (CH_3CO_3H) and chlorine dioxide (ClO_2) and ozone (O_3). For the sterilization of medical devices, the alkylating sterilants ethylene oxide and formaldehyde are most extensively used, while propylene oxide is frequently used especially in the food industry. Due to the oxidative properties, the application of the oxidizing gaseous sterilization is limited to corrosion-resistant materials only. The gaseous sterilization is strongly affected by both the ambient air, which hampers the permeability of the gaseous sterilants, and the humidity. The predominant sterilizing chemical gas is ethylene oxide (EtO). Compared to other gaseous chemical sterilants, EtO sterilizes fast, especially regarding the availability of the sterilized material, shows a good permeability (e.g. through packaging materials, occluded locations) and is associated

with a relatively low potential of misapplication. The typically required sterilization time varies between 30 minutes and 9 hours depending on the surface temperature and procedure.

The main drawback of using gaseous chemicals for sterilization is the risks for the human health. EtO has been classified as a mutagen and human carcinogen by the International Agency for Research on Cancer (IARC). The Occupational Safety and Health Administration (OSHA) limits the exposure to EtO by 1 ppm in 8-hour time weighted average (TWA). Several other chemical gaseous sterilants such as formaldehyde, chlorine dioxide, hydrogen peroxide and propylene oxide are subject to limitations as well, with the OSHA limits ranging from 0.1 ppm to 20 ppm in 8-hour TWA. Sterilization by EtO produce toxic chemical residues and byproducts such as ethylene glycol and ethylene chlorohydrine. Additionally, EtO has a flammability range of 3% to 100% by volume in air and it is possible that EtO deflagrates in absence of oxygen.

1.5.3 Ultraviolet (UV) Radiation

Downes and Blount (1877) were among the first who reported about the destruction of bacteria and fungi by the sunlight [29]. The antimicrobial property of UV has been primarily utilized for the water purification. Especially, the use of UV has been gaining growing popularity since the disclosure about the noxious byproducts from ozonation and chlorination [30]. The sterilization by UV is initiated by the absorption of the photon by the pyrimidine bases of the nucleic acids (DNA and RNA). As illustrated by Blatchley and Peel, the absorption spectra of purine and pyrimidine bases as well as amino acids show a maximum at wavelengths between 250 nm and 280 nm in UVC and UVB range [31]. UVA light with wavelengths of 320 nm or more is poorly absorbed by the nucleobases. Vacuum UV with wavelengths below $\sim$ 200 nm have been found not to contribute to the antimicrobial effect since water vapor and nitrogen and oxygen molecules (N_2 and O_2), the main constituents of the ambient air, behave as

strong absorbers in this range. The absorbed energy induces photochemical reactions, from which a dimer is formed between two of the bases [32]. The dimer inhibits the formation of a new nucleic acid chain and thus the cell replication [33]. Depending on the biological indicator and the setup, the required UV dose for the inactivation of the microorganisms vary between a few and several tens of mJ/cm^2 [34,35].

The second mechanism of the UV sterilization is the release of free radicals that increase the oxidative stress [36], leading e.g. to the peroxidation of the lipid membrane. This oxidizing process can result in DNA damage [37–39].

The main drawback of sterilization by UV is the impermeability. UV cannot penetrate various packaging materials including glass and cannot reach occluded objects. Furthermore, UV sources are relatively expensive and must be operated with care. The National Institute for Occupational Safety and Health (NIOSH) recommends a maximal UVC dose of 0.2 $\mu W/cm^2$ [40]. As UV can destroy the nucleic acids, it can cause skin cancer and be harmful for human eyes.

1.6 Novel Sterilization Technologies

Novel technologies for sterilization have been developed and are being investigated. In the following, two promising alternatives to the conventionally used sterilization methods are breifly described.

1.6.1 Photocatalysis

Several semiconducting metal oxides absorb light in the near-UV range (> 360 nm) and produce a electron-hole pair. This reaction and the corresponding material are termed the photoactivation and a photocatalyst, respectively. The hole is located

at the surface of the photocatalyst and can react with hydroxyl ions or adsorbed water molecules to produce radicals such as OH•. The freely movable electron in the conduction band can reduce an oxygen molecule to form a superoxide anion O_2^-•. These extremely reactive species can react further to produce H_2O_2 and HO_2• [41,42]. The most photoactive and most frequently used photocatalyst is titan dioxide (TiO_2), followed by ZnO and WO_3 [43]. Usually, catalyst particles in the dimension of nanometers are used. A number of studies demonstrated the inactivation of different vegetative bacteria, some viruses, fungi, yeast and algae by photocatalysis within several tens of minutes [41, 42, 44–46]. The exact mechanism of the photocatalytic sterilization is still under discussion. There is growing evidence that the outer membrane of the microbial cells is damaged by photocatalytis [42]. The main advantages of the photocatalytic sterilization over the common methods include the non-toxicity and the inexpensive operation, as highlighted by Ollis [43].

1.6.2 Photodynamic Treatment

In the beginning of the 20th century, Raabe (1900), Jesionek and Tappeiner (1903) and Hausmann (1908) found that the combination of (fluorescent) dye and light can kill several pathogenous microorganisms [47–49]. Since then, the photodynamic therapy using a non-toxic dye, termed a photosensitizer (PS), and visible light has been developed. The focus lied initially on the cancer treatment. Further investigations have expanded the area of application to ophthalmology, dentistry, skin and blood vessel diseases and infectious diseases. The PS is delivered to the treated tissue and irradiated. The excited triplet state of the PS reacts with oxygen to produce cytotoxic species. Two pathway types have been found that produce either superoxide, hydroxyl and lipid-derived radicals (type I) or singlet oxygen (type II) [50, 51]. Chlorins, bacteriochlorins, phthalocyanines and texaphyrins are among the best investigated PS for the cancer treatment, with hematoporphyrin derivate (known as Photofrin) as the most

well-known example. PS with the focus on the antimicrobial properties include halogenated xanthenes (e.g. rose bengal), phenothiazines (e.g. toluidine blue O, methylene blue and its derivates), acridines and perylenequinones (e.g. hypericin) [52,53].

A variety of pathogens including MRSA, some viruses, yeast and parasites has been reported to be inactivated by the photodynamic treatment, as shown by Hamblin and Hasan in an overview [53]. Malik et al. observed a fundamental difference between Gram-positive and Gram-negative bacteria in the susceptibility to the photodynamic treatment [54]. As summarized by Maisch [52], the lipophilicity of the PS appears to play an important role. There are ongoing investigations especially on the optimizing of the PS in order to increase the inactivation efficacy of GR- bacteria by the photodynamic treatment.

Most of the clinical studies were performed using laser light sources with wavelengths of 400 nm - 750 nm. The typical radiation dose was 50 to 500 J/cm^2 depending on the depth, the light source and the PS [55]. The irradiance should not exceed 200 mW/cm^2 because of hyperthermia.

The main advantage of this technique is the high precision. Both the delivery of the PS to the tissue and the site of irradiation can be precisely located. But it is also its main drawback, since the treatment is locally limited.

1.7 Cold Atmospheric Pressure Plasma for Sterilization

The conventionally used sterilization techniques are afflicted with partly serious drawbacks. In this regard, the use of cold atmospheric pressure plasmas (CAPs) for disinfection and sterilization has been drawing increasing attention over the last two decades [56–60]. A comparison of the relevant parameters for sterilization using the

Table 1.1 Important parameters of the various sterilization methods.

	Temperature at the tissue	Treatment duration	Damage to the tissue	Ecological sound-ness	Safety for the user	Portability
Wet heat	120 - 130 °C	< 60 min	yes	no	largely	no
Dry heat	> 160 °C	> 60 min	yes	no	largely	no
UV	∼ r.t.*	< 20 min	possible	yes	yes	no
Chemicals	< 80 °C	30 - 500 min	yes	no	no	no
Photocatalysis	∼ r.t.*	∼ 60 min	partly	yes	yes	possible
Photodynamic	∼ r.t.*	∼ 20 min	no	arguable	yes	yes
CAP	∼ r.t.*	< 10 min	no	yes	yes	yes

∗ r.t.: room temperature

conventional methods and CAPs is shown in table 1.1, according to Laroussi and Hermann et al. [61, 62]. The sterilization by the CAPs does not require high temperatures and does not cause thermal stress to the tissue and the treated material. The reduction of the microbial burden by 10^5 to 10^7 log requires several seconds to a few tens of minutes of exposure, which is very fast in comparison with the conventional methods. The application of the CAPs is regarded safe for the user and the environment. The CAP sterilizing system can be configured in a versatile way. Since no vacuum is required it is possible to design portable CAP devices for sterilization, which widens the range of application dramatically.

While thermal plasmas, generated by arc discharges in the most cases, are already available on the commercial market for example for the use in the surgery (e.g. for cutting, ablating and coagulating) as reviewed by Lloyd et al. [63], the development of CAP devices for the medical and hygienic purposes are still in a premature stage. Sterilization using cold plasmas at low pressure generally works in combination with a reactive gas vapor such as hydrogen peroxide or paracetic acid [64]. The research on CAPs with regard to medical and hygienic application currently focuses on the surface sterilization and disinfection, cancer treatment, dermatological treatment and the dental care [56, 63, 65–69]. Different types of plasma generation and different mecha-

nisms for the transport of the reactive agents onto the tissue and material have been developed and discussed in the following sections.

1.7.1 Corona discharge

Corona discharge appears at a sharp edge or in the vicinity of a strong curvature of the electrode, where the potential gradient (i.e. electrical field) is greatly enhanced thus that the surrounding gas or liquid molecules are ionized and become partially conductive [70]. Usually, either the point-to-plate geometry with a pin electrode or the cylindrical geometry with a thin wire electrode are used [71]. Combined configurations such as the needle-to-cylinder geometry have also been developed [72]. Figure 1.1 shows the schematics of the different arrangements for the corona discharge. Depending on the power supply mode, there are three different types of corona discharge: AC, DC positive and DC negative. A number of studies have demonstrated the antimicrobial effect of the corona discharge. Korachi et al. and Joubert et al. successfully inactivated different vegetative bacteria, bacterial endospores, yeasts, fungi and algae suspended in water and recommended the use the corona discharge for the water purification [71, 73, 74]. Scholtz et al. successfully inactivated vegetative bacteria, yeast and bacterial endospores both spread on agar surface and in aqueous suspension [75]. Dobrynin et al. observed a higher biocidal effect if the current from the discharge passed through the treated sample [76], whereas Machala et al. could not see any enhancement of the bactericidal effect with the current passing through the tissue [77]. The latter observation suggests that reactive oxygen species were mainly responsible for the inactivation of the biological indicator. Yamamoto et al. reported that the bactericidal effect on *Escherichia coli* was greatly enhanced if H_2O_2 droplets were added to the corona discharge treatment [78].

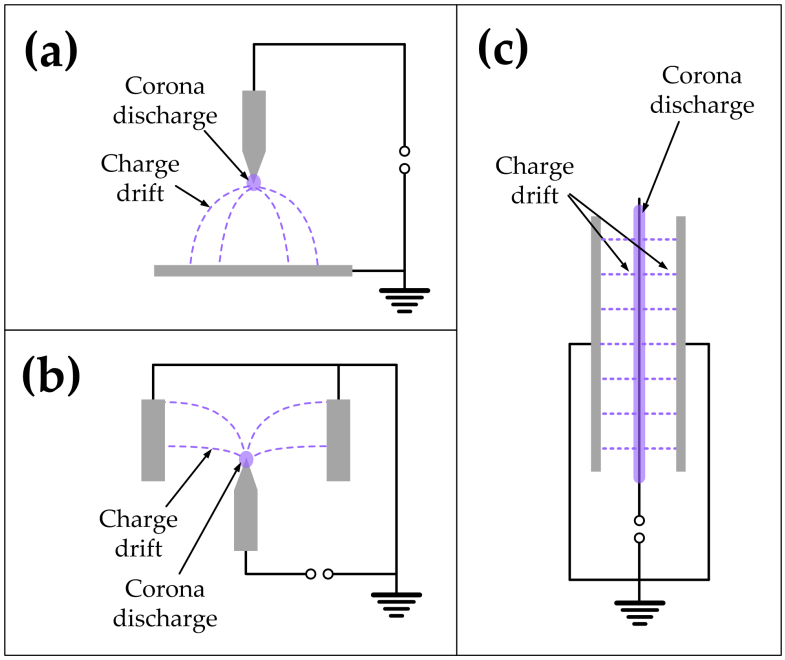

Figure 1.1 Schematic view of different arrangements for corona discharge. (a) point-to-plate, (b) needle-to-cylinder, (c) wire-to-cylinder.

1.7.2 Glow Discharge

The glow discharge was invented in the 1870s by Sir William Crookes (1832 - 1919) by applying a high voltage in a low pressure tube ($\sim 10^{-6}$ to 10^{-8} bar) [79]. Electrons and ions are accelerated towards the electrodes and the "glow" appears as the neutral gas molecules are excited by collisions. In 1933, von Engel et al. [80] successfully operated a dc glow discharge at atmospheric pressure. An effective cooling system for the cathode was required because of the heat generation from ion bombardments and from the ohmic loss in order to prevent the transition to an arc discharge. Roth et al. [81] showed that the cathode heating can be suppressed by applying radio-frequency (RF) instead of DC. Above a critical RF driving frequency, the ions are trapped in the RF electric field. As consequences, the sputtering and erosion at

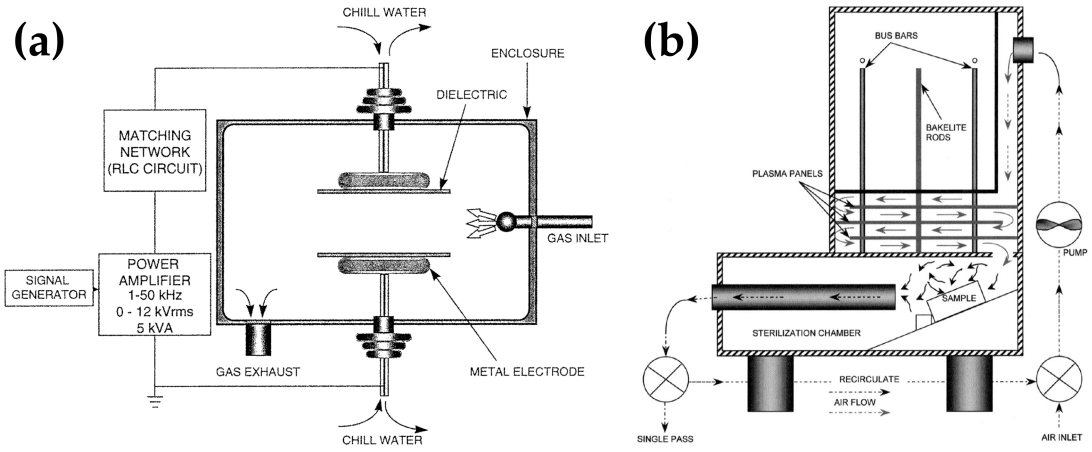

Figure 1.2 Schematic view of the setups for the exposure of the biological indicator to the OAUGDP. (a) direct exposure, (b) indirect exposure (*by Montie et al.* [83]).

the electrode surface as well as the contamination of the plasma were reduced and the ion density in the plasma bulk was increased. In addition, a dielectric was attached to at least one of the electrodes in order to prevent the glow-to-arc transition and protect the electrodes. This type of discharge was termed the One Atmosphere Uniform Glow Discharge Plasma (OAUGDP) [82]. The schematics of the experimental setup for both the direct and indirect treatment with OAUGDP are shown in Figure 1.2. Typical frequencies are 1 - 50 kHz with the root-mean-square (rms) voltage ranging 1 - 10 kV [61].

Montie et al. and Kelly-Wintenberg et al. showed the redution of various bacteria, yeasts and viruses using the OAUGDP [83, 84]. Vleugels et al. inactivated biofilm-forming bacteria by glow discharge at atmospheric pressure using He-O_2 gas without causing decoloration on the food surface [85].

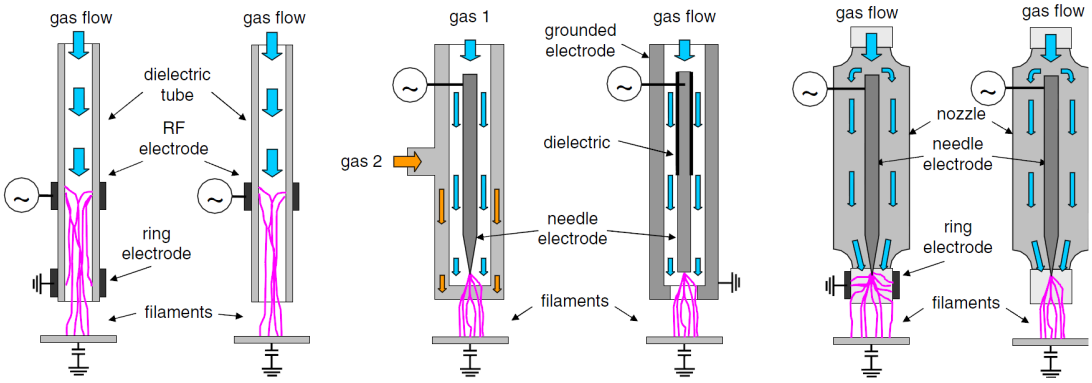

Figure 1.3 Principle designs for the APPJ (*by Ehlbeck et al.* [92]).

1.7.3 Atmospheric Pressure Plasma Jet (APPJ)

In 1998, the research team of Jeong, Babayan, Schütze and Selwyn et al. presented the atmospheric pressure plasma jet (APPJ) and its application possibilities such as etching, plasma-enhanced chemical vapor deposition and decontamination of chemical and biological warfare [62, 86–88]. The APPJs are usually composed of a cylindrical body made of a dielectric and two concentric electrodes. Either a noble gas, mostly helium or argon, or a noble gas with an admixture of oxygen or nitrogen is fed into the body. The feed gas is ionized by the discharge and blow the reactive species out of the nozzle in form of a luminous plume [89–91]. Figure 1.3 shows the schematics of the typical APPJ designs [92].

Typically, RF of 13.56 MHz at a voltage of a few hundred volts is applied, resulting in a power consumption of 50 - 100 W [59]. The effluent usually reaches temperatures of 100 - 150 °C, which can be decreased to the level of room temperature e.g. by modifying the input power signal, as shown by Weltmann et al. [93]. The bactericidal effect of the APPJ has been shown by many using a variety of Gram-positive and Gram-negative bacteria [92, 94–97]

There are several modified designs of the APPJ. One of them is the plasma nee-

dle, developed by Stoffels et al. [59, 98]. It is a miniaturized plasma jet with helium as feed gas at a low flow rate. The power consumption can be decreased down to 10 - 300 mW where the temperature is similar to the body temperature. The bactericidal effect of the plasma needle has been shown by Sladek and Stoffels [99]. The primary target is the application to *in-vivo* tissues such as caries, skin diseases and cardiovascular diseases.

The plasma pencil, as presented by Laroussi et al. [100], is another modified APPJ setup. Two circular ring electrodes are attached to centrally perforated dielectric discs inside a dielectric tube with 2.5 cm in diameter. Helium with an admixture of oxygen was fed through at a flow rate of 1 - 10 slm [90]. The discharge was ignited by microsecond pulses and the power consumption was 1 - 3 W. The successful inactivation of *Escherichia coli* by the plasma pencil was shown by Laroussi et al. [95].

1.7.4 Microwave-Driven Discharge

CAP can be generated and sustained by microwave (MW) as well. A magnetron is commonly used as the microwave source. In the most cases, the MW frequency of 2.45 GHz is applied according to the industrial, scientific and medical (ISM) band. Either a wave guide or a coaxial cable guides the MW to the resonator or to the discharge head, where the feed gas is ignited [101,102]. The choice of the feed gas is not restricted, i.e. both novel gases or ambient air can be used as the discharge medium. A detailed analysis of the physical properties and the chemistry of the MW-driven plasma is given by Stonies et al. [103] and Jasinski et al. [104]. Green et al. determined the electronic temperature profiles in the air microwave plasma torch and found a relatively flat distribution around 4500 - 6500 K within 10 mm radius from the effluent core [105]. However, Kruger et al. [106,107] and Kim and Hong [108] observed that the ion temperature is about an order of magnitude lower than the electron temperature. The temperature of the torch effluent ranges near room temperature up to several hundred Kalvin de-

pending on the input power [109]. The microbiocidal effect of the MW-driven CAP have been demonstrated by several studies using different setups [109–116]. Isbary et al. treated chronic wounds with a MW-driven plasma torch and observed a significant reduction of the bacterial load and enhanced wound healing processes [117,118]. Arndt et al. reported that the treatment with the MW-driven plasma torch altered the expression of key genes that are crucial for the wound healing processes and improved cell migration [119].

1.7.5 Dielectric Barrier-Discharge (DBD)

In 1857, Siemens [120] invented an ozone generator by applying an alternate current at a sufficiently high voltage at the surface of two coaxial glass tubes. Here the glass walls acted as the dielectric barriers the electric current needed to overcome. A high voltage-driven discharge either with at least one electrode covered by dielectric or with the dielectric between two electrodes is termed a dielectric barrier discharge (DBD) [121]. The historical term "silent discharge", as established by Andrews [122] because of the absence of the sparks, which are accompanied by local overheating, generation of local shock waves and noise, also is still in use. Figure 1.4 shows the schematic views of the frequently used DBD configurations [121,123].

The arrangement resembles the glow discharge setup with a dielectric. In fact, the differentiation between the glow discharge and the DBD is rather artificial, since the same setup can operate both discharge modes depending on the discharge conditions, especially the gas composition [124–126]. Bogaerts et al. [127] pointed out that the atmospheric pressure glow discharge can be regarded as a diffuse DBD. Roth et al. [81] observed that the glow discharge formed "coarse filaments" as the applied frequency or the oxygen admixture ratio was increased.

DBDs usually operate at frequencies between the line frequency (50 - 60 Hz) and 1 MHz. There are many industrial applications using DBD because of its wide oper-

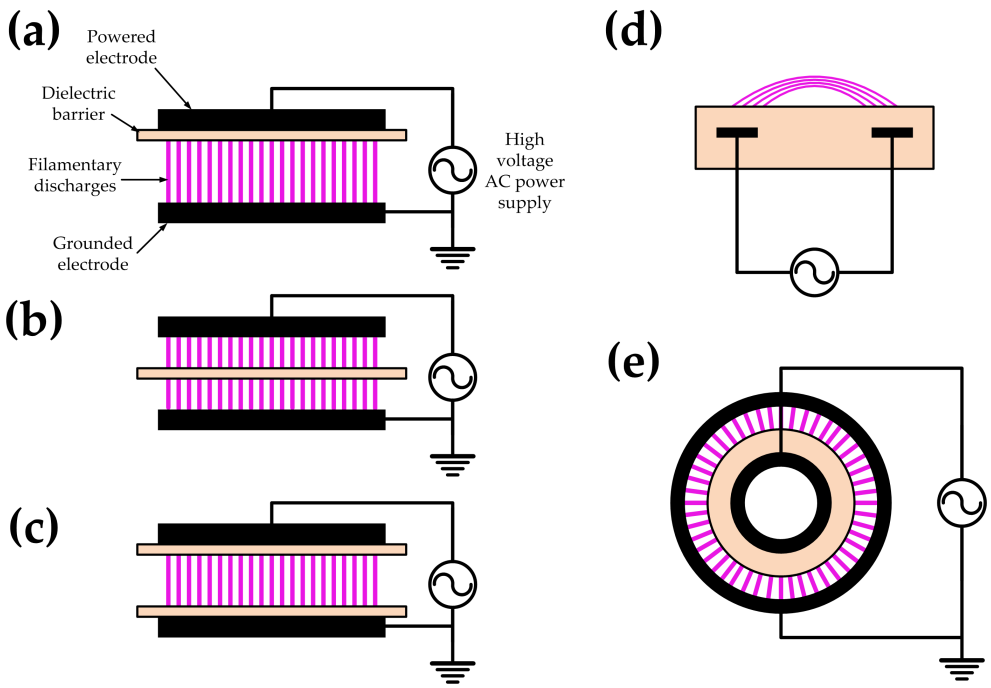

Figure 1.4 Typical configurations of dielectrical barrier discharge. Planar setups with the dielectric (a) covering one electrode, (b) between the electrodes and (c) covering both electrodes. (d) electrodes embedded in the dielectric (surface discharge) and (e) cylindrical setup (*according to Kogelschatz et al.* [121]).

ation range [92, 128]. The gap distance ranges between 0.1 mm to several centimeters depending on the application and the working gas. Glass, quartz, ceramics and polymers are commonly used dielectric barrier materials. The high voltage ($\sim$ 10 kV) AC produces charge accumulations at the dielectric surface. If the breakdown electric field strength is reached, a large number of filamentary micro-discharges emerge. The formation and collapse mechanism and the properties of micro-discharges are described in details in 1.8.

The microbiocidal effect of the DBD has been demonstrated by a number of studies using different arrangements and parameters. Trompeter et al. [129] and Choi et al. [130] demonstrated the inactivation of *Escherichia coli* bacteria and *Aspergillus niger*

and *Bacillus subtilis* spores using the classical setups as shown in Figure 1.4(a) and (c). Vandamme et al. [131] exposed a U87-luc glioma tumor *in-vivo* on the skin of mice to the DBD plasma and reported a significant decrease of both the tumor cells activity and the volume of the tumor. Eto et al. [132] showed that the sterilizing effect of the DBD can penetrate the packaging material. The number of *Geobacillus stearothermophilus* spores in a Tyvek® was reduced by 4 - 6 orders of magnitude (log) after tens of seconds of DBD plasma exposure. Fridman et al. have developed a DBD plasma source, termed the floating-electrode dielectric barrier discharge (FE-DBD), that applies the treated tissue as the grounded electrode [133,134]. They showed that FE-DBD can kill bacteria including *E. coli, Deinococcus radiodurans and MRSA* [135–138] and the skin flora (*Staphylococcus, Streptococcus*, kill yeasts, coagulate blood [133] and induce apoptosis in melanoma skin cells [134]. A number of modified DBD setups have been designed and tested for the microbiocidal effect with respect to the industrial and domestic use: Gallagher et al. showed fast inactivation of airborne bacteria using the dielectric barrier grating discharge (DBGD), a series of thin wires arranged in a plane and coated by a quartz capillary [139]. Leipold et al. developed a DBD-based sterilizer for rotating cutting devices and showed 5 log reduction of *Listeria innocua* within 6 minutes [140]. Schwabedissen et al. presented the "PlasmaLabel", a patented DBD setup with a variable electrode shape, and its sterilization efficacy of 4 log in 10 minutes on *Bacillus subtilis* [141]. Eto et al. used a linear DBD with the powered electrode, a tungsten wire, inside a quartz tube which was wrapped by the grounded aluminum wire [142]. A sterilization efficacy of 6 log in 10 minutes of plasma exposure inside the tube was observed using *G. stearothermophilus*. An embedded-type DBD similar to Figure 1.4(d) was presented by Li et al. [143]. Up to 4 log reduction of *E. coli* bacteria was achieved after several seconds of discharge. Heise et al. presented the cascaded dielectric barrier discharge (CDBD), comprising a DBD and an excimer lamp [144]. They demonstrated a 4 log reduction of *A. niger* and *B. subtilis* spores within several seconds [145].

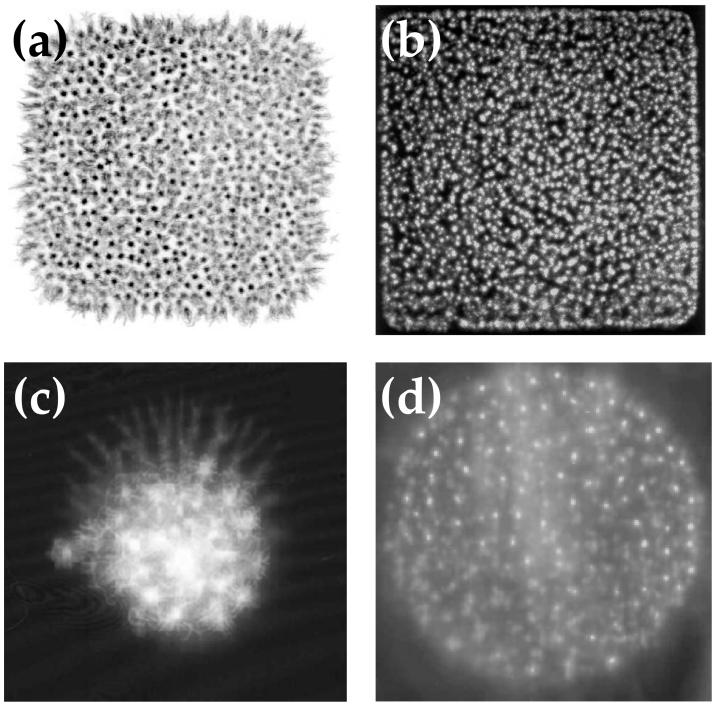

Figure 1.5 Lichtenberg-figures of the micro-discharges from different DBD-setups. (a) storage phosphor image [146], (b) photograph through a transparent electrode [147], (c) emulsion of the photofilms using a ms-pulsed DBD [148] and (d) via light-sensitive photographic film [149].

The dielectric between the electrodes limits the electric current of a single micro-discharge, distributes them homogeneously over the surface and thereby prevents the transition to a spark or an arc. The micro-discharges appear randomly in space and time, as depicted by means of Lichtenberg-figures (Figure 1.5). The mechanism for the formation of the micro-discharges is described in detail later.

1.7.6 Surface Micro-Discharge (SMD)

The surface micro-discharge (SMD) is a DBD-based arrangement designed by Gregor Morfill et al. [150]. A planar electrode and a mesh grid electrode are attached

to each sides of the dielectric. Usually, the planar electrode is connected to the high voltage power supply and the mesh electrode is grounded. By applying high voltage of $\sim$ 1 - 10 kV at $\sim$ 100 Hz - 20 kHz, numerous micro-discharges emerge between the mesh electrode and the dielectric. The spatial and temporal distribution of the micro-discharges are arbitrary. Due to the lack of a gap, the length of the micro-discharges can be controlled to some extent by the applied voltage. Detailed descriptions about the mechanisms and the properties of the SMD (or surface discharge, SD) are given by Gibalov and Pietsch [123, 151]. The properties and shape can vary e.g. depending on the input signal, as shown in Figure 1.6.

The bactericidal properties of SMD has been demonstrated by Shimizu et al. [150]. Gram-positive *Enterococcus mundtii* DSM3269 and Gram-negative *E.coli* DSM1116 bacterial strains were exposed to the SMD plasma at different relative humidities between 20 and 80%. About 5 log reduction was observed for both strains and no significant dependence of the bactericidal efficacy on the humidity was found. Maisch et al. demonstrated the microbiocidal effect of SMD on a variety of microorganisms including MRSA, *S. aureus*, *E. coli*, UV-resistant *D. radiodurans* and *Candida albicans* biofilms. [152–154]. While there was no large difference in the inactivation kinetics of different strains, the microbiocidal efficacy was strongly affected by the surface property. The required treatment duration for a 3 to 5 log reduction was ten times longer on the porcine skin than in a thin liquid film. Klämpfl et al. [155] observed 4 to 6 log reduction of diverse Gram-negative and Gram-positive bacteria, including the multidrug-resistant MRSA and VRE, spores and fungus after thirty seconds of SMD treatment. Bacterial endospores *Bacillus subtilis*, *Bacillus pumilus*, *Bacillus atrophaeus* and *G stearothermophilus* were inactivated inside the wrapping material Tyvek. The virucidal property of SMD has been shown by Zimmermann et al. [156]. A 6 log reduction of adenovirus was achieved within 240 seconds of treatment. The possible application of SMD for the cancer treatment has been discussed in several studies. Köritzer et al. [157] reported the enhanced sensitivity of the temozolomide (TMZ)-resistant glioma cells to

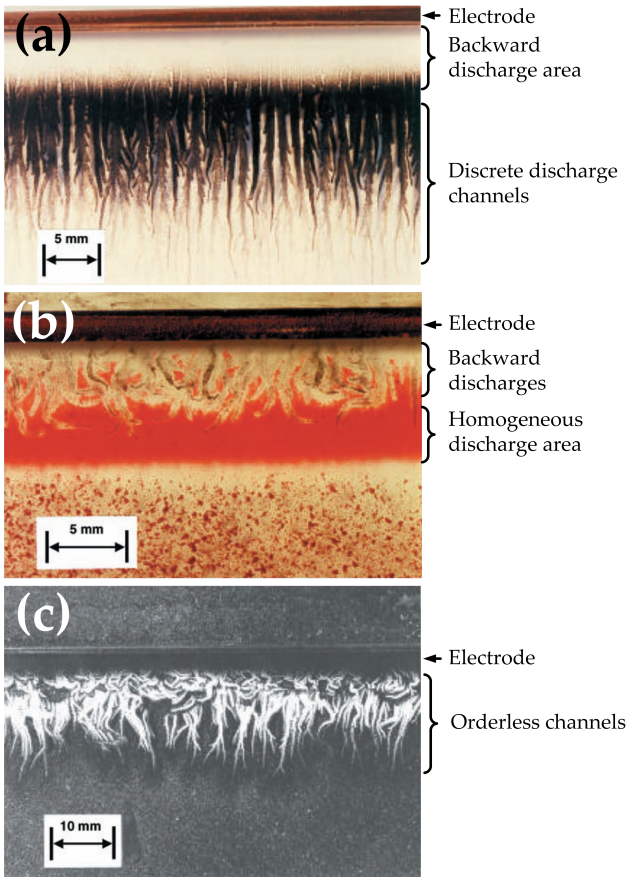

Figure 1.6 Discharge patterns of different surface discharge modes (dust figures). (a) 20 kV positive voltage pulse at the electrode, (b) 20 kV negative voltage pulse at the electrode and (c) 10 kV AC voltage (*by Gibalov and Pietsch* [151]).

the chemotherapy after the SMD treatment. Arndt et al. [158] showed that the SMD treatment induced senescence in melanoma cells including DNA damage, induction of the Sub-G1 phase and increased apoptosis and pre-apoptotic events. The scope of the SMD in industrial applications has been shown as well. Mitra et al. [159] reported 1 to 2 log reduction of the natural microbiota attached to the *Cicer arietinum* seed accompanied by the enhancement of the seed germination speed and quality. Zimmermann et al. successfully inactivated *E. coli* through different textiles [160]. The inactivation efficacy was reduced only by a factor of 2 in comparison with the treatment without

obstacle.

For the development of *in-vivo* applications, it is crucial that healthy cells are not harmed by the SMD treatment. Isbary et al. [161] evaluated the *ex-vivo* treatments of human skin with different SMD devices and observed no damage to the epidermal and dermal layers and no significant increase of DNA damage after 60 seconds of SMD treatment. Boxhammer et al. [162] reported that no mutagenic response was observed on V79 Chinese hamster cells after 240 seconds of *ex-vivo* SMD treatment. Welz et al. [163] treated nasal mucosa cells with SMD and observed no mutagenic effects after up to 120 seconds of exposure.

The bacterial inactivation by SMD has been intensively discussed. Boxhammer et al. [164] observed that the reduction of *E. coli* bacteria by the SMD treatment was greatly decreased if the initial density of the bacteria exceeded a certain threshold. They explained this observation by the shadowing effect, i.e. the overlapping of the microorganisms, and discussed this effect in detail. Shimizu et al. [165] changed the input power for the SMD by several orders of magnitude ($\sim 1 \cdot 10^{-4}$ - 3 W/cm^2) and investigated the correlation between the power, the bacterial reduction and the concentration and the production rate of ozone. They found a very strong correlation of the bacterial reduction with the ozone concentration and concluded that ozone could be one major player in the inactivation of *E. coli* by the SMD plasma. These results are described in detail in a later section.

1.8 Breakdown Mechanism of a Micro-Discharge

The formation of a micro-discharge breakdown is preceded by the Townsend discharge, as illustrated in Figure 1.7(a) [166, 167]. The initial electrons from the spontaneous ionization in the discharge gap move towards the anode with the electron drift

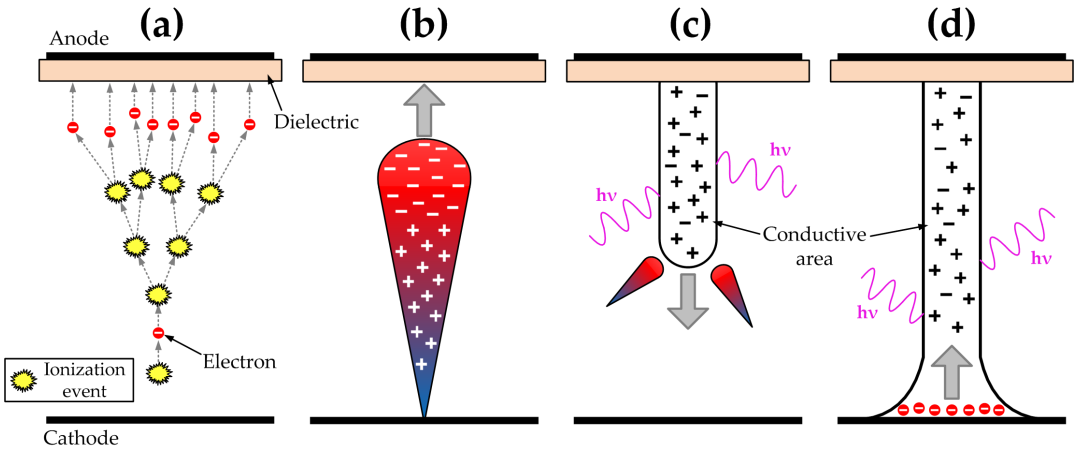

Figure 1.7 Different stages of the micro-discharge formation using a DBD (dielectric on the anode side). (a) Townsend discharge, (b) avalanche of charged particles approaching the anode, (c) propagation of the cathode-directed positive streamer, and (d) filamentary micro-discharge (*according to* [169, 172]).

velocity and collide with neutral molecules. Each electron drifting in the electric field is capable of ionizing neutral gas molecules they collide with according to Townsend's first ionization coefficient [168]. The number of the electron-ion pairs grow exponentially and an avalanche of charged particles is formed that moves towards the anode (Figure 1.7(b)). The initial avalanche does not affect the electric field between the electrodes and the produced current is negligible [169–171].

Due to the difference in the mobility, the ions in the tail of the initial avalanche either stay in place or drift slowly towards the cathode, while the avalanche electrons are quickly adsorbed at the anode (or anode dielectric) [170, 173, 174]. Secondary electrons are produced by the radiation from the excited particles, by the ion bombardment on the cathode or, depending on the gas composition, from the Penning effect [169, 174]. When the avalanche of the secondary electrons reach the anode, the high density of the positive ions near the anode leads to a strong field distortion which can grow up to a multiple of the external (displacement) electric field [169, 170, 175, 176]. The

drifting electrons from further detachment and ionization processes are affected by the field distortion and the charge accumulation grows in a self-amplifying process. As a consequence, the conductivity in this area is strongly enhanced and the area expands from near anode towards the cathode, forming the cathode-directed streamer (Figure 1.7(c)) [169,177,178]. During the streamer formation and propagation the electric field strength between the peak of the field distortion and the anode is significantly reduced, while the field towards the cathode increases further.

When the streamer reaches the cathode, the diameter of the channel broadens due to the interaction between the radiation from the streamer head and the cathode surface [171]. The strong field between the cathode and the streamer remains near the cathode surface, which is analog to the cathode layer of a glow discharge. The weak field along the most part of the filament between the cathode layer and the anode is similar to the positive column in a glow discharge [151,179]. The high density of the positive ions at the cathode gives rise to the radial expansion of the cathode layer due to the diffusive transport of the ions and the electron emission current increases (Figure 1.7) [171]. At the peak point of the current, the relevant parameters including the diameter of the filament, the dimensions of the cathode layer, the current, the charge densities and the electric field strength stay approximately constant and the discharge can be regarded as a quasi-stationary glow discharge [170]. Due to the depletion (if the dielectric is attached to the cathode) or the accumulation (if the dielectric is attached to the anode) of electrons at the dielectric surface, the mean electric field strength in the filament is reduced and the radial expansion decelerates until it stops. Consequently, the electric current decreases and finally the conductive filament fades.

The characteristic properties of the micro-discharge are given owing to the extensive studies, especially by Kogelschatz [147,180] and Gibalov et al. [123,151]. The typical parameters are listed in the Table 1.2 [128,180].

Within the filamentary micro-discharges, the temperature can reach up to several hundred degrees. Due to the short lifetime of the micro-discharges, the surround-

Table 1.2 Characteristic parameters of the micro-discharge (*according to* [128, 180]).

Lifetime	1 - 20 ns
Filament radius	50 - 200 µm
Peak current	$\sim$ 100 mA
Current density	$\sim$ 0.1 - 1 kV cm^{-2}
Charge transfer	$\sim$ 0.1 - 1 nC
Electron density	10^{14} - 10^{15} cm^{-3}
Electron energy	1 - 10 eV
Dissipated energy	$\sim$ 5 µJ

ing gas is not heated up significantly and remains at the room temperature [147].

1.9 Possible Mechanisms of the Microbiocidal Effect of CAPs

The possible sterilizing agents produced by the CAP are cytotoxic chemicals including reactive oxygen species and reactive nitrogen species (RNS) including radicals, UV radiation, charged particles, electric fields, chemical and physical etching as well as sputtering. The contribution of each of them to the antimicrobial effect depends on the plasma source, diverse treatment parameters, and the biological indicator. Heat can be excluded.

1.9.1 Heat

As mentioned before, the term "cold" declares that the temperature increase by the application of plasma is either nonexistent or negligible for the microbiocidal effect. The direct contribution of heat from CAPs to the inactivation of microorganisms,

especially thermophile bacterial endospores, was ruled out. However, temperature gradients between the plasma generator and the treated tissue give rise to thermal convection that can boost the transport of reactive species, as demonstrated by Shimizu et al. [181].

1.9.2 UV

UV photons are emitted during the relaxation processes of excited particles. At low pressures, UV appears to play an important role for plasma inactivation of microorganisms, as summarized by Moisan et al. [182, 183] As described above, there are two main mechanisms of UV inactivation of microorganisms: (*i*) The direct absorption of UV photon and formation of dimers in the nucleic acids and (*ii*) release of free radicals and oxidative damage. Generally, it was found that the contribution of UV to the microbiocidal effect of CAPs is negligible due to the insufficient radiation power [62, 78, 184–186]. However, Boudam et al. presented a narrow range of parameters for the operation of DBD at atmospheric pressure where *B. subtilis* spores were inactivated mainly by UV [187]. Heise et al. investigated the correlation of the sporicidal efficacy of the CDBD using different gases with the emission spectra and concluded that UV was the main inactivation agent for the *B. subtilis* and *A. niger* spores [145].

1.9.3 Reactive Species

At the atmospheric pressure, the energy from the plasma is dissipated mostly by collisions. A variety of reactive species arises from the inelastic collisions. If air is the background gas, the most important reactive species are atomic oxygen (O), singlet oxygen ($^1O_2$), ozone (O^3), hydrogen peroxide (H_2O_2), hydroxyl radical ($OH\bullet$), superoxide anion (O_2^-), nitric oxides (N_xO_y), nitric acids (HNO_x). Depending on the

transport mechanism (i.e. by diffusion or by a gas flow), the reactive species have to be subdivided into short-lifetime and long-lifetime species [188]. A detailed list of reactions has been compiled by Sakiyama et al. [189] and by Dorai and Kushner [190]. The peroxidation of the lipid membrane, the oxidation of proteins and oxidative damage to DNA are supposed to be the main mechanism of the microbial inactivation by reactive species [83,137,185]. A detailed review on the CAP-generated reactive species and their role in medicine and biology is given by Graves [191].

1.9.4 Charged Particles and Electric Field

In 1967, Sale and Hamilton [192] first presented the concept of the pulsed electric field (PEF) for the inactivation of bacteria and yeast with special respect to the food industry. Many studies demonstrated the lethal effect of PEFs on pathogeneous microorganisms since then [193–195] and the rupture of the outer membrane has been identified as the main mechanism [196,197].

Many authors have introduced the sub-category of the plasma "direct" treatment which is associated with the electric current passing through the treated tissue. The FE-DBD is one of the most intensively investigated plasma source for direct treatments. Fridman et al. [135] and Dobrynin et al. [198] observed enhanced bactericidal effect by direct plasma treatment. Mendis et al. [199] and Laroussi et al. [200] suggested that, in presence of a irregular curvature at the bacteria shell, the electrostatic tension could lead to a rupture and induce necrosis. Another possibility has been suggested by Stoffels et al. [201]. They point out that the typical charge a cell naturally develops in an aqueous solution is higher than the charge a cell would gain from the direct exposure to CAP. This also leads to rupture of the cell membrane and eventually to cell death, but the mechanism would be no charging but decharging of the cells.

In a further discussion, Stoffels et al. [201] the microbiocidal effects of electric currents through the liquid, if the microorganisms are suspended in it. In the case

that the liquid medium is isolated, the charge accumulates on the surface and attracts the ions from underneath, so that a thin ($\sim$ 1 mm) double layer of charged particles is formed. A current of less than 1 mA is sufficient to induce bactericidal effect [202]. However, the microorganisms have to be on the surface or within the thin layer, for the current decreases rapidly with depth in the medium [203]. Generally, the measurement of the electric field strength and the charge density from CAP is difficult. Further investigations on the microbiocidal effect by the electric fields from CAP depend on the development of the plasma diagnostics technology [57].

1.10 The Scope of the Thesis

The main focus of this work lies on (*i*) the identification of the reactive species responsible for the microbiocidal effect of SMD and (*ii*) the estimation of the contribution of the different reactive species to the microbiocidal efficacy.

As described in the previous sections, the microbiocidal property of SMD has already been demonstrated by many researchers on various biological indicators. It is generally assumed that the microbiocidal efficacy is due to the combination of various sterilizing agents. An attempt to identify the responsible species for the inactivation of *E. coli* by SMD was made by Shimizu et al. [165]. The strong correlation between the ozone concentration and the bacterial reduction, as illustrated in Figure 1.8, showed that ozone may be the major bactericidal agent.

In the following, two different surface micro-discharge setups are used to inactivate vegetative bacteria and bacterial endospores. The temperature increase and the UV radiation power from the SMD were found far below the lethal level for the microorganisms. The contribution of the short-lifetime reactive species (e.g. radicals, electrons, ions) was regarded negligible due to the gap of several millimeters between

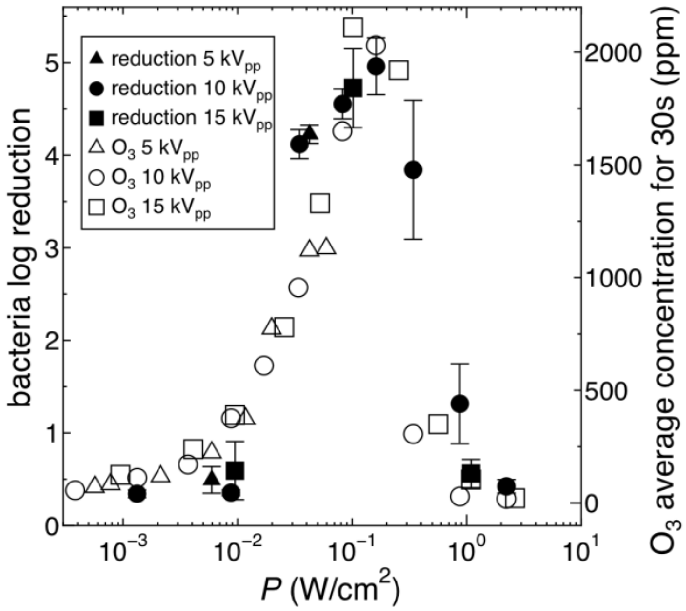

Figure 1.8 Bacterial reduction and average ozone concentration (*by Shimizu et al.* [165]).

the plasma discharge and the microbial sample. Details on the temperature increase, the UV radiation power and the short-lifetime species will be discussed later. Long-lifetime reactive species were suggested mainly responsible for the microbiocidal effect of the SMD. The concentration of ozone was monitored and analyzed as one indicator of the long-lifetime reactive oxygen species.

Bactericidal effect by controlling gas composition

In chapter 2, the gas composition for the discharge and bacterial treatment was varied using variety of argon, nitrogen and oxygen. The mixture ratio was changed and the bacterial reduction by the SMD was investigated. Gram-positive *Enterococcus mundtii* and Gram-negative *E. coli* bacteria were used as biological indicators. The bacteria were inoculated on an agar dish and treated for up to 120 seconds. The correlation of the concentration and the production rate of ozone with the bactericidal efficacy was investigated.

Sporicidal effect at different humidities and in a wide power range

In chapter 3, the input power for the discharge was varied in a wide range over 2 orders of magnitude. The heat-resistant bacterial endospores of *G. stearothermophilus* were exposed to the SMD for 5 minutes in a closed volume. The humidity was changed in three steps in order to estimate the contribution of the water-based chemistry to the sporicidal effect. The correlation of the concentration and the production rate of ozone with the sporicidal efficacy was investigated.

Transitions between the different ozone modes

Ozone was found as one possible major player for the inactivation of microorganisms by the SMD plasma treatment. So far, the concentration of ozone was manipulated by controlling the input power only. In chapter 4, the influence of the SMD electrode's geometry and the time span of the plasma generation on the production and quenching of ozone was investigated. The transition between the different ozone generation modes was highlighted.

Chapter 2

Bactericidal Properties with Controlled Gas Composition

2.1 Experimental Setup

2.1.1 Chamber and Gas Feed

In order to control the gas composition, a vacuum-sealable stainless steel chamber with an inner volume of approx. 7.2 liters was used. The SMD electrode was placed centrally on the bottom plate of the chamber. The opening on the top side was used for a gas feed and for the vertically movable rod, which was necessary for the gas exchange in the volume between the sample and the SMD electrode. Inside the chamber, an agar plate holder was attached horizontally to one end of the rod, as shown in Figure 2.1 (a). Two viewports made of quartz were attached to each of two opposing side openings for the ozone measurement via optical absorption spectroscopy. In total, four side openings were used for the electric feedthroughs and as exhausts (see Figure 2.1(b)). The chamber was grounded.

The gas composition in the chamber was exchanged by the gas mixture flowing through the chamber for a sufficient duration. The gas feed was controlled using two mass flow controllers (1179AX and MF1 series, MKS Instruments, Andover, MA, USA). Each of them was connected to one of the three gas containers: oxygen (O_2), nitrogen (N_2) and argon (Ar). Hence, variety of the binary mixtures out of these gases was made. The purity of the feed gases was at least 99.995%. The combined maximum gas flow rate was kept constant at 4000 standard cubic centimeters per minute (sccm) for all conditions. The individual flow rate of each controllers was adjusted according to the required gas mixture ratio. The fraction f_i of the partial gas i is described as following

$$f_i = \frac{\Gamma_i}{\Gamma_i + \Gamma_j} = \frac{\Gamma_i}{\Gamma_{total}} , \qquad i, j = \{O_2, N_2, Ar\} , \tag{2.1}$$

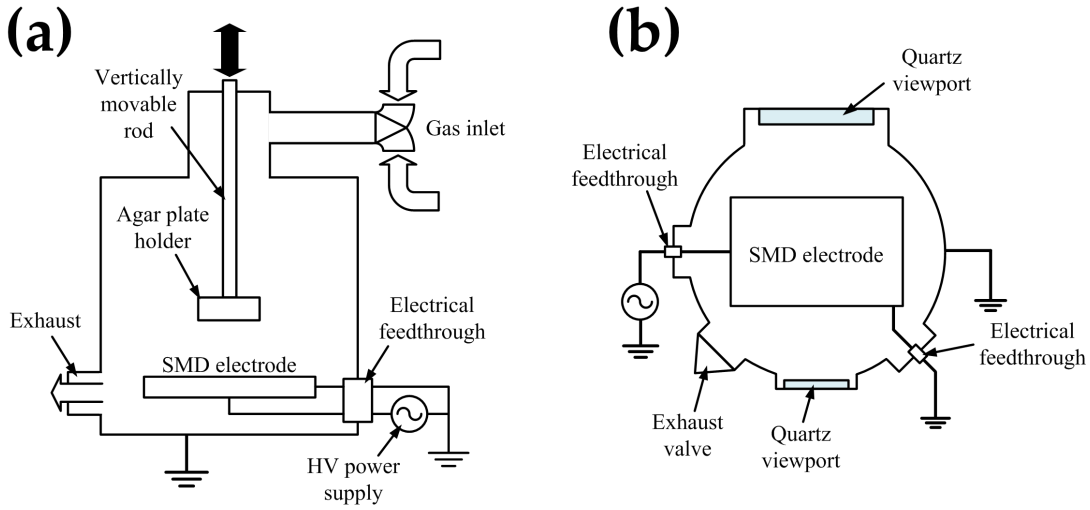

Figure 2.1 Sketch of the cross section view of the chamber. (a) side view, and (b) top view.

where Γ_i is the respective gas flow rate of the gas i and Γ_{total} the combined total gas flow rate (4000 sccm). The gas feed duration was determined by means of mass spectrometry (QMS 100 series Gas Analyzer, Stanford Research Systems, Sunnyvale, CA, USA). Here, the chamber was filled with pure N_2 without any admixture and the time evolution of the N_2 concentration was measured. The time was recorded when the chamber was saturated with N_2. Afterwards the chamber was filled with pure O_2 and the saturation duration for the O_2 concentration in the chamber was measured. This procedure was repeated several times. As the result, the average saturation time of approx. 210 seconds was found. It was within the computed range for a 99.9% saturation with the feed gas from the modeling and calculation by Brandt [204]. Therefore, 90 seconds of time puffer were added and the gas feed duration of 300 seconds was chosen.

The humidity was measured using a hygrometer (GFTB 100, Greisinger Electronic GmbH, Regenstauf, Germany) placed inside the closed chamber during the gas feed and the plasma treatment. Both the relative humidity and the water content in

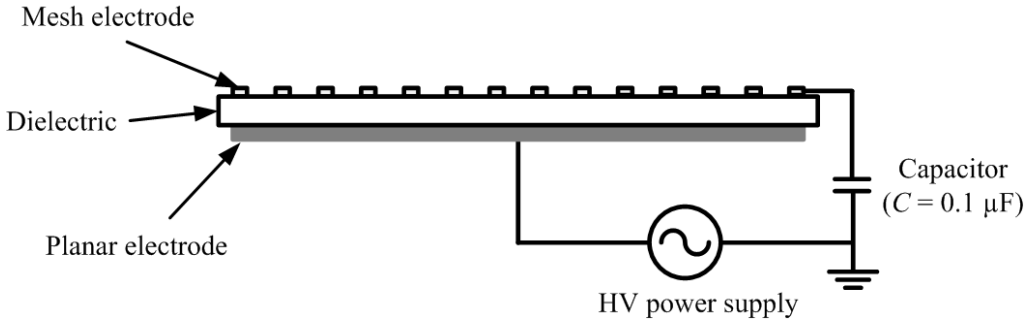

Figure 2.2 Schematic view of the SMD electrode with electric connections.

the gas were displayed. The humidity also saturated after around around 210 seconds. The relative humidity in the room ranged 35 - 60 % and the absolute water content 5.5 - 10 g/m^3. The humidity inside the chamber decreased during the gas feed below 9% in relative humidity corresponding to 2 g/m^3 in water content.

2.1.2 SMD Plasma Generation and Power Dissipation

The SMD electrode comprised a polytetrafluoroethylene (PTFE, Teflon®) dielectric, a stainless steel mesh grid and a planar aluminum electrode. The mesh electrode and the planar electrode are attached to the dielectric on each side, as shown in Figure 2.2, and is embedded in a polyoxymethylene (POM) frame. A sinusoidal waveform was applied using a function generator (HM8150, HAMEG Instruments GmbH, Mainhausen, Germany) and amplified by an amplifier (10/10B, TREK Inc., Medina, NY, USA). In the following, the function generator and amplifier are jointly referred to as the power supply.

The material and measures of the dielectric, the mesh electrode and the planar electrode are summarized in the Table 2.1. The planar electrode was connected to the power supply and the mesh electrode was grounded. A peak-to peak voltage of 6.5 to 10 kV$_{pp}$ was applied at the fixed frequency of 1.0 kHz. Microdischarges emerged

Table 2.1 Material and measures of the SMD components

	material	thickness	length x width
dielectric	PTFE	0.5 mm	145 mm x 105 mm
mesh electrode	stainless steel	1.5 mm	145 mm x 105 mm
planar electrode	aluminum	$\approx$ 0.05 mm	124 mm x 85 mm

between the mesh electrode and the dielectric surface when the high voltage was applied.

The consumption of the input power at the SMD electrode was determined by measuring the voltage drop across a capacitor connected in series between the mesh electrode and the ground (see Figure 2.2). The power consumption was calculated using the Lissajous-figure method, as proposed by Manley in 1943 [205] and described in details by Kogelschatz et al. [147,180]. In general, the electric power is calculated by integrating the product of the voltage and frequency over time. The power consumption $\overline{P}$ averaged over the period of the applied frequency $1/f$ is

$$\overline{P} = f \int_{t_0}^{t_0+\frac{1}{f}} U_0 \cdot I \;\; \mathrm{d}t \,, \tag{2.2}$$

where t_0 is the time offset, U_0 the input voltage, I the electric current via microdischarges and t time. The electric current I is the time derivative of the charge of the capacitor Q which, in turn, is the product of the capacitance C and the voltage drop U across the capacitor,

$$I = \frac{\mathrm{d}Q}{\mathrm{d}t} \quad \Rightarrow \quad I \,\mathrm{d}t = \mathrm{d}Q = C \,\mathrm{d}U \,. \tag{2.3}$$

Hence, the average power consumption at the SMD electrode measured by the voltage

drop across the capacitor is

$$\overline{P} = f\,C \int_{t_0}^{t_0+\frac{1}{f}} U_0 \,\mathrm{d}U\,. \tag{2.4}$$

Plotting U against the input voltage U_0 results in a closed parallelogram. The area of this Lissajous-figure equals the integral term in equation (2.4) and thus it is direct proportional to the averaged power consumption $\overline{P}$. Typical characteristic curves of the SMD are shown in Figure 2.3. Alternatively to using the Lissajous-figure method, the electric current from the SMD electrode could be directly measured using an inductive current meter (Model 6585, Pearson Electronics Inc., USA). Figure 2.3(a) shows the input voltage and the SMD electric current. Each peak in the current indicates the accumulation of microdischarges in the respective time interval. Current peaks of up to $\sim$ 30 mA were registered. The input voltage and the voltage drop across the capacitor are shown in Figure 2.3(b). The latter had the shape of a slightly distorted sine. A small phase shift was observed between the input power and the voltage drop. The waveform was slightly distorted from the sinusoidal curve due to the charging at the capacitor by the micro-discharges. Figure 2.3(c) shows the voltage drop from Figure 2.3(b) plotted against the input voltage. The shape of this Lissajous-figure is nearly a parallelogram. The area was calculated in order to determine the power consumption according to equation (2.4). Note that this Lissajous-figure was obtained by averaging over 512 samples in order to obtain an averaged power consumption by the plasma discharge.

Figure 2.4(a) shows the calculated power consumption at different voltages using 100% of each O_2, N_2 and Ar with the fixed frequency of 1.0 kHz. The curves of the power consumption show parabolic shapes. The highest power consumption was observed using 100% Ar as feed gas while no large difference in power consumption was found below 7.5 kV_{pp} using 100% O_2 and 100% N_2. A bifurcation of O_2 and N_2 curves was found at higher voltages. The power consumption using different gas mixtures with both the voltage and the frequency fixed (6.5 kV_{pp} and 1 kHz, respectively)

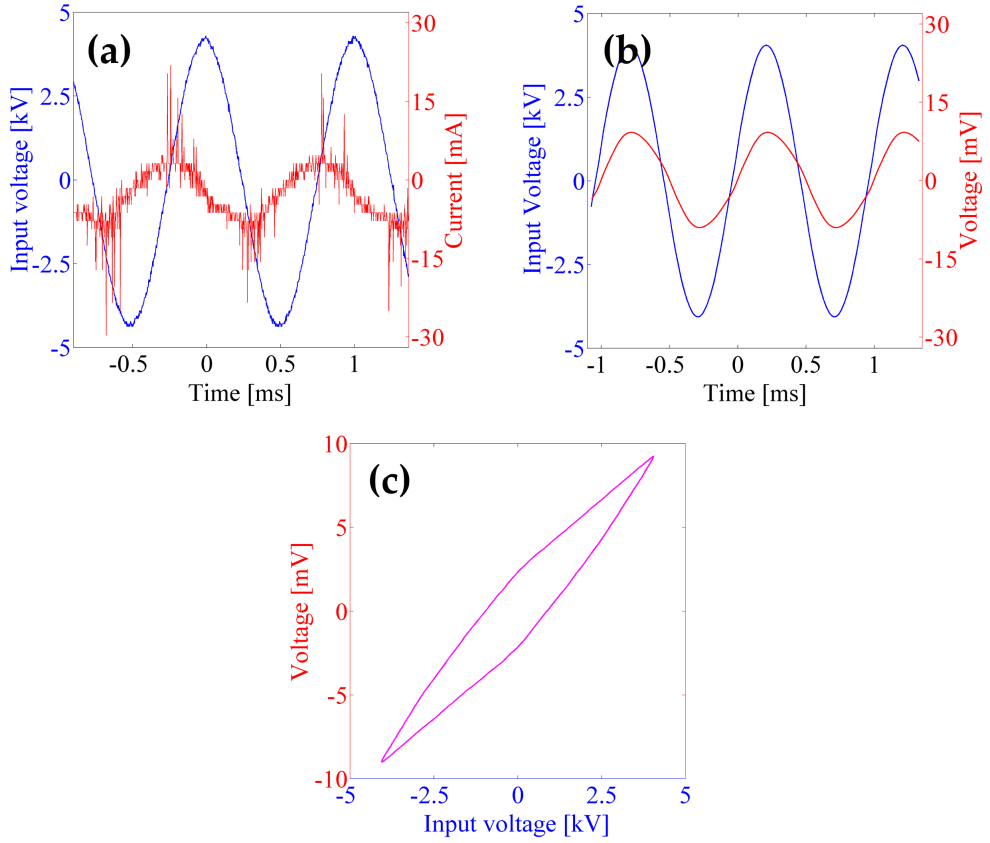

Figure 2.3 Typical characteristic curves of the SMD electrode. (a) input voltage and directly measured electric current, (b) input voltage and the voltage drop across the capacitor ($C = 0.1\mu$F), (c) voltage across the capacitor against input voltage (Lissajous-figure).

is shown in Figure 2.4(b). Here, the horizontal axis indicates either the O_2 fraction (for O_2 + N_2 and O_2 + Ar mixtures) or the N_2 fraction (for N_2 + Ar mixtures). The error bars correspond to the respective standard deviation of the results from 3 measurements. The calculated power consumption increased strongly with the fraction of Ar in the gas composition. In O_2 and N_2 (O_2 + N_2) mixtures, the power consumption did not change much at different mixture ratios. The power consumption was approximately twice as high using 100% Ar as using O_2, N_2 or a mixture of both.

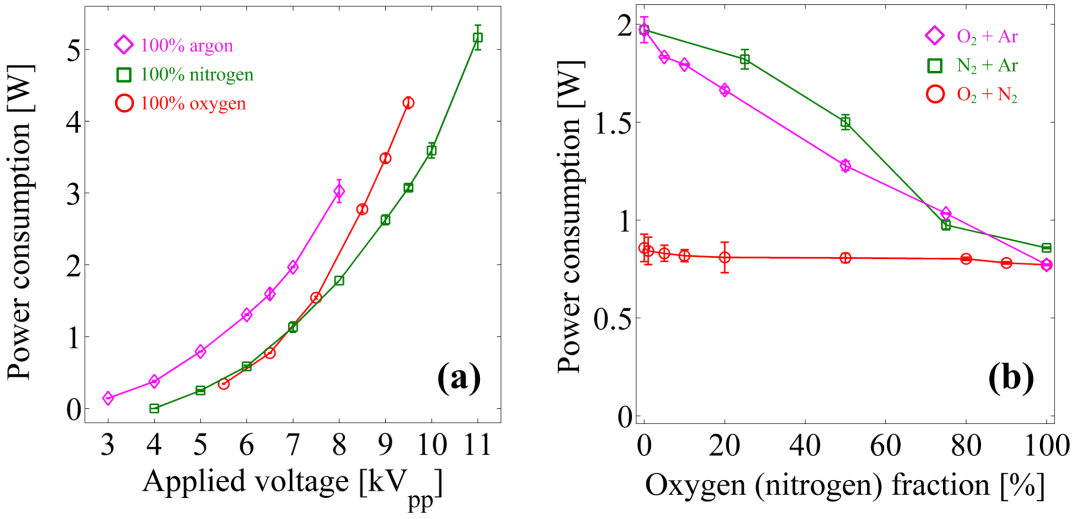

Figure 2.4 Power consumption at the SMD electrode calculated by the Lissajous-figure method. (a) each of the feed gases (Ar, N_2 and O_2) without admixtures at different voltages, (b) gas mixtures at different mixture ratios. In (b), the horizontal axis indicates either the O_2 fraction (for O_2 + Ar and O_2 + N_2 mixtures) or the N_2 fraction (for N_2 + O_2 mixtures). The applied frequency was kept constant at 1 kHz.

With increasing Ar fraction f_{Ar} and increasing power consumption, the probability of the formation of spark discharges also increased. The spark discharges occurred around the dielectric instead of passing through it and produced a short circuit between the high voltage electrode and the mesh electrode. The spark discharge was an undesirable instability in this study because of the inhomogeneous occurrence and the large power dissipation. In 100% Ar background gas, applying voltages higher than 6.5 kV_{pp} resulted in a frequent formation of sparks. To avoid the spark formation, the applied voltage did not exceed 6.5 kV_{pp} with 100% Ar and the corresponding power consumption of 2 W under this condition was set for the experiments at constant power consumption. The temperature increase at the SMD electrode was measured after 30 seconds of plasma generation at different input powers. Even at the highest applied input power of $\sim$ 2 W, the temperature increase did not exceed 4°C, so that the

inactivation of the bacteria by heat from the plasma can be excluded.

2.1.3 Ozone Measurement via Optical Absorption Spectroscopy

One of the well known long-lifetime reactive species is ozone. As mentioned in 1.7.5, DBD was first invented as ozone generator [120] and consequently the SMD, based on DBD, is able to produce ozone in large amounts. The concentration of ozone inside the chamber was measured via optical absorption spectroscopy. The incident UV light was supplied by a Hg/Ar light source (AVAST Avalight-CAL, Avantes BV, Apeldorn, the Netherlands) at the wavelength of 254 nm, which lies in the optimal range for the absorption of photons by ozone molecules [206–208]. The UV light beam was aligned parallel to the SMD electrode at approx. 5 mm height from the SMD electrode matching the distance of the bacterial sample on the agar plate. The transmitted light signal was recorded by a spectrometer (AVAST Avaspec-2048-USB2, Avantes BV) through an optical fiber. Two apertures with the diameter of 1.0 mm were placed in front of each the detector and the light source for the sake of better convergence. As previously mentioned, the light beam passed through the chamber via two opposing quartz viewports. Inside the chamber, a quartz cylinder of 30 mm inner diameter and $\sim$ 6 mm height was mounted to the vertically movable rod instead of the agar plate holder. During the gas feed, the quartz cylinder was detached from the SMD electrode by pulling up the rod. After the gas feed, the rod was lowered down until the quartz cylinder was placed on the top of the SMD electrode. By this procedure, the gas composition in the closed volume formed by the SMD electrode and the quartz glass cylinder was fully exchanged. Moreover, the formed closed volume was well confined and the products inside did not escape, i.e. the ozone concentration only inside the closed volume was measured. The UV light traversed the volume enclosed by the quartz tube and was absorbed by the ozone inside. Figure 2.5(a) shows the schematic cross section view of the chamber with respect to the absorption spectroscopy.

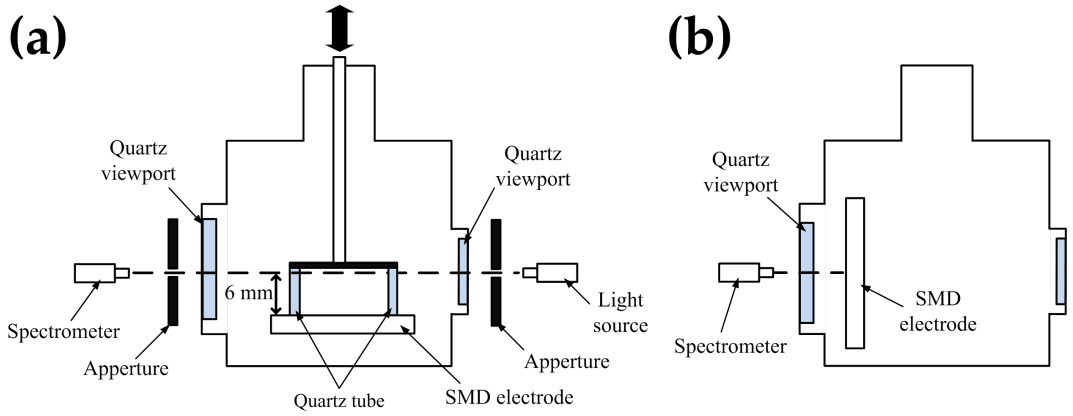

Figure 2.5 Sketch of the cross section view of the chamber with respect to the optical absorption spectroscopy setup (a) and optical emission spectroscopy setup (b).

The measured light signal was integrated over the wavelength from 253.5 to 254.5 nm. The integration time for the time evolutions was set to 1 second. The time evolution was recorded for 120 seconds after the plasma ignition. The concentration of ozone was calculated based on the Beer-Lambert Law. The intensity of light dI absorbed by particles in a volume defined by the absorption cross section σ, the particle density N and the length of the light path dx is

$$\mathrm{d}I = -IN\sigma\mathrm{d}x \quad \Rightarrow \quad \frac{\mathrm{d}I}{I} = -N\sigma\mathrm{d}x\,. \tag{2.5}$$

Integration over x results in

$$\ln(I) = -N\sigma x + \mathcal{C}\,, \tag{2.6}$$

where $\mathcal{C}$ is a constant of integration. The boundary condition finally leads to

$$I(x=0) = I_0 \quad \Rightarrow \quad \mathcal{C} = \ln(I_0) \quad \Rightarrow \quad N(I) = \frac{1}{\sigma x}\,\ln\left(\frac{I_0}{I}\right)\,, \tag{2.7}$$

where I_0 is the transmitted light intensity through the quartz viewports without ozone, i.e. before the ignition of the SMD plasma (t $\leq$ 0). The computed particle number was

converted into the concentration of ozone with the unit of ppm under the assumption of ideal background gases (number density $\sim 2.5 \times 10^{25}$ m^{-3}). A detailed description of the measurement techniques and calculation of ozone concentration via UV absorption spectroscopy is given by Samson [209]. In the wavelength range of $\sim$ 254 nm, the ozone absorption cross section reaches the maximum of $\sim 1.15 \times 10^{-17}$cm^2, as reviewed by Hudson [210] and Molina [211]. Additionally, the ozone concentration was averaged over 30 seconds ($\overline{n}_{O3}$) according to the bacterial treatment and plotted against the O_2 fraction in the gas composition. The production rate of ozone was estimated by means of the slope of the ozone time evolution immediately after the plasma ignition.

2.1.4 Optical Emission Spectroscopy and Discharge Photographs

The emission spectra from the SMD electrode were recorded using a UV/VIS spectrometer (TM-UV/VIS, Hamamatsu Photonics, Hamamatsu, Japan) within a wavelength range of 200 - 800 nm. Additionally, the UV radiation power was measured in the UVC range ($\sim$ 180 - 270 nm) using a UV power meter (C8026/H8025, Hamamatsu Electronics, Hamamatsu, Japan) at a distance of $\sim$ 6 mm. The measured UV power was below $\sim$ 100 nW/cm^2, leading to a UV dose of 10^{-6} to 10^{-5} mJ/cm^2 under the conditions of this study. This dose is by several orders of magnitude lower than the lethal dose for microorganisms as previously mentioned [30, 34].

For the emission spectroscopy, the SMD electrode was held vertically in front of the viewport, as shown in Figure 2.5(b). The photographs of the SMD plasma at different gas compositions are shown in Figure 2.6. The photographs were made using a digital camera (Canon EOS 450D) with ISO-400, f/4 and 15 seconds of exposure time. For the sake of a better visibility, the brightness of the photographs was enhanced by a constant factor using an image editing program. The brightness of the plasma increased with decreasing O_2 admixture ratio. The area covered by the plasma grew

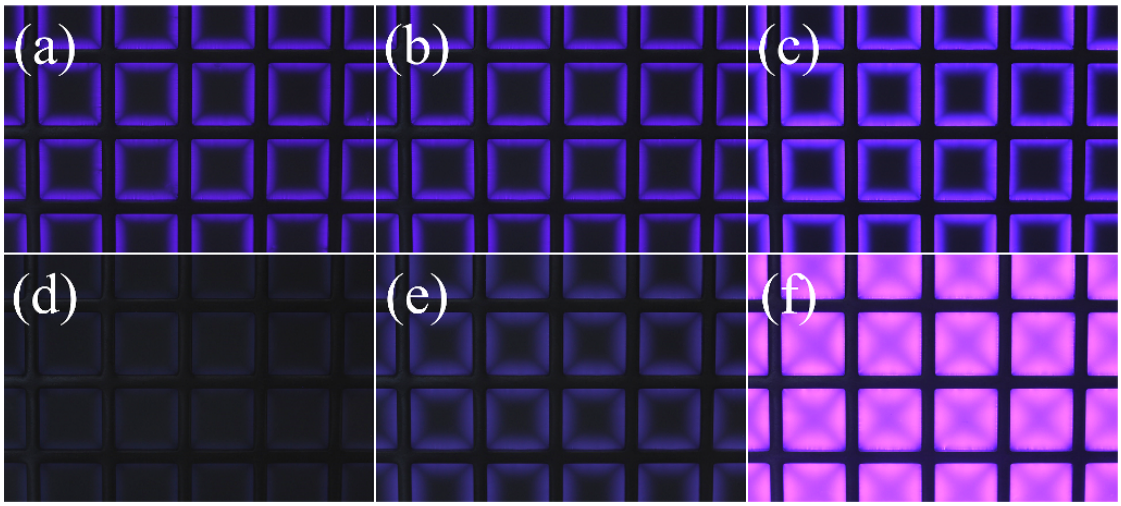

Figure 2.6 Photographs of the SMD plasma using different gas mixtures at the fixed power consumption of 2 W. (a) ambient air, (b) 20% O_2 + 80% N_2, (c) 100% N_2, (d) 100% O_2, (e) 20% O_2 + 80% Ar, and (f) 100% Ar. 15 seconds of exposure time, f/4 and ISO-400. The brightness was enhanced by a constant factor for all pictures.

strongly with increasing fraction of Ar in the gas composition, whereas it grew, if ever, only slightly with increasing N_2 fraction.

2.1.5 Bacterial Sample Preparation

Gram-negative *E. coli* DSM1116 and Gram-positive *Enterococcus mundtii* DSM3848 strains were used as bacterial indicators. Müller-Hinton (MH) agar filled in petri dishes with 85 mm in diameter was used as nutrient medium. The bacterial suspension was made by admixing a certain amount of bacteria to 5 or 10 ml of phosphate buffered saline (PBS) using an inoculating loop. For each experiment, a new bacterial suspension was made. Depending on the requirements, one dilution step or a cascade of dilution steps were made. The bacterial samples were prepared by inoculating 100 µl of the bacterial suspension onto the MH agar plates. The fluid was distributed over

the entire agar surface by smearing with a cell spreader. The preparation of the bacterial samples was performed following the standard procedures of the microbiology as described by Willey et al. [212] and Cappuccino and Sherman [213]. After the inoculation, the samples were kept open in the ambient air for $\sim$ 30 minutes until the sample surface was visibly dry.

2.1.6 Sample Treatment and Evaluation

Figure 2.7 shows the photograph of the chamber with the SMD electrode inside. The bacterial sample was fixed to the agar plate holder with the open side down. The chamber was then closed and the gas mixture was conducted into the chamber for 5 minutes with the exhaust valve opened. For the exchange of the gas between the bacterial sample and the SMD electrode, the agar plate was moved away from the SMD electrode by pulling up the rod during the gas feed. After the gas feed the valve was closed and the agar plate holder was lowered until the sample dish touched the SMD electrode. The gap between the samples on the agar surface and the SMD electrode was approx. 6 mm. Then the plasma was ignited by applying the high voltage. After the required duration the plasma was extinguished by switching off the power supply. The sample was immediately removed from the vicinity of the SMD electrode in order to minimize the bactericidal effects from the gases containing the long-lifetime species produced by the plasma, the so-called afterglow.

After the treatment, the bacterial samples were kept in an incubator at 36°C for at least 16 hours. After the incubation the colony forming units (CFUs) were counted. The bacterial reduction was determined by comparing the numbers of CFUs with those of the untreated samples.

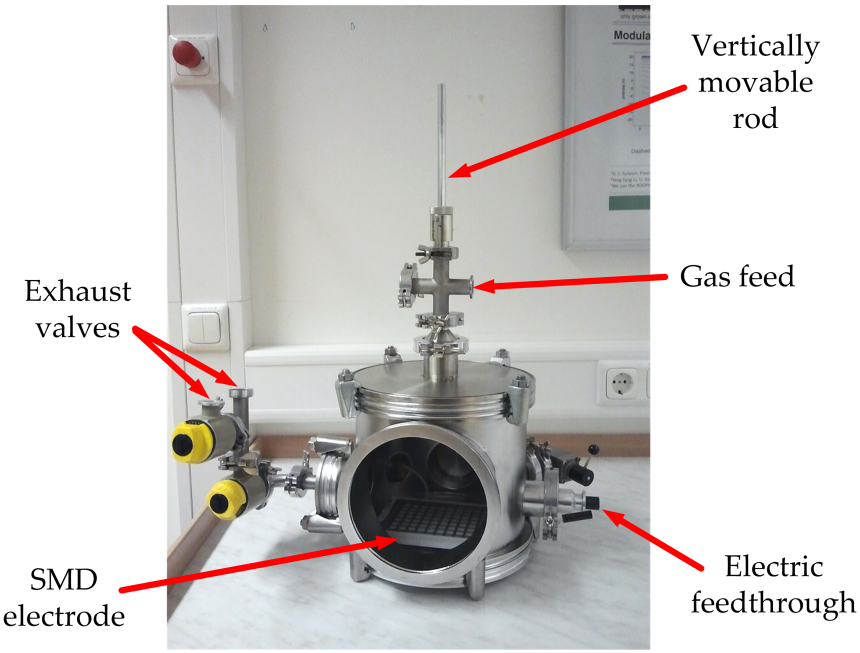

Figure 2.7 Photograph of the vacuum-sealable chamber with the SMD electrode inside.

2.2 Results

2.2.1 Emission Spectra

Figure 2.8 shows the emission spectra from the SMD using different O_2 + N_2 gas mixtures. The intensity is in an arbitrary unit but consistent in all four plots. The strongly pronounced peaks in the wavelength range of 300 - 400 nm are the emission lines of the N_2 second positive system [214]. The intensity of the peaks decrease rapidly with increasing O_2 fraction in the gas composition. An increase of the O_2 fraction to 50% resulted in an intensity fall of almost 2 orders of magnitude. The emission lines of the N_2 second positive system were observed from SMD plasmas using 100% O_2 as well (see Figure 2.8). It was assumed that a small amount of N_2 residue remained in the chamber, e.g. at the surface of the chamber wall and the SMD electrode, after 5

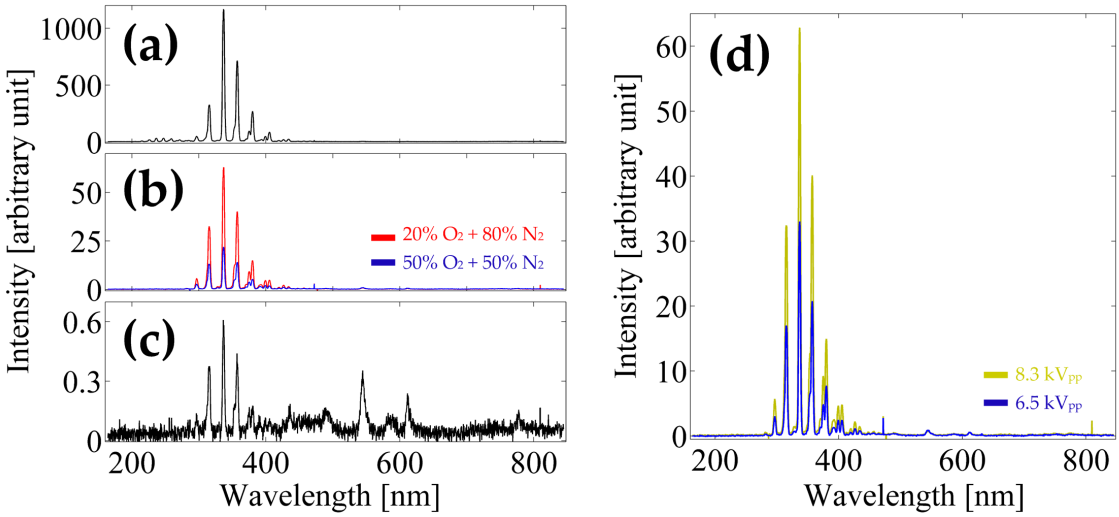

Figure 2.8 Emission spectra from the SMD plasma using different O_2 + N_2 gas mixtures. (a)-(c) at constant power consumption of 2 W; (a) 100% N_2, (b) 20% O_2 + 80% N_2 (red) and 50% O_2 + 50% N_2 (blue), (c) 100% O_2. (d) 20% O_2 + 80% N_2 at different voltages 6.5 kV_{pp} and 8.3 kV_{pp}. The intensity is displayed in a consistent arbitrary unit for all four plots.

minutes of gas exchange. However, the intensity was negligibly low with the intensity unit at 0.1 - 0.5. Compared with the intensity of $\sim$ 1000, the estimated fraction of N_2 in gases without N_2 admixture was $\sim 10^{-4}$.

Figure 2.8(d) shows the emission spectra from SMD plasmas using 20% O_2 + 80% N_2 at different voltages 6.5 kV_{pp} and 8.3 kV_{pp}. The lines appear at the same wavelengths but the emission intensity was higher at the higher voltage of 8.3 kV_{pp}.

The emission spectra from O_2 + Ar mixture plasmas resembled those of the O_2 + N_2 plasmas due to the remaining N_2 in the chamber (data now shown). Because of the high electron density in Ar and Ar mixture plasmas and due to the very high luminosity, the emission lines of the N_2 second positive system were dominant. The characteristic Ar emission lines were observed at the wavelengths $\geq$ 700 nm [215].

2.2.2 Ozone Concentration

The time evolutions of the ozone concentration produced by the SMD plasma using different gas mixtures are shown in Figure 2.9. Here, the ozone concentrations from SMD plasmas using different O_2 + N_2 mixtures are shown where (a) the applied voltage is kept constant at 6.5 kV_{pp}, (b) the power consumption was kept constant at 2 W and (c) the applied voltage was kept constant at 10 kV_{pp}, corresponding to power consumptions of 3 W or more. The ozone concentration saturated within less than 30 seconds after the plasma ignition. The ozone concentration was near zero when 100% N_2 or 100% Ar was used as background gas. Both the production rate, indicated by the slope of the curve near $t = 0$, and the saturation concentration of ozone increased with increasing O_2 fraction f_{O2}.

Figure 2.9(d) and (e) show the time evolutions using different O_2 + Ar gas mixture plasmas at the fixed voltage of 6.5 kV_{pp} and at the fixed power consumption of 2 W, respectively. While the saturation concentration and the production rate of ozone increase monotonically with increasing f_{O2} at constant power consumption, a maximum was found between 0.2 and 0.5 in O_2 fraction if the applied voltage was fixed. This is explained by the balance between the power consumption and the O_2 fraction in the gas composition. The more O_2 was added to the background gas, the less power consumption was, as shown in Figure 2.4. On the other hand, O_2 is necessary for the formation of ozone by the three-body reaction [189, 190]

$$O + O_2 + M \quad \longrightarrow \quad O_3 + M\,, \tag{R1}$$

where M is the third body. Additionally, the production of atomic oxygen O as well depends on the concentration of O_2 via

$$O_2 + e^- \quad \longrightarrow \quad O + O + e^-\,. \tag{R2}$$

In total, the electron density in the plasma depends on the Ar fraction, while the ozone production reaction itself depends on the O_2 fraction. Hence, a maximum of ozone yield appears at a certain O_2/Ar mixture ratio. The ozone concentrations at different humidities are compared in Figure 2.9(f), where the plasma was generated in the dry feed gas of 20% O_2 + 80% N_2 and in ambient air at two different voltages 6.5 kV_{pp} and 10 kV_{pp}. Lower saturation concentration was observed using ambient air as background gas at both voltages. Possible explanations are that, firstly, ozone react with water-related species such as H, OH•, OH^- etc., and secondly, the electrons from the plasma react with water and hydrogen-associated species and the yield of the oxygen atoms by the electron dissociation is reduced [190].

Figure 2.10(a) shows the ozone production rates from the SMD plasma using various gas mixtures (O_2 + N_2 and O_2 + Ar) at different O_2 fractions f_{O2}. Using O_2 + N_2 gas mixtures, the ozone production rate increased monotonically under all three conditions (6.5 and 10 kV_{pp} and 2 W) as f_{O2} increased. With the power consumption fixed at 2 W, the ozone production rate from O_2 + Ar mixture plasmas also increased monotonically as f_{O2} increased. A maximum of ozone production rate was observed from O_2 + Ar mixture plasmas at constant voltage of 6.5 kV_{pp}. This is due to the balance between the electron density and the availability of atomic and molecular oxygen as discussed previously on the basis of the time evolution curves.

2.2.3 Survival Curves

For the evaluation of the bactericidal kinetics, the bacterial samples were exposed to the SMD plasma using various background gases for different durations from 5 to 120 seconds with the power consumption kept constant at 2 W. Figure 2.11 shows the survival curves of *E. coli* using four chosen feed gases 100% O_2, 20% O_2 + 80% Ar, 20% O_2 + 80% N_2 and ambient air. Additionally, the survival curves using 100% N_2 and 100% Ar were also measured but are not shown, since no distinguishable reduc-

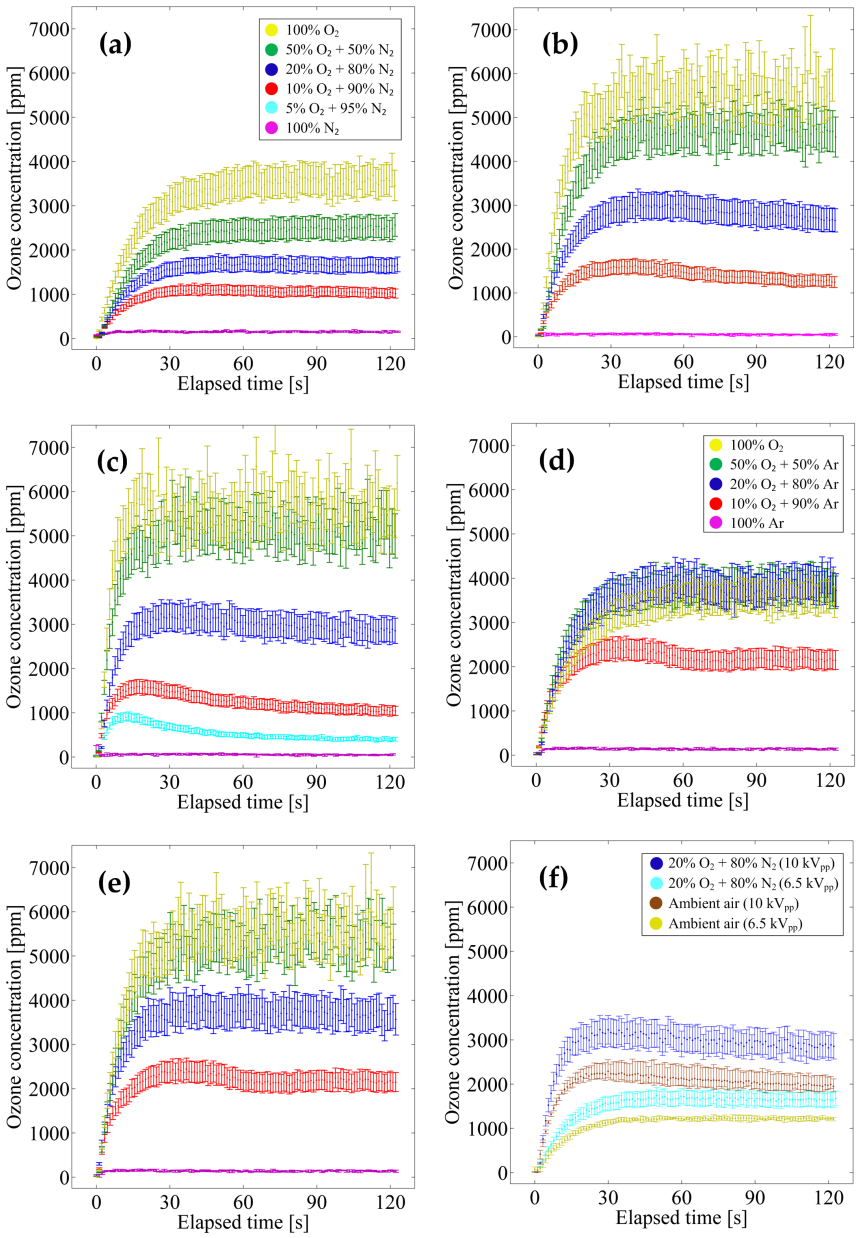

Figure 2.9 Time evolution of the ozone concentration. (a) O_2 + N_2 mixture plasmas at fixed voltage of 6.5 kV_{pp}, (b) O_2 + N_2 mixture plasmas at fixed power of 2 W, (c) O_2 + N_2 mixture plasmas at fixed voltage of 10 kV_{pp}, (d) O_2 + Ar mixture plasmas at fixed voltage of 6.5 kV_{pp}, (e) O_2 + Ar mixture plasmas at fixed power of 2 W, (f) synthetic air (20% O_2 + 80% N_2) plasma and ambient air plasma at two different voltages 6.5 kV_{pp} and 10 $_{pp}$. (a)-(c) share the same legend, as well as (d) and (e).

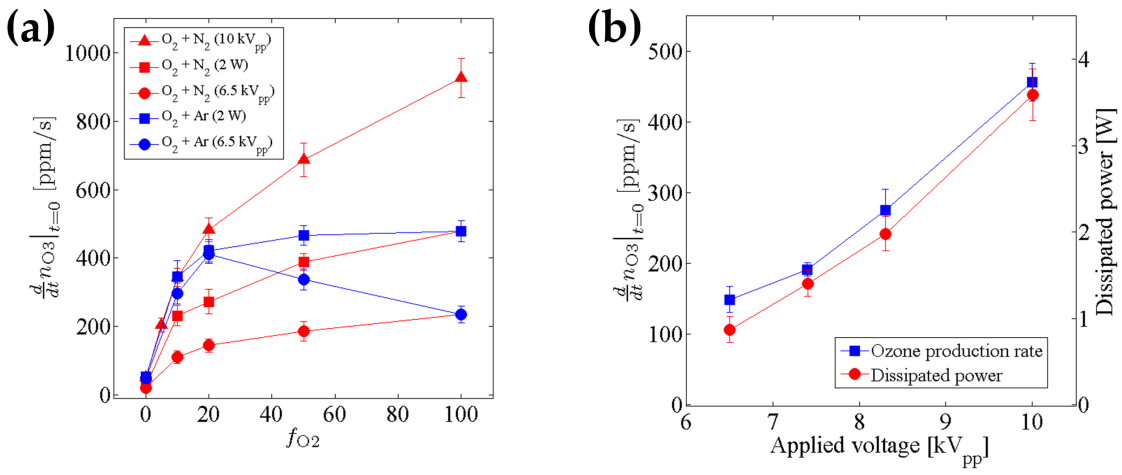

Figure 2.10 Ozone production rates from the SMD plasma. (a) using $O_2 + N_2$ and O_2 + Ar gas mixtures with different O_2 fractions f_{O2} at fixed voltages (6.5 and 10 kV $_{pp}$) and fixed power consumption (2 W), (b) dependency on the applied voltage, comparison with the power consumption using 20% O_2 + 80% N_2.

tion of bacteria was observed ($\leq$ 0.2 log) after up to 5 minutes of plasma exposure. Two different inactivation phases were observed at all four survival curves. In the first phase below $\sim$ 30 seconds, the reduction of bacteria was fast with 4 - 4.5 log reduction within 30 seconds. In the following phase, the bacterial reduction was slower with a reduction increase of less than 1 log over 90 seconds. The highest reduction of *E. coli* was observed from 100% O_2 plasma, followed by the O_2 + Ar and O_2 + N_2 mixture plasmas with f_{O2} = 0.2. Although there was no large difference in the bacterial reduction at fixed f_{O2}, the least bactericidal efficacy was obtained using ambient air.

2.2.4 Inactivation of *E. coli* by N_2 + Ar Mixture Plasmas

The SMD plasma was generated using N_2 + Ar gas mixtures with different mix ratios (N_2 fraction $f_{N2} = 0, 0.25, 0.5, 0.75, 1$) as background gas. The bacterial samples of both *E. coli* and *Enterococcus mundtii* were exposed to the plasma. The first experi-

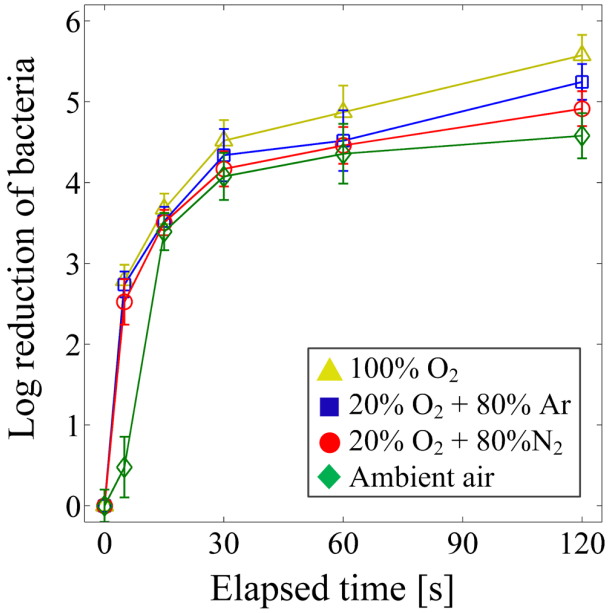

Figure 2.11 Survival curves of *E. coli* after the exposure to the SMD plasma using different background gases at the constant power consumption of 2 W.

ments with 30 seconds of exposure duration showed no bactericidal effect using any of the N_2 + Ar mixtures. Even after increased exposure durations of up to 5 minutes, no bactericidal effect was observed.

2.2.5 Inactivation of *E. coli* by O_2 + N_2 Mixture Plasmas

The *E. coli* bacterial samples were exposed to the SMD plasma for 30 seconds using O_2 + N_2 gas mixtures with different O_2 fractions ($f_{O2} = 0, 0.05, 0.1, 0.2, 0.5, 1$). The plasma parameters were varied in three different ways: Either the applied voltage was kept constant at 6.5 or 10 kV_{pp}, or the power consumption was fixed at 2 W. Figure 2.12 shows the reduction of the bacteria on logarithmic scale. In absence of O_2 in the gas composition ($f_{O2} = 0$) no bactericidal effect was observed under all three conditions (6.5 kV_{pp}, 10 kV_{pp} and 2 W). As the O_2 fraction was increased, the bacterial reduction

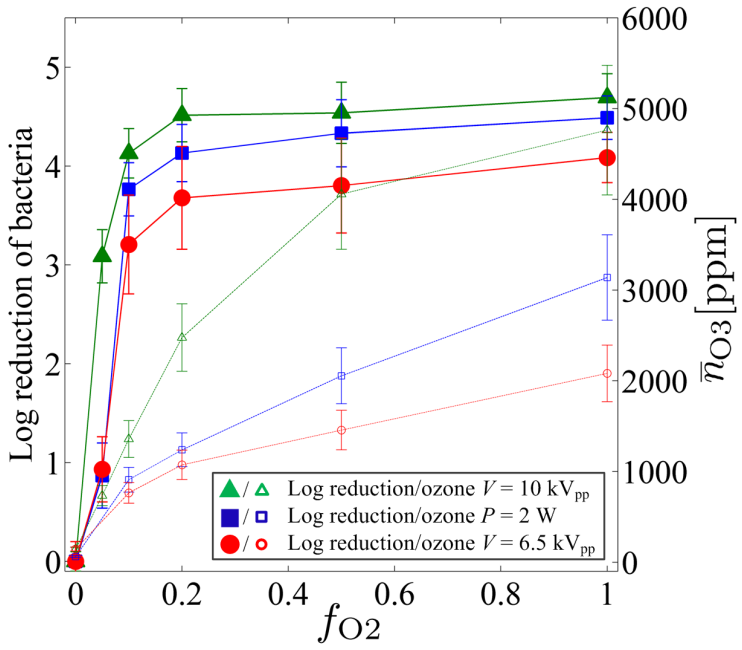

Figure 2.12 Reduction of *E. coli* bacteria after 30 seconds of SMD plasma treatment using $O_2 + N_2$ gas mixtures at different mixture ratios. Either the applied voltage was kept constant at 6.5 and 10 kV_{pp} or the power consumption at 2 W.

increased rapidly up to 3.5 to 4.5 log until f_{O2} reached ≈ 0.2. A further increase of f_{O2} did not result in a significant increase of the bactericidal efficacy (≤ 0.2 log). For the visualization of the correlation of the bactericidal efficacy with the ozone production, the ozone concentrations in 30 seconds average, $\overline{n}_{O3}$, are plotted in the same diagram. $\overline{n}_{O3}$, too, showed two phases of different slopes with the transition at $f_{O2} \approx 0.2$. For low O_2 fractions, $f_{O2} \leq 0.2$, the increase of $\overline{n}_{O3}$ with increasing f_{O2} was fast. For $f_{O2} \geq 0.2$, $\overline{n}_{O3}$ increased slower with increasing f_{O2} for all three conditions.

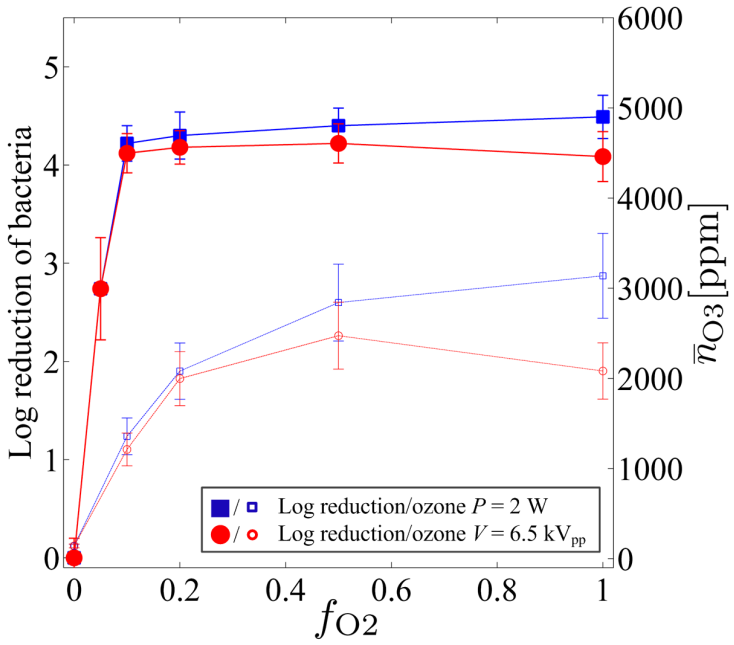

Figure 2.13 Reduction of *E. coli* bacteria after 30 seconds of SMD treatment using O_2 + Ar gas mixtures at different mixture ratios. Either the applied voltage was kept constant at 6.5 kV_{pp} or the power consumption at 2 W.

2.2.6 Inactivation of *E. coli* by O_2 + Ar Mixture Plasmas

The *E. coli* bacterial samples were exposed to the SMD plasma using O_2 + Ar gas mixtures with different mixture ratios for 30 seconds. Either the power was kept constant at 2 W or a fixed voltage of 6.5 kV_{pp} was applied. f_{O2} was changed between 0, 0.05, 0.1, 0.2, 0.5 and 1. The log reduction of the bacteria after the SMD plasma treatment is shown in Figure 2.13. The corresponding ozone concentrations in 30 seconds average, $\overline{n}_{O3}$, are shown in the same figure. It was assumed that all gas molecules moved with the same thermal velocity which was constant during the SMD plasma treatment. Under this condition, the mass flow of ozone molecules onto the sample surface was proportional to the averaged concentration of ozone.

No bactericidal effect and no ozone concentration were measured at $f_{O2} = 0$. As

f_{O2} was increased up to 0.1, the bacterial reduction increased strongly by more than 4 logs for both conditions. For higher values of f_{O2} up to 1, the bacterial reduction increased insignificantly ($\leq$ 0.2 log) at the fixed power consumption of 2 W. With the applied voltage fixed at 6.5 kV_{pp}, the bacterial reduction increased minimally by $\sim$ 0.1 log as f_{O2} increased from 0.1 to 0.5. The bacterial reduction decreased slightly by $\sim$ 0.1 log as f_{O2} increased further up to 1.

At constant power consumption of 2 W, $\overline{n}_{O3}$ increased monotonically with increasing f_{O2}. Two phases were observed with a strong increase for $f_{O2} \leq 0.2$ and a reduced increase at higher f_{O2}. With the applied voltage fixed, $\overline{n}_{O3}$ increased strongly with increasing f_{O2} until 0.2, then increased slightly until f_{O2} was at 0.5, and decreased as f_{O2} increased up to 1. In total, the shapes and tendencies of the bacterial reduction and of $\overline{n}_{O3}$ were similar.

2.2.7 Inactivation of *Enterococcus mundtii* by O_2/N_2/Ar Binary Mixture Plasmas

The samples of the Gram-positive bacteria *Enterococcus mundtii* were exposed to the SMD plasma using O_2 + N_2 and O_2 + Ar gas mixtures with different O_2 fractions in a similar way as for the tests with *E. coli*. The survival curves, as shown in Figure 2.14(a), were determined by changing the treatment duration from 5 to 120 seconds. Here, the samples were exposed to the SMD plasma from four different feed gases, 100% O_2, 20% O_2 + 80% Ar, 20% O_2 + 80% N_2 and ambient air. These experimental conditions were same as for *E. coli* samples as shown in Figure 2.11. The power consumption was kept constant at 2 W. The bacterial reduction increased rapidly in the first 5 seconds to 3 to 4 log. A transition phase was observed between 5 and 30 seconds of exposure duration where the bacterial reduction increased by $\sim$ 1 log within 25 seconds. As the treatment duration was increased from 30 to 120 seconds, the bacterial

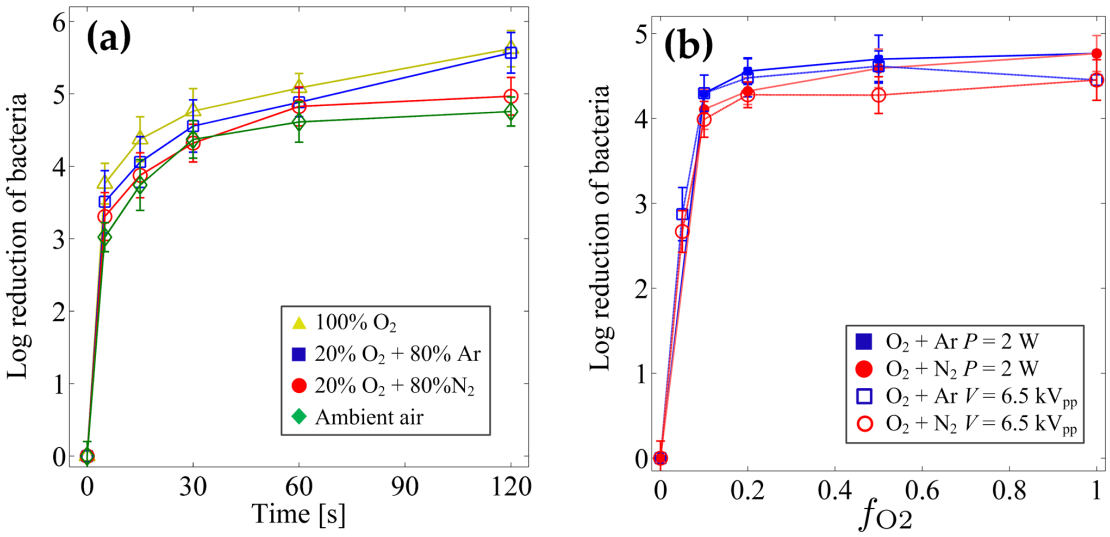

Figure 2.14 Reduction of *Enterococcus mundtii* bacteria by the exposure to the SMD plasma using various O_2 + N_2 and O_2 + Ar gas mixtures. (a) survival curves using four selected gas compositions at the constant power consumption of 2 W, (b) after 30 seconds of SMD plasma treatment at different O_2 fractions f_{O2} at the fixed voltage of 6.5 kV_{pp} and at the constant power consumption of 2 W.

reduction increased by $\sim$ 1 log using 100% and 20% O_2 + 80% Ar as feed gas, whereas it nearly stagnated using 20% O_2 + 80% N_2 and ambient air.

Figure 2.14(b) shows the reduction of *Enterococcus mundtii* bacteria after 30 seconds of exposure to the SMD plasma using O_2 + N_2 and O_2 + Ar gas mixtures at different f_{O2}. Here, either the power consumption was kept constant at 2 W or a fixed voltage of 6.5 kV_{pp} was applied. No bactericidal effect was observed without O_2 admixture (f_{O2} = 0). The bacterial reduction increased strongly as f_{O2} increased from 0 to 0.1 and increased by 0.2 to 0.3 as f_{O2} increased from 0.1 to 0.2. With a further increase of f_{O2} from 0.2 to 1, the bacterial reduction at constant power consumption increased slightly for both gas mixtures. At the fixed voltage of 6.5 kV_{pp}, the bacterial reduction using O_2 + N_2 mixtures increased with increasing f_{O2}, whereas a maximum of bacterial reduction was found at f_{O2} = 0.5 if O_2 + Ar mixtures were used.

In total, both the survival curves and the bacterial reduction after 30 seconds of treatment using different gas compositions showed the same tendency as from the results with *E. coli*.

2.3 Discussion

The temperature increase and the UV radiation power from the SMD plasma were found far below the lethal level for the microorganisms. The short-lifetime reactive species cannot reach the sample surface due to the gap of 6 mm between the SMD plasma and the sample surface with no gas flow. Thus, the contribution of heat, UV radiation and short-lifetime reactive species to the bactericidal effect was excluded and the search for the bactericidal agents from the SMD plasma was narrowed down to the long-lifetime reactive species. First of all, no microbiocidal effect on both Gram-negative *E. coli* and Gram-positive *Enterococcus mundtii* bacteria strains was observed after 30 seconds of SMD plasma treatment if no O_2 was admixed to the feed gas. This indicates that, in the parameter range investigated in this study, the bacterial reduction was due to the reactive species that comprise oxygen.

In order to compare the bactericidal effect of the SMD plasma using O_2 + N_2 and O_2 + Ar mixtures as feed gas, the reduction of *E. coli* and $\overline{n}_{O3}$ were re-arranged. Figure 2.15(a) shows the curves at the fixed voltage of 6.5 kV_{pp} and Figure 2.15(b) at the constant power consumption of 2 W. Under the both conditions, higher bactericidal efficacy was observed using O_2 + Ar than using the corresponding O_2 + N_2 gas mixtures as feed gas. Additionally, the bactericidal efficacy increases as the N_2 fraction decreases. Hence, it was concluded that nitrogen reactive species contribute little to the inactivation of bacteria by the SMD plasma.

Ar molecules possess full valence electron orbitals and are chemically more stable than N_2 molecules. In comparison with N_2 plasma, Ar plasma shows a higher

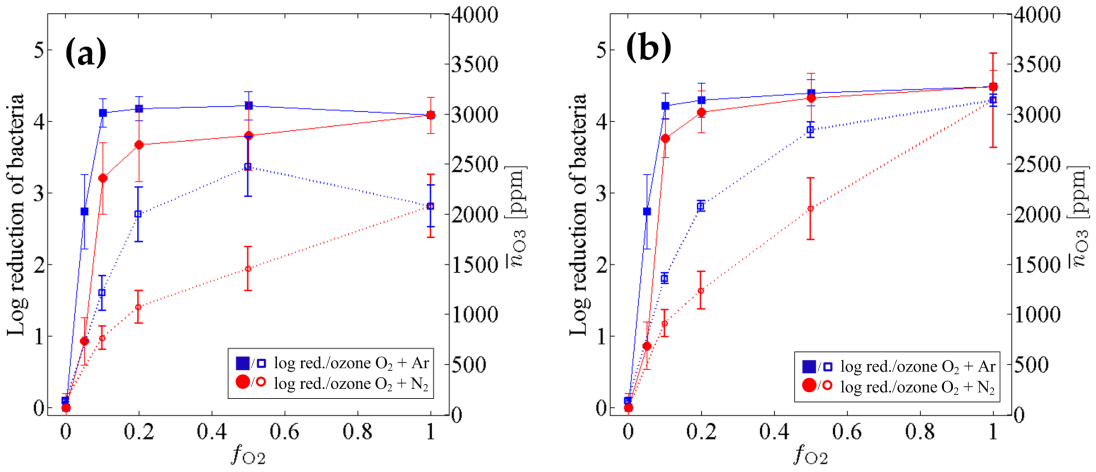

Figure 2.15 Reduction of *E. coli* after 30 seconds of SMD plasma exposure and the ozone concentration in 30 seconds average. Comparison of O_2 + N_2 and O_2 + Ar gas mixture plasmas. (a) at the fixed voltage of 6.5 kV_{pp}, (b) at the constant power consumption of 2 W.

electron density because there are less electron loss mechanisms such as dissociation and activation processes. Therefore, O_2 + Ar plasmas have a higher electron density than O_2 + N_2 plasmas at a fixed power consumption and at the same f_{O2}, which results in a higher number density of atomic oxygen and ozone. In addition, the fraction of N_2 in O_2 + N_2 gas mixtures reduced the ozone production and enhanced the quenching of ozone in comparison with Ar fraction in O_2 + Ar gas mixtures. According to the plasma chemistry model developed by Shimizu et al. [165], the ozone molecules can be quenched by oxidizing nitrogen based-molecules, especially nitrogen oxides (NO, NO_2). Moreover, the same averaged ozone concentrations resulted in more or less same bactericidal property regardless of the feed gas composition. For instance, at the constant power consumption of 2 W, O_2 + Ar plasma at f_{O2} = 0.1 and O_2 + N_2 plasma at f_{O2} = 0.2 match in both bacterial reduction and averaged ozone concentration. The same tendency was shown e.g. by O_2 + Ar plasma at f_{O2} = 0.2 and O_2 + N_2 plasma at f_{O2} = 0.4.

The tendencies of the curves of the bacterial reduction and $\overline{n}_{O3}$ show a good correlation both at the fixed voltage and at the constant power consumption. The increase of the bacterial reduction was associated with the increase of $\overline{n}_{O3}$. If $\overline{n}_{O3}$ decreased, as shown at O_2 + Ar mixture plasmas at 6.5 kV_{pp} for f_{O2} = 0.5 - 1, the bactericidal efficacy decreased, too. The slopes of both curves were found similar as well. It is important to note that the bacterial reduction is plotted on logarithmic scale, whereas $\overline{n}_{O3}$ is on linear scale. The time-dependent curves of the ozone concentration and the bacterial reduction also overlapped. The survival curves (Figure 2.11 and 2.14(a)) showed a strong increase of the bactericidal effect in the first 30 seconds after the plasma ignition, followed by a slight increase for longer treatment durations. The ozone concentration, as demonstrated by the time evolutions in Figure 2.9, increased strongly in the first 20 - 30 seconds after the plasma ignition and saturated.

In total, the observations from this study support the idea of regarding ozone as the mainly responsible agent for the bactericidal effect of the SMD plasma under the investigated conditions. A good correlation between the ozone concentration and the bacterial reduction was found. Both the ozone concentration and the bacterial reduction increased either by increasing the power consumption or by raising the O_2 fraction f_{O2}. The results and the conclusions are in agreement with those presented by Shimizu et al. [165], as mentioned in the previous chapter (see Figure 1.8).

It is possible, for instance, that ozone reacted with the water vapor diffused off the agar surface to produce water-related reactive species such as OH• that are strong sterilants.

Despite of the different scaling of the bacterial reduction and $\overline{n}_{O3}$, the sharp bend in the bacterial reduction stands opposed to the smooth bend of the averaged ozone concentration. This is possibly due to the two-phased inactivation of the bacteria, suggesting that multiple mechanisms involved in the bactericidal effect of the SMD plasma. However, the results do not evidence that ozone alone is responsible for the bactericidal effect by the SMD plasma treatment. It is possible that other reac-

tive species apart from ozone were involved as well or even mainly responsible for the bacterial inactivation. The evaporation of water from the agar sample surface can lead to the formation of water-related reactive species such as hydrogen peroxide and hydroxyl radicals. Furthermore, the bactericidal effect on both Gram-negative *E. coli* and on Gram-positive *Enterococcus mundtii* was similar despite of the different cell structures of the microorganisms. This observation is in accordance with the results from a study by Klämpfl et al. [155], where similar bactericidal effect was observed on different vegetative bacterial indicators. No plausible explanations for these observations have been found yet and further detailed investigations are required.

Chapter 3

Sporicidal Properties of SMD under Different Humidity Conditions

3.1 Bacterial Endospores

Bacterial endospores are dormant, highly resistant and non-proliferating form of some (usually Gram-positive) bacteria. The transformation of a vegetative bacterium in an endospore, termed sporulation, mostly occurs in absence of nutrients (carbon, nitrogen or phosphate) in the vicinity [216–218]. The endospore transforms back to the vegetative form if the environment is suitable for metabolism and proliferation.

A number of experiments have proven that bacterial endospores can withstand extreme terrestrial and extraterrestrial conditions including wet/dry heat, (solar and cosmic) UV and gamma radiation, desiccation, vacuum pressures ($\sim 10^{-7}$ Pa) and oxidative damage for long periods of time (up to hundreds of days) without nutrition, as summarized in several reviews [219–221]. These observations have given rise to panspermia, the theory that microorganisms are distributed throughout the universe by traveling on or under the surface of meteoroids, asteroids, comets and planetoids [222]. In addition, it is believed that contamination with bacterial endospores on the surface of spacecrafts can lead to an undesirable transport of microorganisms e.g. to other planets. Therefore, the decontamination of the spacecraft and the equipment for the space missions has become an intensively studied research topic [223–225].

The high resistance of bacterial endospores are due to the multilayer structure, the characteristic mineral content, the formation of dipicolinic acids (DPA) and the small acid-soluble proteins (SASPs) and the capability of DNA repair [220, 226–228].

3.1.1 Multilayer Structure

The bacterial endospore has a different cell structure than the corresponding vegetative bacterium. Characteristic for the endospores are the multiple layers protect-

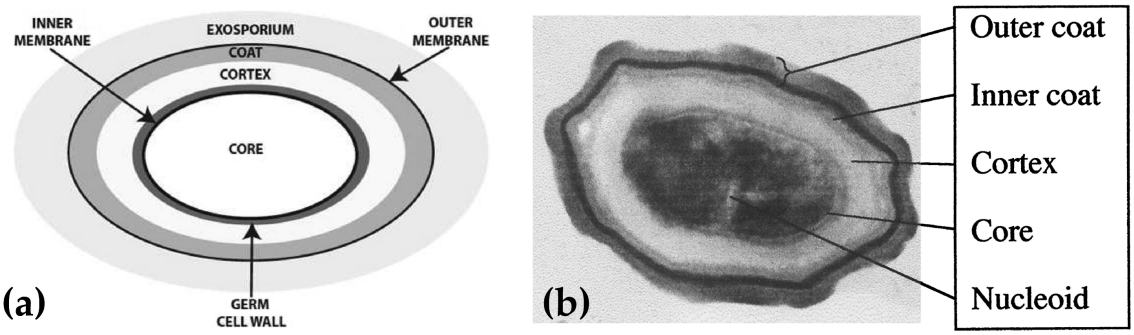

Figure 3.1 Structure of a endospore of *Bacillus* species. (a) schematic view, drawn to scale (note: spores of many species do not have an exosporium), (b) cross-section of a spore of *B. subtilis*, electron micrograph. *From Yardimci and Setlow* [227] *and Nicholson et al.* [220].

ing the spore's core. From the outside inward, the layers are composed of the exosporium, the coat, the outer membrane, the cortex and the inner membrane. The schematic view and an electron micrograph showing the cross-section of a *Bacillus* endospore are shown in Figure 3.1(a) and (b), respectively. The exosporium is the loose-fitting outermost layer of the endospore of *Bacillus cereus* and some other species. Many endospore-forming bacteria such as *G. stearothermophilus* and *B. subtilis* either do not possess the exosporium or contain an exosporium with a greatly reduced size [229, 230]. The exosporium consists of proteins, including some glycoproteins that are characteristic for exosporium-containing endospores [228, 229, 231, 232]. The function of the proteins in the exosporium is unknown. The coat is a complex structure that comprises several layers and consists of tens of mostly spore-specific proteins [226, 228, 231, 233]. Even though the individual roles of the coat's proteins are unknown, it has been found that the coat protects the endospore from some chemical agents and from exogenous lytic enzymes [220, 233] The outer membrane appears not to contribute to the resistance of the bacterial endospore, though it is essential for the sporulation and germination [220, 234]. The cortex consists of peptidoglycan and plays an important role in the reduction of the water content in the endospore's core [235–237]. A low water con-

tent in the core enhances the resistance to wet heat and peroxide species [238, 239]. It has been demonstrated that the water content in the core of an endospore is greatly reduced (28 - 50% of the wet weight) while the water content in the outer layers is similar to that in growing cells (75 - 80% of the wet weight) [236, 237]. The inner membrane of an endospore functions as a strong permeability barrier and protects the core from chemical agents [220, 240].

3.1.2 Mineral Content

Bender and Marquis [241] presented procedures to completely exchange the mineral content in the endospore cells in a controlled way without affecting the viability. They tested a variety of mineral cations on the endospores of *Bacillus megaterium*, *B. subtilis niger* and *G. stearothermophilus* strains and concluded that the resistance to wet heat increased using H^+, Na^+, K^+, Mg^{2+}, Mn^{2+} and Ca^{2+}, in ascending order. They noted that the protection from wet heat was reduced using H^+ and Na^+ in comparison with other mineral cations but still more effective than that of the corresponding vegetative cells. Beaman and Gerhardt [238] suggested that mineral cations replace water in biopolymers of the cell core by intercalation and thus enhance the dehydration and the protection from heat.

3.1.3 Dipicolinic Acid (DPA)

Pyridine-2,6-dicarboxylic acid, or dipicolinic acid (DPA), comprises 5 - 15% of the dry weight of an endospore and is located in the core. Figure 3.2 shows the structure of the DPA. DPA chelates most of the divalent cations, especially Ca^{2+}, and reduces the water content in the endospore's core [220, 226, 242] Furthermore, Magge et al. [243] observed that the endospore cells initiate the germination process and thus degrade the protection if the concentration of DPA falls below a critical level.

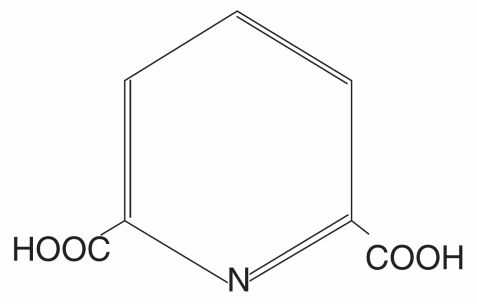

Figure 3.2 Structure of the dipicolinic acid (DPA).

3.1.4 Small Acid-Soluble Proteins (SASPs)

The DNA of an endospore is saturated with α/β type small acid-soluble proteins (SASPs) that are characteristic for the bacterial endospores. The SASPs are synthesized in an abundant amount ($\sim 5\%$ of total spore protein) in the late of the sporulation phase and degraded in the beginning of the germination phase [220, 244]. These proteins are mostly bound to the outside of the DNA helix and changes the DNA's structure and properties dramatically. In this way, the SASPs increase the endospore's resistance to heat, reactive chemicals and UV radiation [244].

3.1.5 DNA Repair

Bacterial endospores are metabolically dormant without enzyme activity and damage inflicted to DNA or proteins is accumulated without being repaired in this state. Though, the DNA repair enzymes are activated during the germination and outgrowth phase of the endospore and DNA and protein damage can be repaired to a great extent [235, 245]. Two pathways for the DNA repair of endospores, namely the excision and the monomerization of the spore photoproducts formed within the DNA by UV irradiation, have been described by Fajardo-Cavazos et al. [246]. Setlow [247]

compared the UV sensibility of various wild-type *Bacillus* endospores and their mutations without the the capability of DNA repair and observed enhanced UV inactivation of the latter.

3.1.6 Bacerial Endospores as Biological Indicator

Due to the protective properties described in the previous sections, bacterial endospores are highly resistant to toxic chemicals, wet and dry heat and UV radiation. The difficulty of inactivation of bacterial endospores makes them a good indicator for the evaluation of sterilizing methods. The most frequently used bacterial endospores as biological indicator are *B. atrophaeus*, *B. cereus*, *B. subtilis* and *G. stearothermophilus*, but also *Bacillus anthracis*, which are considered as potential biological weapons [248, 249].

3.1.7 *Geobacillus stearothermophilus*

A number of previous studies have demonstrated the sporicidal effect of CAPs on different bacterial endospore strains [155, 250–252]. Several comparative studies [253–255] concluded that, despite different experimental conditions, *G. stearothermophilus* endospores are among the most resistant species to the plasma treatment and therefore appropriate biological indicator for assessment of the microbiocidal effect of the plasma [227]. In the following chapters, the term "spore" is used instead of bacterial endospore.

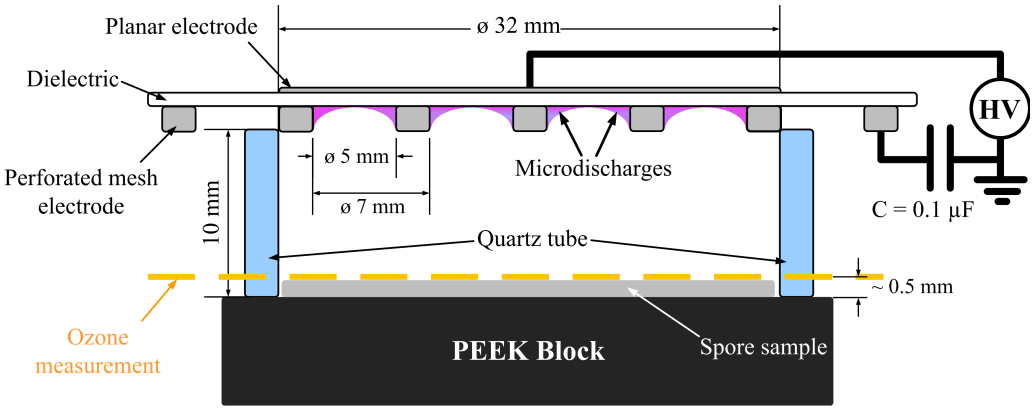

Figure 3.3 Schematic view of the SMD electrode setup with the electric connections and the ozone measurement layer.

3.2 Experimental Setup

3.2.1 Plasma Generation

The SMD plasma generator incorporated an aluminum sheet as planar electrode, a ceramic plate (Al_2O_3) as dielectric and a stainless perforated plate as mesh electrode. The power supply comprised an amplifier (PM4015, TREK Inc., Lockport, USA) and a function generator (HM8150, HAMEG Instruments GmbH, Mainhausen, Germany). The electric current was measured using an inductive current meter (Model 6585, Pearson Electronics Inc., USA). Additionally, an additional capacitor with the capacitance of 0.1 µF was connected in series between the mesh electrode and the ground for the measurement of the power consumption via the Lissajous-figure method as described in the previous chapter. Figure 3.3 shows the schematic view of the SMD electrode including the electric connections, the measures and the position of the light beam for the absorption spectroscopy. The powered electrode was cut in circular shape with a diameter of 30 mm and was attached onto the dielectric. The thickness of the dielectric was 0.75 mm. The mesh electrode, 1.5 mm in thickness, was attached on the oppo-

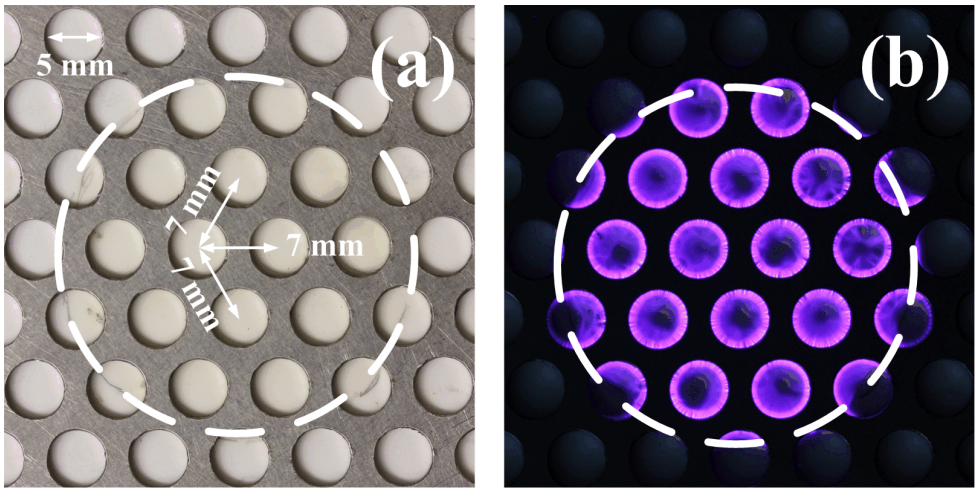

Figure 3.4 Top view of the SMD electrode. (a) no discharge and (b) with plasma ignited at 6.8 kV_{pp} and 3.0 kHz ($\sim$ 5 W, 15 seconds exposure time, f/4, ISO-400, brightness enhanced). The white dashed circles indicate the position of the planar electrode on the the reverse side of the dielectric.

site side of the dielectric. Both the dielectric and the mesh electrode were in square shape with a side length of 100 mm. The uniformly circular-shaped openings in the mesh electrode were arranged in a hexagonal pattern with the lattice spacing of 7 mm. The diameter of the opening measured 5 mm. The top view photograph of the mesh electrode is shown in Figure 3.4(a).

High voltage with a sinusoidal waveform was generated by the power supply and applied to the planar electrode. The applied voltage was fixed at 6.8 kV_{pp} and the frequency was varied from 100 Hz up to 10.0 kHz. The input voltage, the electric current and the voltage drop over the capacitor were monitored by an oscilloscope (7000B Series, Agilent Technologies, Santa Clara, CA, USA). The total power consumption at the SMD electrode varied between 0.15 and 14 W. Figure 3.4(b) shows a photograph of the SMD electrode after the ignition of the plasma at 3.0 kHz, corresponding to a power consumption of $\sim$ 5 W. The photograph was taken using 15 seconds of exposure time, f/4 and ISO-400. The brightness was enhanced by an image editing software.

3.2.2 Handling and Treatment of the Spore Samples

The *G. stearothermophilus* spore samples were prepared by drying a certain amount of spore suspension in a saline solution on the surface of rectangular stainless steel plates with the dimensions 30 mm $\times$ 6 mm $\times$ 0.5 mm (provided by SIMICON GmbH, Munich, Germany). According to the specification given by the manufacturer, the number of spores on each sample was $\sim 1.5 \times 10^6$. For the SMD plasma treatment of the spores, the sample was placed on the top of a polyether ether keptone (PEEK) block as shown in Figure 3.3. PEEK was chosen as sample holder because of its high resistance to electrical and thermal influences. A cylindrical quartz tube with the inner diameter of 32 mm and the height of 10 mm was placed around the sample. The SMD electrode was then placed on top of the quartz tube with the mesh electrode down and the planar electrode matching exactly the position of the quartz tube (see Figure 3.3). In total, a closed cylindrical volume was confined by the PEEK block, the quartz tube and the SMD electrode with the spore sample inside.

For the comparison of different plasma parameters and humidities, the spore samples were exposed to the SMD plasma for 5 minutes. For the determination of the survival curves, the treatment duration was varied from 1 to 5 minutes. After the SMD plasma treatment, each spore sample was put into a sealable centrifuge tube with 5 ml of Ampuwa® (sterile and pyrogen-free water, Fresenius Kabi Deutschland GmbH). The spore cells were suspended by vortexing for 30 seconds, by ultrasonic-bathing for 20 minutes and by vortexing once again for 30 seconds. Dilution series were made from the suspension for the evaluation of the spore reduction by the SMD plasma treatment. 100 µl of the required suspension/dilution was inoculated onto a Tryptic Soy agar (TSA) plate (Thermo Fisher Scientific Inc., Waltham, MA, USA) and spread over the surface using a cell spreader. Then the agar plates were incubated at 55.5 °C for at least 16 hours. Three spore samples were treated for each experimental condition. The experiments were repeated at least 3 times for each condition. Untreated samples were

also processed in the described way in order to evaluate the initial number on the spore samples and the recovery rate after SMD plasma treatment.

3.2.3 Ozone Measurement via Optical Absorption Spectroscopy

As demonstrated in the previous chapter, ozone appeared to be involved in the inactivation of bacteria by the SMD plasma exposure. In order to investigate the chemical components present in the confined volume where the spore samples were treated, the concentration of ozone was monitored by optical absorption spectroscopy using the same setup as described previously. The ozone measurement was performed in the absence of a spore sample in the closed volume. The beam of UV light was aligned parallel to the surface of the PEEK block at a distance of 0.5 mm according to the surface height of the spore samples, as indicated in Figure 3.3. The measurement was repeated 3 times for each experimental condition and the mean value and the standard deviation were calculated.

3.2.4 Monitoring and Regulation of Humidity

The humidity was measured using the hygrometer mentioned in the previous chapter. Before and after the SMD plasma treatment, the SMD electrode was removed and the sensor of the hygrometer was positioned near the sample position. Then the volume was closed again and the humidity was recorded. Three different humidity conditions were applied for the spore treatment in this study, which are referred to as condition A, B and C with the respective humidity of ~ 5.5 g/m^3, ~ 10 g/m^3 and ~ 17 g/m^3. The conditions A and B were realized by choosing proper environmental conditions. The high humidity of ~ 17 g/m^3 under condition C was achieved by pipetting 40 µl of tap water onto the PEEK block and spreading it with a cell spreader. The ambient pressure was stable at 960 ± 10 hPa for all the experiments.

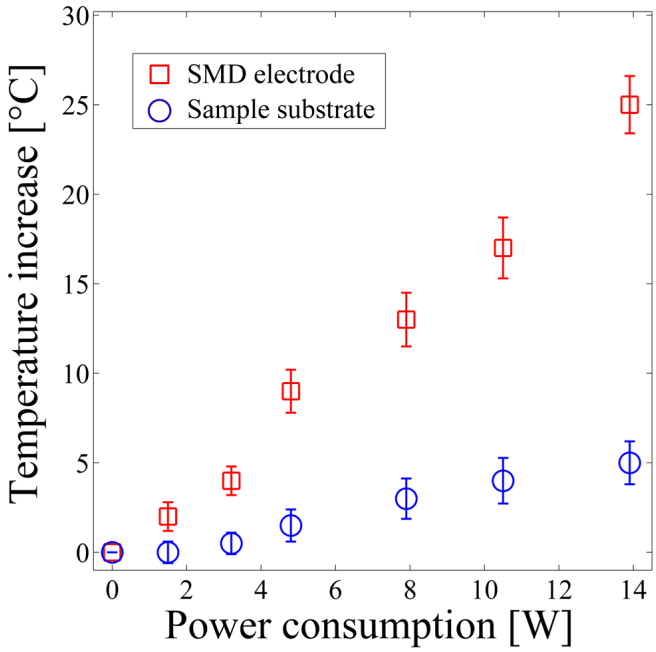

Figure 3.5 Temperature increase at the mesh electrode and at the sample position after 5 minutes of plasma generation. The initial temperature was $\sim$ 21 °C.

3.2.5 Measurement of Temperature

The temperature was measured both at the mesh electrode and at the sample position after 5 minutes of plasma generation using a type K thermocouple with a tip diameter of $\sim$ 0.6 mm. A stainless steel substrate without spores was placed at the sample position for the temperature measurement. Before the plasma ignition, the temperature at both locations was at room temperature, $\sim$ 21 °C. Figure 3.5 shows the temperature increase plotted against the power consumption. The error bars indicate the minimum and maximum values from three measurements. The temperature at the mesh electrode increased monotonically with increasing power consumption and reached $\sim$ 46 °C at the highest power consumption of 14 W. At the sample position, the temperature increase was much slower with a maximum increase of $\sim$ 5 °C at 14 W. *G.*

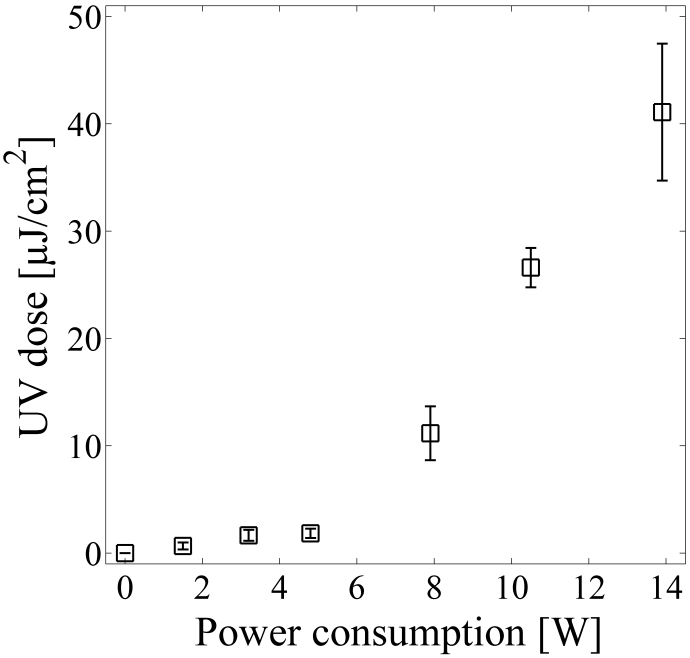

Figure 3.6 UV dose at 10 mm distance from the SMD electrode.

stearothermophilus spores are thermophile microorganisms that proliferate preferably at temperatures above 50 °C. Hence, the contribution of heat to the sporicidal effect of the SMD plasma was excluded in this study.

3.2.6 Measurement of UV Radiation Power

The UV radiation power was measured in the UVC-range using the previously introduced UV power meter. The power consumption was varied between 0 and 14 W. The UV dose was calculated by integrating the UV power over 5 minutes. Figure 3.6 shows the UV dose plotted against the power consumption. The UV dose was very low with ≤ 2 µJ/cm^2 (near detection limit) at low power consumption of below 5 W. As the power consumption was increased, the UV dose increased strongly up to ~ 40

$\mu J/cm^2$ at 14 W. Still, the measured doses were by several orders of magnitude smaller than the lethal doses $\sim 10\ mJ/cm^2$ for microorganisms [30,34,35] as mentioned in 1.5.3.

3.3 Results

First of all, the recovery from an untreated spore sample after processed in the described way was between 0.1 and 3.5×10^6 CFUs. Partly large fluctuation was observed which was possibly due to the fabrication procedures of the manufacturer and/or due to the thermal convection inside the closed volume. Klämpfl [256] presented scanning electron microscope (SEM) pictures of the untreated spore samples and pointed out the presence of the organic cell debris from the sporulation process as well as the NaCl crystals from the fabrication. In total, 33 untreated samples were evaluated and the average recovery from an untreated sample was $\sim 0.7 \times 10^6$ CFUs, about half as much as the manufacturer's specification. As mentioned previously, the different humidity levels are referred to as condition A ($\sim 5.5\ g/m^3$), condition B ($\sim 10\ g/m^3$) and condition C ($\sim 17\ g/m^3$).

3.3.1 Reduction of *G. stearothermophilus* after 5 Minutes of SMD Plasma Treatment

The reduction of *G. stearothermophilus* spores after 5 minutes of exposure to the SMD plasma with varied power consumption under different humidity conditions is illustrated in Figure 3.7. Here, the number of recovered CFUs after the SMD plasma treatment is shown in box plots, where the lower and upper edge of each box indicate the first and the third quartile, respectively. The horizontal line inside the box marks the median. The whiskers indicate 1.5 times of the interquartile range from the median

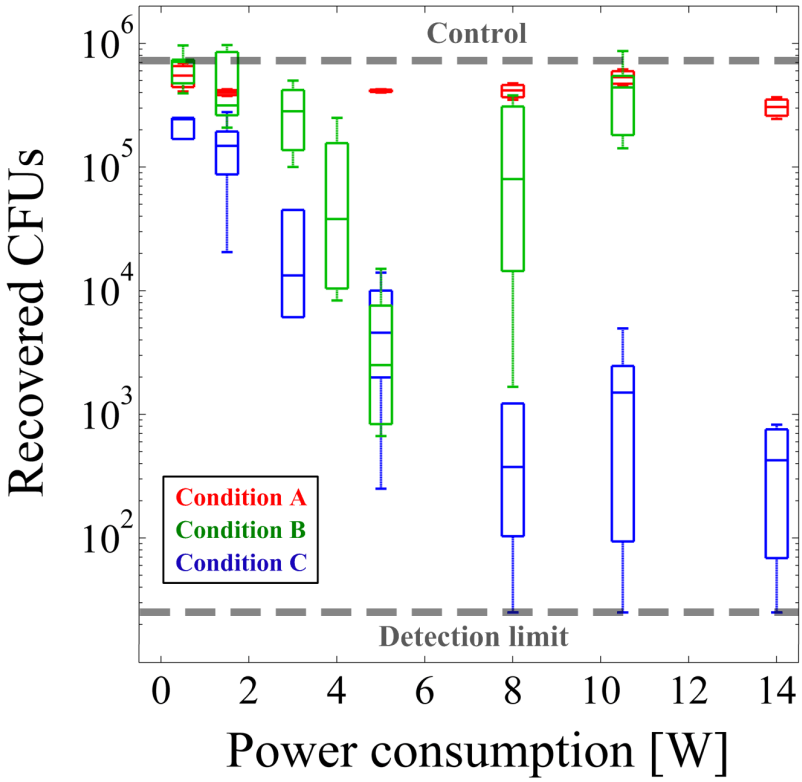

Figure 3.7 Reduction of *G. stearothermophilus* spores after 5 minutes of exposure to the SMD plasma with varied power consumption under different humidity conditions.

and cover together with the box 99.3% of the experimental data. The dashed horizontal bar in gray at 7×10^5 indicates the average recovery from the untreated samples. The lower detection limit due to the evaluation procedure was 25, as indicated by the dashed gray bar the at the bottom.

The reduction of spores was almost negligible ($\leq$ 0.5 log reduction) at low humidity under condition A in the entire power consumption range from 0.5 to 14 W. No large difference in the spore reduction was found as the power consumption was changed. Under condition B, the spore reduction was below 0.5 log at the lowest applied power consumption of 0.5 W. As the power consumption was increased from

0.5 to 5.0 W, the number of recovered spore CFUs decreased and the maximum spore reduction of 2.5 - 3 log was observed at 5.0 W of power consumption. The spore reduction decreased as the power consumption was increased further up to 14 W and almost no spore reduction was observed at the highest applied power consumption of 14 W. At the increased humidity under condition C, the sporicidal efficacy increased continuously from ≤ 1 log at 0.5 W to ≥ 3 log at 14 W. A large fluctuation of up to 1.5 log in the spore recovery after the SMD plasma treatment was observed under conditions B and C, whereas the fluctuation was comparably little under the condition A. The fluctuation of the experimental data is not understood yet. Since the experimental conditions for the plasma ignition were kept constant and stable for the given conditions, a possible explanation is provided by the altered chemistry e.g. from the surface modification at increased humidity. Further investigations are required to understand this observation properly.

3.3.2 Survival Curves of *G. stearothermophilus*

For the investigation of the kinetics of the spore reduction, the exposure duration of the spore samples to the SMD plasma was increased from 1 to 5 minutes. The power consumption was kept constant at 5.0 W where the maximum of spore reduction under condition B was found. The spore reduction under condition A was negligibly small at ≤ 0.5 log after up to 10 minutes of SMD plasma exposure. Figure 3.8 shows the survival curves of the spore samples after the SMD plasma treatment under condition B (a) and under condition C (b). The survival curve data under condition A are not shown. As shown in Figure 3.7, the spore reduction at 5.0 W was similar (~ 2.5 log) after 5 minutes of SMD plasma exposure under condition B and C. Under both humidity conditions, the survival curves showed a linear decrease (a single-phase reduction), indicating a single process of spore inactivation by the SMD plasma.

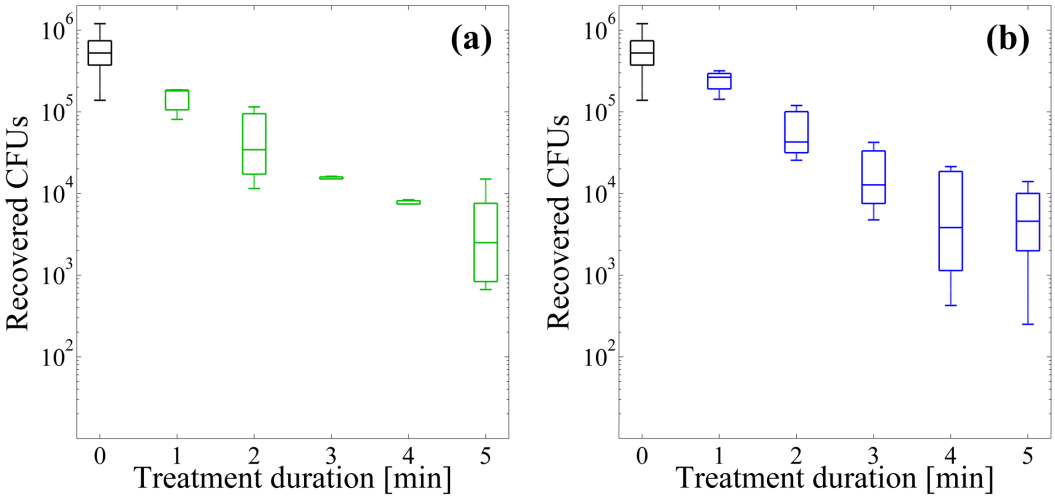

Figure 3.8 Reduction of *G. stearothermophilus* spores after different exposure durations to the SMD plasma treatment at the constant power consumption of 5.0 W. (a) under condition B ($\sim$ 10 g/m^3), (b) under condition C ($\geq$ 17 g/m^3)

3.3.3 Ozone Concentration

The concentration of ozone n_{O3} was measured to investigate the chemistry in the confined volume where the spore samples were treated with the SMD plasma. The time evolutions of n_{O3} at different power consumptions under condition A are shown in Figure 3.9. The error bars indicate the standard deviation from three independent measurements. Different ozone generation modes were observed depending on the power consumption. At the lowest applied power consumption of 0.1 W, n_{O3} increased slowly in the first 100 seconds after the plasma ignition and saturated at $\sim$ 500 ppm. At 0.5 and 1.5 W, n_{O3} increased rapidly in the first 50 - 60 seconds, reached a maximum, decreased slightly and saturated at 1500 - 2500 ppm. At higher power consumptions, n_{O3} rose rapidly within a initial duration that decreased with increasing power, reached a maximum and dropped to zero.

These observations were are qualitatively in agreement with the results pre-

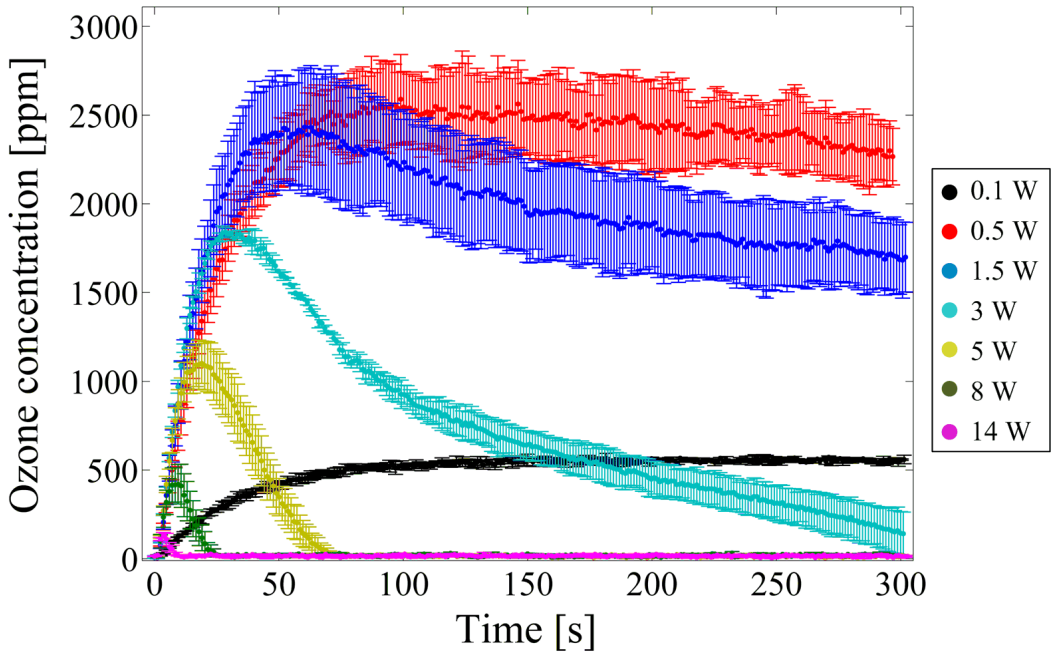

Figure 3.9 Time evolutions of the ozone concentration measured by the optical absorption spectroscopy under condition A ($\sim$ 5.5 g/m^3).

sented by Shimizu et al. [165]. Under condition B and C, the same ozone generation modes with similar curve shapes were observed, though the overall ozone concentration and the saturation level decreased with increasing humidity (data now shown). Based on the time evolution data, the averaged ozone concentration over 5 minutes $\overline{n}_{O3}$ was determined by integrating the time dependent ozone concentration n_{O3} over 5 minutes and dividing it by 5 minutes. Figure 3.10 shows $\overline{n}_{O3}$ plotted against the power consumption under different humidity conditions. The shapes of the curves were similar under all three humidity conditions. Starting near zero at 0.1 W, $\overline{n}_{O3}$ increased strongly with increasing power consumption. A maximum of $\overline{n}_{O3}$ was found at relatively small power consumptions between 0.5 and 1.5 W. As the power consumption was increased past 1.5 W, $\overline{n}_{O3}$ decreased monotonically and fell below 200 ppm for all humidity conditions at 5.0 W. At high power consumption above 8 W, $\overline{n}_{O3}$

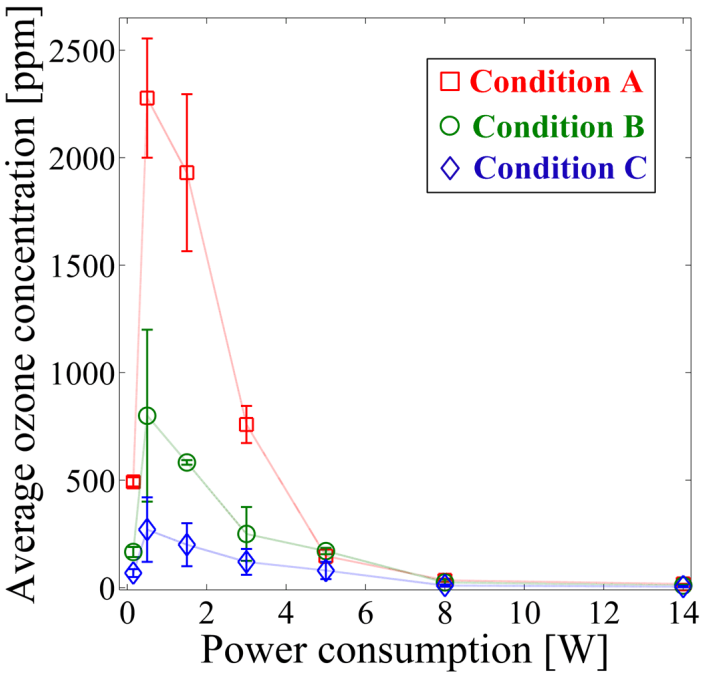

Figure 3.10 The ozone concentration averaged over 5 minutes under different humidity conditions.

approached zero ppm.

The overall values of $\overline{n}_{O3}$ decreased by almost one order of magnitude as the humidity was increased from $\sim$ 5.5 g/m^3 to $\geq$ 17 g/m^3. The maximum of $\overline{n}_{O3}$ was 2000 - 2500 ppm under condition A, 500 - 1000 ppm under condition B and 150 - 400 ppm under condition C.

3.4 Discussion

The bacterial endospores of *Geobacillus stearothermophilus* are thermophile microorganisms that preferably proliferate at high temperatures above $\sim$ 55 °C. Regard-

ing the low heat dissipation at the SMD electrode and the low temperature increase at the sample position, the inactivation of the endospores by heat can be excluded. The measurement of the UV radiation power in the UVC range showed that the UV dose from the SMD plasma was several orders of magnitude below the lethal doses for microorganisms. The chemical species from the SMD plasma were transported onto the sample surface mainly by diffusion. The diffusive transport is described by the diffusion equation of an one-dimensional system

$$\frac{\partial n}{\partial t} = D\frac{\partial^2 n}{\partial x^2} \quad , \tag{3.1}$$

where n is the concentration of the gas particles, D the diffusion coefficient, t time and x the distance. With the typical diffusion coefficients of gases of ~ 0.1 cm^2/s at the atmospheric pressure, the estimated time required for the diffusive transport length of 10 mm was 1 - 10 seconds [257, 258]. Thus, the contribution of the short-lifetime reactive species from the SMD plasma to the sporicidal effect is ruled out. Consequently, it was assumed that the long-lifetime reactive species were primarily responsible for the inactivation of the endospores of *G. stearothermophilus* by the SMD plasma exposure. The single-phase reduction of the endospores in the survival curves suggests that there was only one main mechanism involved in the inactivation process under the investigated conditions.

Ozone is one of the long-lifetime reactive species that can be produced by the SMD plasma in large amounts. As concluded in the previous chapter and demonstrated by Shimizu et al. [165], ozone was strongly correlated with the bacterial reduction by the SMD plasma exposure. The correlation of the ozone concentration with the inactivation efficacy on the endospores of *G. stearothermophilus* after the SMD plasma exposure was investigated in the present study. Under each of the three humidity conditions, the highest ozone concentrations were detected in the power consumption range of 0.5 - 1.5 W, where the reduction of the endospores was small below 0.5 log

under condition A and B and below 1 under condition C. The highest ozone concentrations of up to 2500 ppm was measured under condition A, but the spore reduction remained low and did not exceed 1 log at any power consumption. Here, the sporicidal efficacy remained almost constant although there was a large difference in the averaged ozone concentration $\overline{n}_{O3}$ as the power consumption was changed from 0.5 to 14 W. $\overline{n}_{O3}$ decreased significantly by nearly one order of magnitude as the humidity was increased from $\sim$ 5.5 g/m^3 under condition A to $\geq$ 17 g/m^3 under condition C, whereas the overall sporicidal efficacy increased from below 0.5 log to above 3 log. The maximum spore reduction under condition B was found at the power consumption of 5.0 W, where the ozone concentration dropped to zero after $\sim$ 60 seconds. Under condition C, the spore reduction increased monotonically with increasing power consumption, whereas $\overline{n}_{O3}$ decreased monotonically with at power consumptions higher than 0.5 W. In total, no clear correlation was found between the concentration of ozone produced by the SMD plasma and the reduction of endospores of *G. stearothermophilus*.

Hähnel et al. [259] exposed the endospores of *Bacillus atrophaeus* to a DBD plasma with the relative humidity in the environment varied between 0 and 70%. They reported that air humidity was required for the inactivation of the endospores and the sporicidal efficacy increased monotonically with increasing humidity. After ruling out the contribution of UV and heat, they suggested OH• radicals as the main sporicidal agent. Referring to these observations, the influence of the humidity on the sporicidal efficacy was investigated in this study. It appears that humidity was essential for the inactivation of the endospores of *G. stearothermophilus* under the investigated conditions. Very small reduction of the endospores was observed at the comparably low humidity of $\sim$ 5.5 g/m^3 under condition A. The sporicidal efficacy increased at the moderate humidity of $\sim$ 10 g/m^3 under condition B and the highest reduction of up to $\geq$ 3 log was obtained at the increased humidity of $\geq$ 17 g/m^3. Water molecules can

be dissociated by electrons and produce OH• radicals according to the reaction [190]

$$e^- + H_2O \longrightarrow OH\bullet + H + e^- . \quad \text{(R3)}$$

Alternatively, H atoms and hydroperoxyl radicals ($HO_2\bullet$) can be produced from reaction cascades involving water molecules [180, 189, 190]. Even though OH• radicals, H atoms and $HO_2\bullet$ radicals are short-lifetime reactive species, their contribution to the inactivation of the endospores must be taken into account especially at high humidity, because they can be produced by the reactions of the long-lifetime reactive species (e.g. ozone) with the water molecules in the vicinity of the spore sample surface. Moreover, long-lifetime chemical species, especially H_2O_2, can be produced from reactions involving water molecules and play a role in the inactivation of the bacterial endospores. Reactive nitrogen species such as NO_2, N_2O_5 and HNO_3 can also contribute to the sporicidal effect as suggested by Schnabel et al. [260].

Water condensation was observed in the confined volume between the SMD plasma electrode and the spore sample under condition C when the applied power consumption exceeded 1.0 W. The reactive species from the SMD plasma can react with or dissolve in the condensed water. The formed solution on the sample surface, containing a variety of reactive species, is termed plasma activated water (PAW) [261, 262]. The short-lifetime reactive species associated with water can be formed in PAW as well. If the PAW reached the surface of an endospore sample, the reactive species could have contributed to the inactivation of the endospores.

Jung et al. [263] observed an enhancement of the sporicidal efficacy by $\sim 33\%$ if the endospores of *Bacillus subtilis* were treated with both UV and aqueous ozone. They explained the synergistic effect of UV and ozone by the formation of OH• radicals in the liquid. Additionally, nitric and nitrous acids formed by the SMD plasma can acidify the PAW and promote the sporicidal effect [264, 265]. Regarding the similar sporicidal efficacy at 0.5 - 5.0 W under conditions B and C, the increased endospore

reduction under condition C is possibly the result of the superposition of the endospore reduction under condition B and additional effects from the PAW appeared on the sample surface.

Chapter 4

Influence of Geometry and Time Intervals on SMD Plasma Chemistry

4.1 Ozone Generation by Microdischarges

In the chapters 2 and 3, the dynamic behavior of ozone generation by the SMD was demonstrated. The generation of ozone by SMD involves a third-body reaction (R1), preceded by the dissociation reaction of O_2 molecules by electrons (R2) as described in 2.2.2. The SMD plasma comprises a large number of micro-discharges between the surface of the mesh electrode and that of the dielectric. A single micro-discharge is suggested to have a long cylindrical shape with a widened end at the cathode. The description of the formation mechanism and the relevant properties of the micro-discharges are summarized in 1.8. Due to the accumulation of charge at the surface of the counter electrode by the micro-discharge, there are a spatial gap between the neighboring micro-discharges and a time gap between two micro-discharges occurring at the same location.

In order to describe the relation between the geometry for the plasma production and the plasma chemistry, a simple model was developed. The circular holes in the perforated plate which was used as mesh electrode, is referred to as "openings" or an "open area" with the inner diameter of d. The spatial variable r represents the distance from the center of an opening. Two assumptions were made: (i) the energy and electron densities are uniform in a single micro-discharge. (ii) the micro-discharges have a ideal cylindrical shape, i.e. the length and the diameter of the micro-discharges are constant. The total power consumption is assumed to be proportional to the number of the micro-discharges, since the radial density $E_i(r) = \int E_i(\theta, r)\mathrm{d}\theta$ for both electron and energy is constant for $(\frac{d}{2} - l) \leq r \leq \frac{d}{2}$. l is the length of a micro-discharge and has a positive correlation with the applied voltage. The number of the micro-discharges can be calculated by the division of the circumference of the opening, πd, by the mean distance between the neighbored micro-discharges a. Assuming that a is constant for

different d, the energy and electron density should be proportional to πd as long as $d \geq l$, if the field strength, i.e. the applied voltage is the same. The concentration of ozone is strongly dependent on the electron density in the plasma. With the assumptions made here, the ozone concentration should be controllable by varying geometric parameters, e.g. the diameter of the mesh electrode's opening.

The time scales which are relevant for the SMD plasma are $\sim$ 1 ms and $\sim$ 100 ns from the plasma frequency for electrons and for ions, respectively, the characteristic diffusion time $\tau_{diff} \sim 10s$ and the lifetime of a micro-discharge $\tau_{MD} \sim 10$ ns. In the present study, the possibility to control the plasma chemistry by varying the time interval for plasma generation was investigated. For this purpose, the SMD plasma was generated applying pulsed input power with the pulse width varied in a wide range over 4 orders of magnitude.

Additionally, the dynamics of the concentration of ozone and ozone quenching species was investigated by generating the SMD plasma in two sequenced phases applying different input powers. The results should give more detailed information about the plasma chemistry of SMD.

4.2 Experimental Setup

4.2.1 SMD Plasma Generation

The SMD plasma generator comprised a ceramic plate as dielectric, a perforated stainless plate as mesh electrode and a circular aluminum sheet as planar electrode. The dielectric was square-shaped with the side length of 100 mm. The planar electrode was circular-shaped with the diameter of 30 mm. The thickness of the dielectric and that of the planar electrode was 0.75 mm and less than 0.1 mm, respectively. Perforated stainless steel plates with different measures were used as mesh electrode as

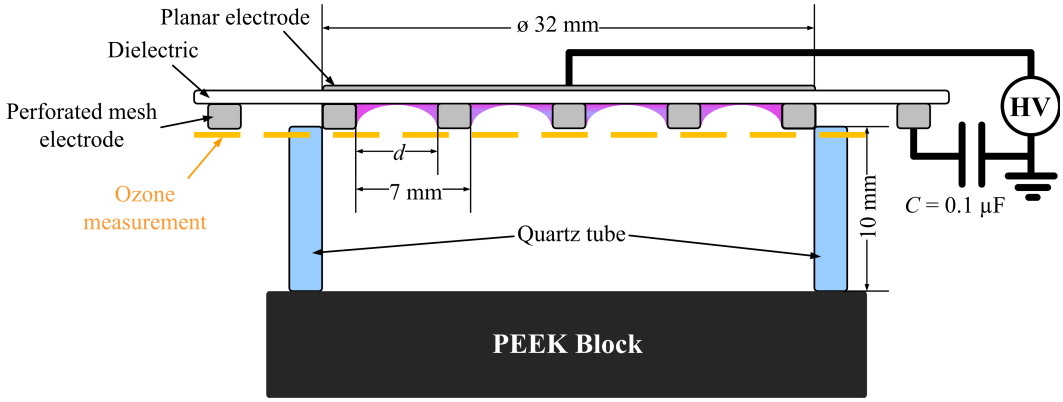

Figure 4.1 Schematic view of the SMD electrode setup with the electric connections and the ozone measurement layer.

will be described later. The power supply comprised a function generator (33220A, Agilent Technologies, Santa Clara, CA, USA) and an amplifier (PM4015, TREK Inc., Lockport, NY, USA). The input voltage, the electric current and the voltage drop across the capacitor were monitored using an oscilloscope (7000B Series, Agilent Techonologies). An additional capacitor was connected in series between the mesh electrode and the ground for the measurement of the power consumption via the Lissajous-figure method as mentioned in chapter 2.

A quartz tube with an inner diameter of 32 mm and a height of 10 mm was placed on the mesh electrode side matching the position of the circular planar electrode. The absorption spectroscopy for the measurement of ozone was performed near the surface of the SMD plasma generation. The beam of light from the light source (Avalight-CAL, Avantes BV, Apeldoorn, Netherlands) passed through the enclosed volume parallel to the SMD plasma electrode at a distance of less than 1 mm from the electrode surface. The absorption spectra were determined and displayed by a spectrometer (AvaSpec-2048, Avantes BV). A sketch of the experimental setup including the electric connections and the position of the light beam for the absorption spectroscopy is shown in Figure 4.1.

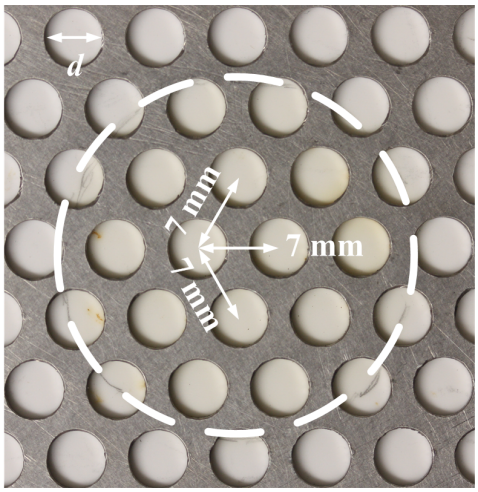

Figure 4.2 Front view of the mesh electrode made of a stainless steel perforated plate. The circular openings were hexagonally arranged with a constant lattice spacing of 7.0 mm. The hole diameter d was variable with 2.5, 3.5 and 5.0 mm.

4.2.2 Variation of the Geometry

The geometry for the SMD plasma generation was changed by interchanging three different perforated plates each with a hole diameter of 2.5, 3.5 or 5.0 mm. In all three perforated plates, the openings were hexagonally arranged with a constant lattice spacing of 7.0 mm. The geometry of the mesh electrode is visualized in Figure 4.2, where d indicates the variable hole diameter. Continuous sinusoidal waveform was applied at the voltages of 7 and 10 kVpp. The frequency was varied between 0.1 and 5.0 kHz. The resulting power consumption was between 0.1 and 7.5 W. Table 4.1 summarizes the mesh size, the ratio of the open area to the powered area and the typical coverage of the open area by the SMD plasma. From the photographs of the SMD plasma, the estimated length of the micro-discharges was 1.8 - 2.0 mm at the applied voltages of 7.0 and 10.0 kV_{pp}.

Table 4.1 Mesh sizes, the ratio of the open area to the power area and the coverage of the open area by the plasma. The plasma coverage was estimated by evaluating photographs.

Mesh	Hole diameter	Area ratio	Plasma coverage
M25	**2.5 mm**	0.12	$\geq$ 100%
M35	**3.5 mm**	0.23	$\sim$ 100%
M50	**5.0 mm**	0.47	$\sim$ 60 - 70 %

4.2.3 Variation of the Time Interval

To investigate the influence of the time interval on the SMD plasma chemistry, a sinusoidal waveform was applied in pulses using the so-called burst mode of the function generator. Here, only the perforated plate with 5 mm hole diameter was used as mesh electrode. The interval between the pulses was controlled by setting the burst period T_B, which was defined as the reciprocal of the pulse frequency f_P. The width of a single pulse was controlled by setting the number of cycles in one pulse N_C. The input frequency f_0 was kept fixed at 10.0 kHz and the applied voltage at 7 kV_{pp}. Based on these parameters, the duty cycle D_C was calculated

$$D_C = \frac{N_C}{T_B f_0} \tag{4.1}$$

and was given in percents (%). Depending on T_B, N_C was varied to obtain the required duty cycle D_C. T_B was varied in a wide range over 4 orders of magnitude from 1 ms to 1000 ms (1 s), resulting in 1 kHz, 100 Hz, 10 Hz and 1 Hz in pulse frequency f_P. D_C was changed betweeen 10% and 50%. Table 4.2 shows the required N_C for the given combinations of T_B and D_C at fixed f_0 of 10 kHz.

Figure 4.3 illustrates the input waveform with the both constant (at 1 ms) and variable T_B and the corresponding diagram for the power consumption with the duty cycles of (a) 10%, (b) 20% and (c) 50%. The input frequency f_0 was fixed at 10 kHz. The

Table 4.2 Number of cycles N_C at $f_0 = 10$ kHz for the given combinations of pulse frequency f_P (burst period T_B) and duty cycle D_C.

T_B	f_P	10%	20%	30%	40%	50%
1 ms	**1 kHz**	1	2	3	4	5
10 ms	**100 Hz**	10	20	30	40	50
100 ms	**10 Hz**	100	200	300	400	500
1 s	**1 Hz**	1000	2000	3000	4000	5000

power consumption within a pulse was constant and exactly as high as the continuous power consumption at the same input frequency (e.g. P_{10kHz} at 10 kHz). On a larger time scale t $\gg T_B$, e.g. of the measurement duration of $\sim 10^2$ s, the time-average power consumption equaled the continuous power consumption at a reduced frequency (effective frequency, $f_{\text{eff}} < f_0$) depending on the duty cycle.

4.2.4 Two-Phase Ignition of the Plasma

For a detailed investigation of the ozone quenching mechanisms, the SMD plasma was ignited applying 7.0 kV_{pp} at 500 Hz, switched off after 90 s and ignited again 10 s later (at t = 100 s) applying the same high voltage at a different frequency, the final frequency f_f. The perforated plate with the hole diameter of 5 mm was used as mesh electrode. f_f was varied between 100 Hz, 500 Hz, 1.0 kHz, 3.0 kHz and 10.0 kHz. It is known from the previous experiments that the SMD was operated in the ozone rich mode until 1.0 kHz and ozone depletion mode at 3 kHz and 10 kHz. Additionally, the plasma was switched off and not ignited again to measure the leakage behavior of the ozone concentration.

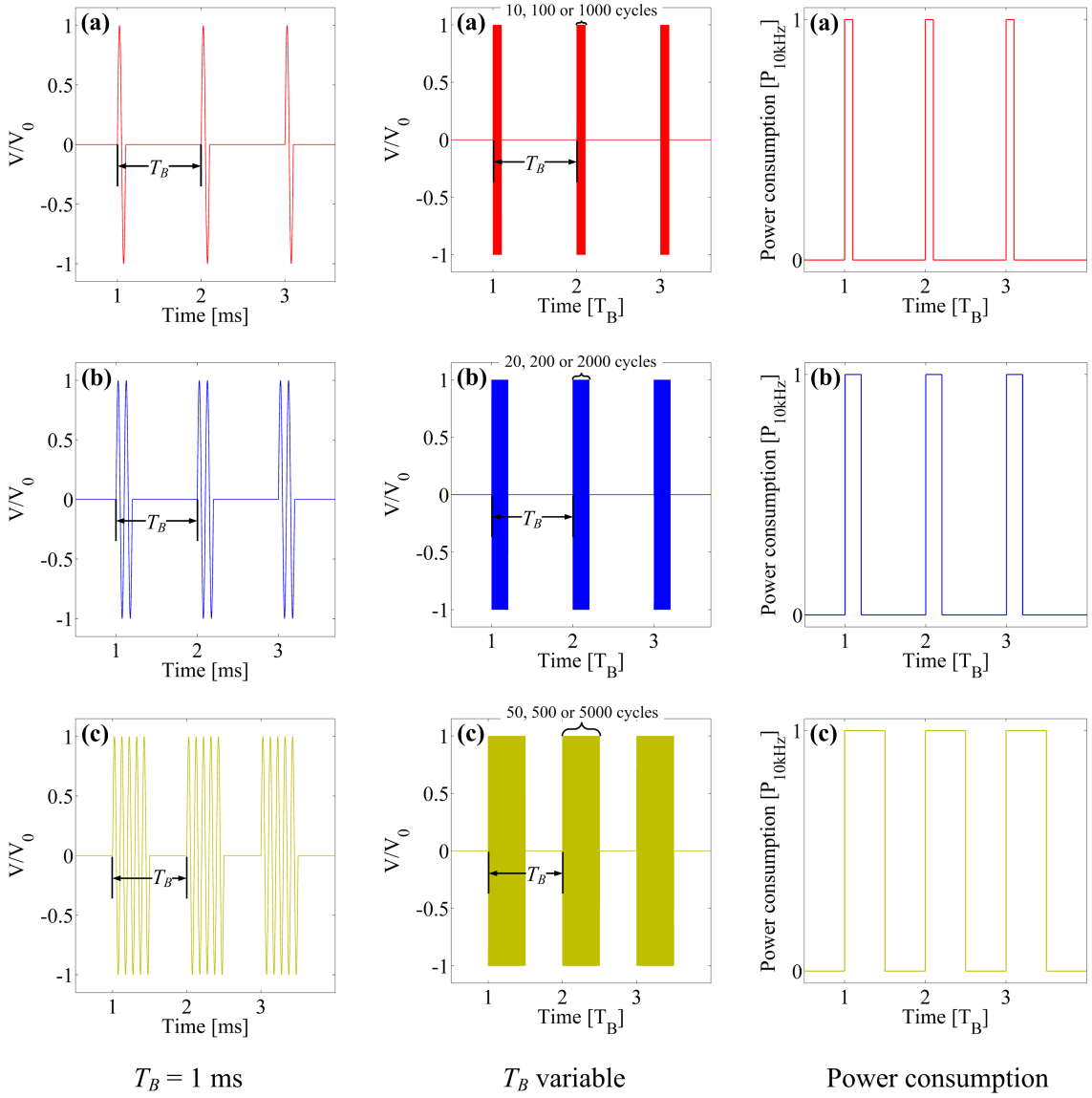

Figure 4.3 Visualization of the burst mode with f_0 = 10 kHz. The input waveform on the timescale of the burst period T_B with T_B = 1 ms and T_B variable. The power consumption on the timescale of T_B. (a) D_C = 10%, (b) D_C = 20% and (c) D_C = 50%.

4.3 Results

4.3.1 Variation of the Geometry

From here, the different perforated plates are on referred to as M25 (mesh electrode with the hole diameter of 2.5 mm), M35 (3.5 mm) and M50 (5.0 mm). Figure 4.4 shows the time evolutions of the ozone concentration n_{O3} at two different voltages of 7 kVpp (a1 - a3) and 10 kVpp (b1 - b3) using M25 (a1, b1), M35 (a2, b2) and M50 (a3, b3). In order to obtain constant power consumptions for different meshes, the applied frequency was adjusted with the voltage fixed at 7 kVpp or 10 kVpp. Comparably little ozone concentrations with maximum concentrations below 500 ppm were measured at both voltages using M25. Similar behaviors were observed using M35 and M50 for both voltages, with a slight tendency of a faster ozone depletion using M35. At the lowest applied power consumptions of 0.5 W (for 7 kV_{pp}) and 0.1 W (for 10 kV_{pp}), n_{O3} increased monotonically with time. At higher power consumptions, n_{O3} increased during an initial phase, reached a maximum and decreased. n_{O3} dropped down to zero within the measurement duration of 120 s if the power consumption exceeded $\sim$ 4.5 W depending on the conditions. The duration of the initial increasing phase and the maximum of n_{O3} decreased with increasing power consumption. Two different ozone generation modes, namely the saturation mode and the depletion mode, were found at both voltages with the transition taking place at $\sim$ 2 W using M25 and at 3.5 - 4.5 W using M35 and M50. In total, the shapes of the time evolution curves of n_{O3} were similar using M35 and M50 at both applied voltages 7 and 10 kVpp

The time-dependent ozone concentration was obtained by averaging over the measurement duration. The so calculated averaged ozone concentration $\overline{n}_{O3}$ is shown in Figure 4.5. $\overline{n}_{O3}$ was slightly higher at 7 kV_{pp} than at 10 kV_{pp} using all three perforated plates. Using M35 and M50, $\overline{n}_{O3}$ increased up to $\sim$ 1400 ppm as the power consumption increased from near zero to 1.5 W and decreased continuously with the

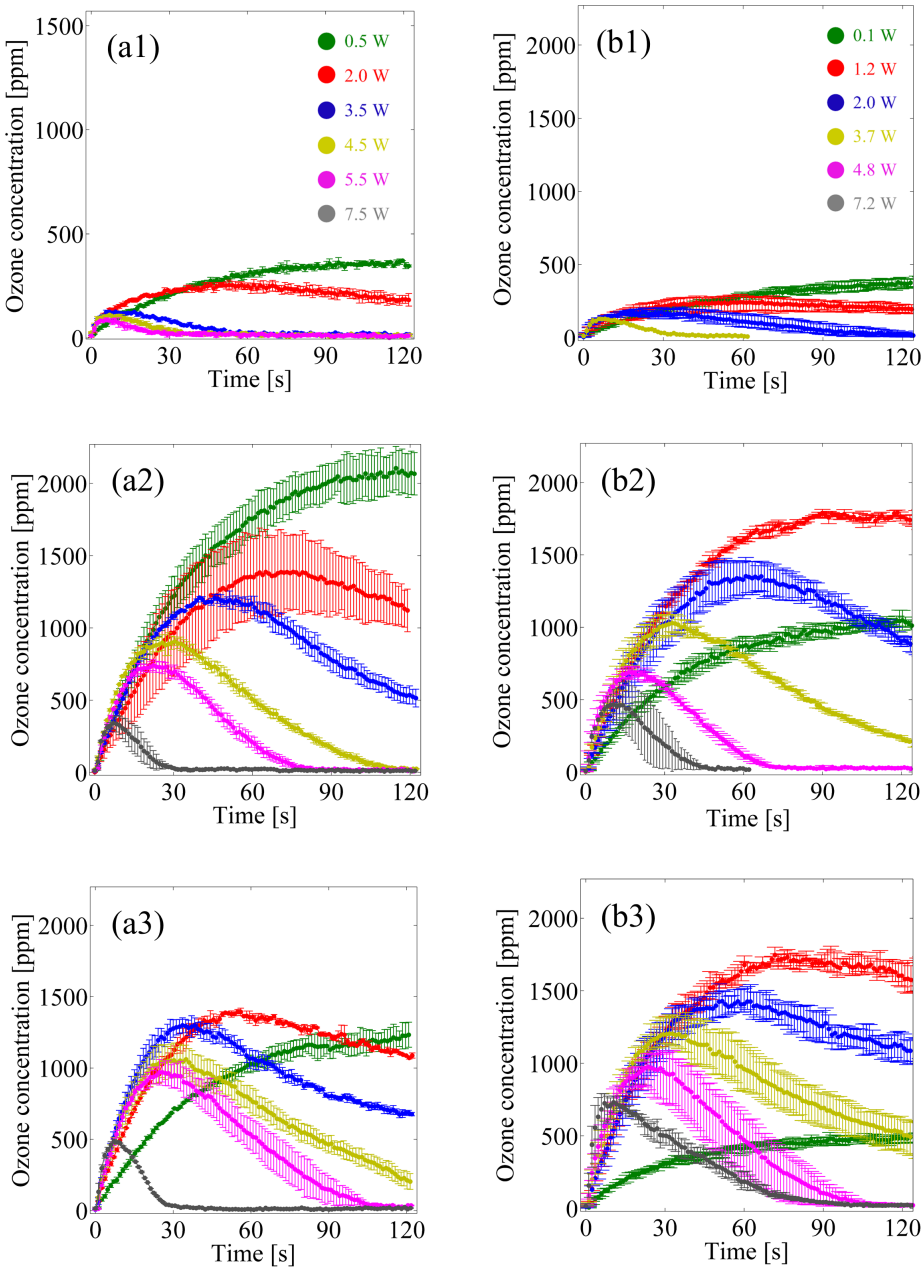

Figure 4.4 Time evolutions of the ozone concentration at different power consumptions using three different perforated plates as mesh electrode. (a1) - (a3) voltage fixed at 7 kVpp, (b1) - (b3) 10 kVpp. (a1), (b1) 2.5 mm hole diameter, (a2), (b2) 3.5 mm hole diameter, (a3), (b3) 5.0 mm hole diameter. (a1), (a2) and (a3) share the legend from (a1), and (b1), (b2) and (b3) share the legend from (b1).

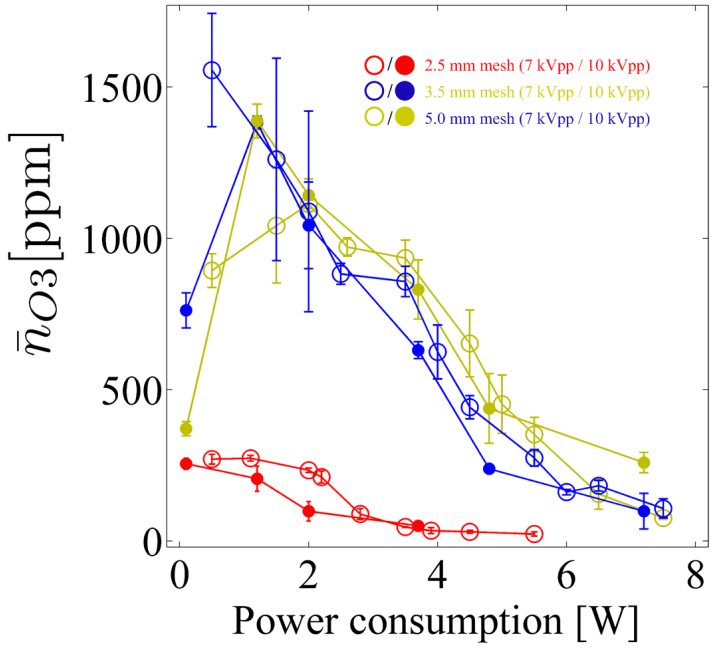

Figure 4.5 Averaged ozone concentrations at two different applied voltages 7 kV_{pp} and 10 kV_{pp} using three different hole diameters 2.5 mm, 3.5 mm and 5.0 mm.

power consumption increased further. $\overline{n}_{O3}$ using M25 was $\sim$ 250 ppm by a factor of 4 - 6 smaller than using the meshes with a bigger hole diameter and decreased monotonically with increasing power consumption.

The production rate of ozone P_{O3} is defined by the slope of the time evolution curve immediately after the plasma ignition (t = 0), as following

$$P_{O3} = \left.\frac{\mathrm{d}n_{O3}}{\mathrm{d}t}\right|_{t=0} . \tag{4.2}$$

Figure 4.6 shows P_{O3} from the SMD plasma using different meshes at different power consumptions. The difference between the applied voltages 7 kV_{pp} and 10 kV_{pp} was negligibly small and showed that P_{O3} depends only on the power consumption and not on the applied voltage or frequency individually. Using M25, P_{O3} increased from

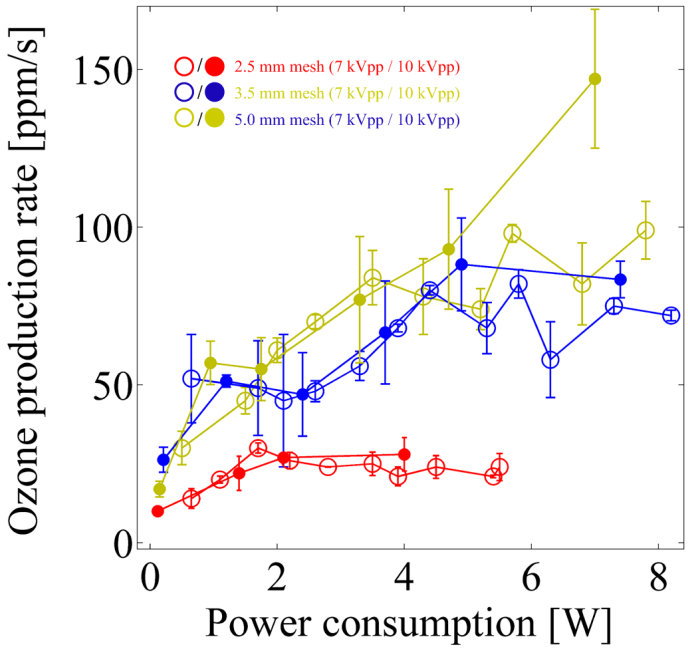

Figure 4.6 Production rates of ozone from the SMD plasma using different meshes (with 2.5, 3.5 and 5.0 mm hole diameter) at varied power consumption with applied voltages 7 and 10 kV_{pp}.

$\sim$ 10 ppm/s to $\sim$ 25 ppm/s as the power consumption was increased from near zero to 2 W, and saturated at $\sim$ 25 ppm/s as the power consumption was further increased. Using M35 and M50, P_{O3} increased monotonically with increasing power consumption. Higher P_{O3} were observed using M50 than using M35, if the power consumption exceeded 2 W. The maximum P_{O3} obtained in this study was 125 $\pm$ 20 ppm/s using M50 and 80 $\pm$ 10 ppm/s using M35.

4.3.2 Variation of the Time Interval

The time evolutions of ozone at different pulse frequencies f_P with varied duty cycle D_C are shown in Figure 4.7. With D_C at 10%, the time-dependent ozone concen-

tration n_{O3} increased during the first $\sim$ 60 s after the SMD plasma ignition and saturated. The saturation level varied from $\sim$ 1000 to $\sim$ 2000 depending on f_P. The highest and the lowest concentrations were found with f_P at 100 Hz and at 1 Hz, respectively. With D_C at 20% and 30%, n_{O3} increased in the first 40 - 50 s after the ignition and decreased thereafter. n_{O3} appeared to approach a saturation value. With D_C of 40% and 50%, n_{O3} increased in the first $\leq$ 25 s, then declined to zero. No transition between the ozone generation modes, was found when D_C was kept constant and f_P was varied. The saturation and the overall concentrations of ozone were highest with f_P at 100 Hz and 10 Hz. The lowest ozone concentrations were measured with f_P at 1 Hz. The ozone concentrations with f_P of 100 Hz and 10 Hz on the one hand and with f_P of 1 kHz and 1 Hz on the other hand increasingly overlapped as D_C was raised from 10% to 50%.

The time-dependent ozone concentration was averaged over the measurement duration of 2 minutes. Figure 4.8(a) and (b) show the averaged ozone concentrations $\overline{n}_{O3}$ plotted against f_P (a) and against D_C (b), respectively. The maximum $\overline{n}_{O3}$ appeared with f_P between 10 Hz and 100 Hz at any of the applied D_C of 10%, 20%, 30%, 40% and 50%. $\overline{n}_{O3}$ declined at 1 Hz and 1 kHz of f_P.

$\overline{n}_{O3}$ decreased monotonically with increasing D_C at any of the applied f_P. At 10%, 20% and 30%, the highest and lowest $\overline{n}_{O3}$ were observed with f_P at 100 Hz and at 1 Hz, respectively. At 40% and 50%, similar $\overline{n}_{O3}$ were observed with f_P at 10 Hz and 100 Hz as well as at 1 Hz and 1 kHz.

The production rate of ozone P_{O3} by the SMD plasma was calculated by determining the slope of time-dependent n_{O3} immediately after the plasma ignition. Figure 4.9 shows P_{O3} at different f_P and D_C. Nearly constant P_{O3} was observed with f_P at 10 Hz to 1 kHz. Clearly lower P_{O3} were measured at 1 Hz. Generally, P_{O3} increased slightly with increasing D_C.

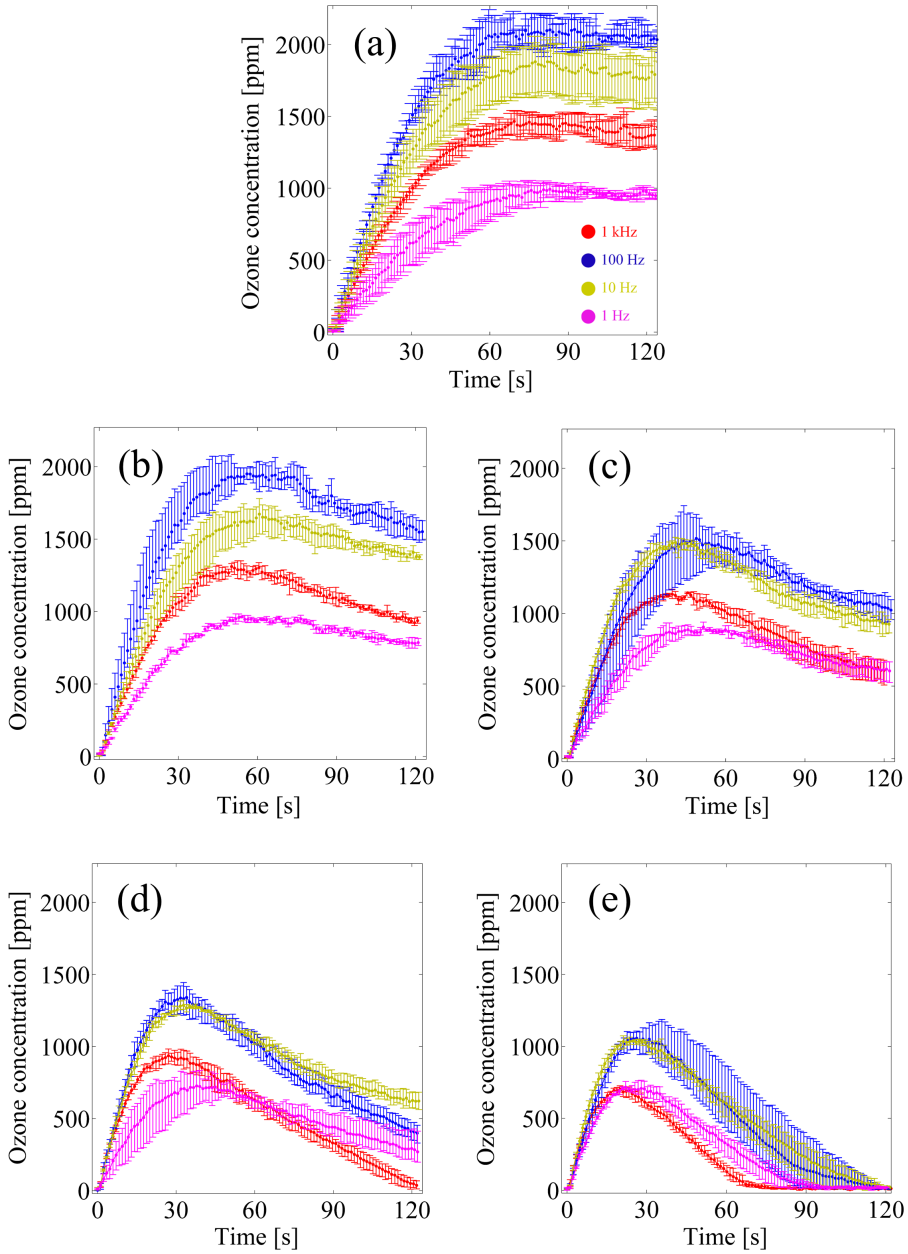

Figure 4.7 Time evolutions of the ozone concentration from the SMD plasma applying pulsed sinusoidal waveform with varied pulse frequency f_P. Applied input frequency $f_0 = 10$ kHz and applied voltage $V = 7$ kV_{pp}. (a) duty cycle $D_C = 10\%$, (b) $D_C = 20\%$, (c) $D_C = 30\%$, (d) $D_C = 40\%$ and (e) $D_C = 50\%$. Legend in (a) applies for all subplots (a) - (e).

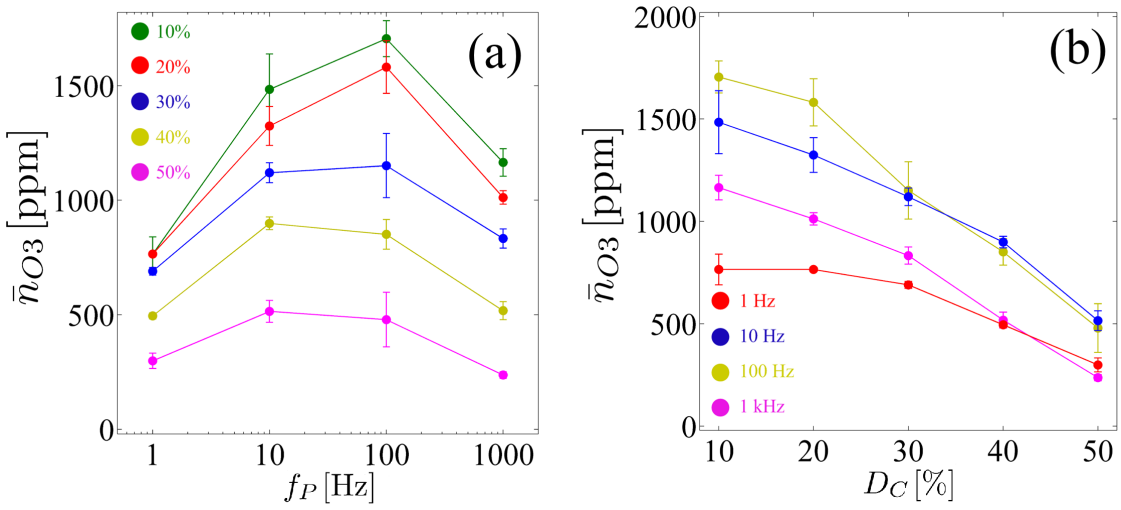

Figure 4.8 Ozone concentrations averaged over the measurement duration of 2 minutes with the burst mode applied. (a) plotted against the pulse frequency f_P, (b) plotted against the duty cycle D_C.

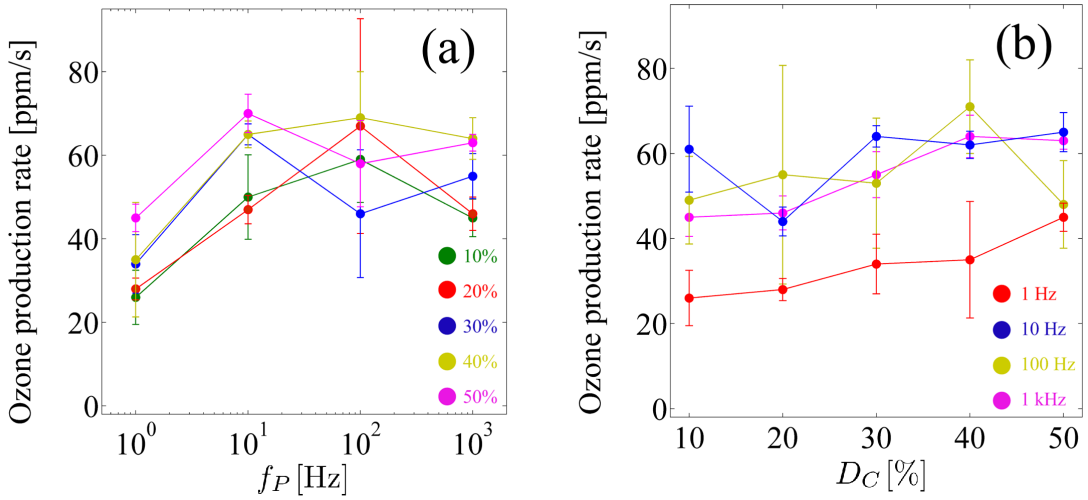

Figure 4.9 Production rates of ozone from the SMD plasma with the burst mode applied. (a) plotted against the pulse frequency f_P, (b) plotted against the duty cycle D_C.

4.3.3 Two-Phase Ignition of the Plasma

The time-dependent ozone concentrations n_{O3} are shown in Figure 4.10. The vertical bars at t = 90 s and 100 s indicate the time points where the SMD plasma with the initial frequency f_0 was switched off and re-ignited with the final frequency f_f, respectively. The dots indicate n_{O3}, when the SMD plasma was ignited and sustained with f_0 for 90 s, then switched off and re-ignited with f_f (except for Figure 4.10(a), where the plasma was not ignited for the second time). The thin solid lines represent n_{O3}, when the SMD plasma was generated continuously with the corresponding f_f. Figure 4.10(a) shows n_{O3}, when the SMD plasma was switched off and not ignited again after t = 90 s. The complete leakage of ozone (n_{O3} = 0) was reached after $\sim$ 180 s. The leakage of ozone was fitted by an exponential curve with

$$n_{O3}(t) \;=\; n_{O3}(t = 90s)\exp\left(-\frac{t-90s}{\tau}\right).$$

where $\tau \approx 34$ s is the characteristic leakage duration. The experiments with the second SMD plasma ignition showed an exponential decrease of n_{O3} during 10 s of the plasma-off duration according to the leakage. With f_f at 100 Hz, n_{O3} decreased after the re-ignition and saturated at the typical saturation concentration of ozone for 100 Hz, as shown in Figure 4.10(b). The re-ignition of the SMD plasma with $f_f = f_0$ = 500 Hz resulted in a increase of n_{O3} until the ozone loss due to the leakage during the plasma-off time (90 - 100 s) was compensated. After $\sim$ 30 s, the typical saturation level for 500 Hz was reached, as shown in Figure 4.10(c). The maximum n_{O3} from the continuous SMD plasma operation was observed at 1 kHz under the investigated conditions. As shown in Figure 4.10(d), the re-ignition with f_f at 1 kHz led to an increase of n_{O3} to the typical level for 1 kHz. Here, the re-ignition curve followed exactly the decreasing trend (and no saturation behavior) of the continuous n_{O3} curve at 1 kHz. In the ozone depletion mode at 3 and 10 kHz, n_{O3} decreased linearly and dropped to zero. The ozone depletion speed increased with increasing frequency (i.e. power consumption).

While the slope of the linear decrease was nearly the same at 3 kHz, the depletion speed was much higher after the re-ignition with 10 kHz than from the continuous SMD operation at the same frequency.

No increase of the ozone concentration was observed when the initial frequency f_0 was set to 10 kHz and any frequency between 0.1 and 10 kHz was chosen as f_f (data not shown). As the SMD plasma was re-ignited with f_f, the ozone concentration remained at 0. After $\sim$ 180 s of plasma generation, ozone was detected again. The initial increase of the ozone concentration was not as fast as with no pre-ignition, but exponential until the typical concentration was reached.

4.4 Discussion

Variation of the Geometry

With increasing power consumption until $\sim$ 1.5 W, the ozone production rate P_{O3} increased monotonically while the averaged ozone concentration increased in a saturation mode and decreased in a depletion mode. The decrease of ozone in the ozone depletion mode was much faster than the exponential decrease by leakage. It was therefore assumed that ozone was quenched by other reactive species produced by the SMD plasma, e.g. NO_2. The transition from the ozone saturation mode to the ozone depletion mode occurred if the production rate of the ozone quenching species surpassed P_{O3}.

Using M25, both the production rate and the averaged concentration of ozone from the SMD plasma was significantly below those using M35 and M50 at the same power consumption. As described in chapter 1, the surface micro-discharges are formed along the boundary edge between a single opening of the mesh electrode and the surface of the dielectric. With a hole diameter of 2.5 mm, the entire open area in the mesh

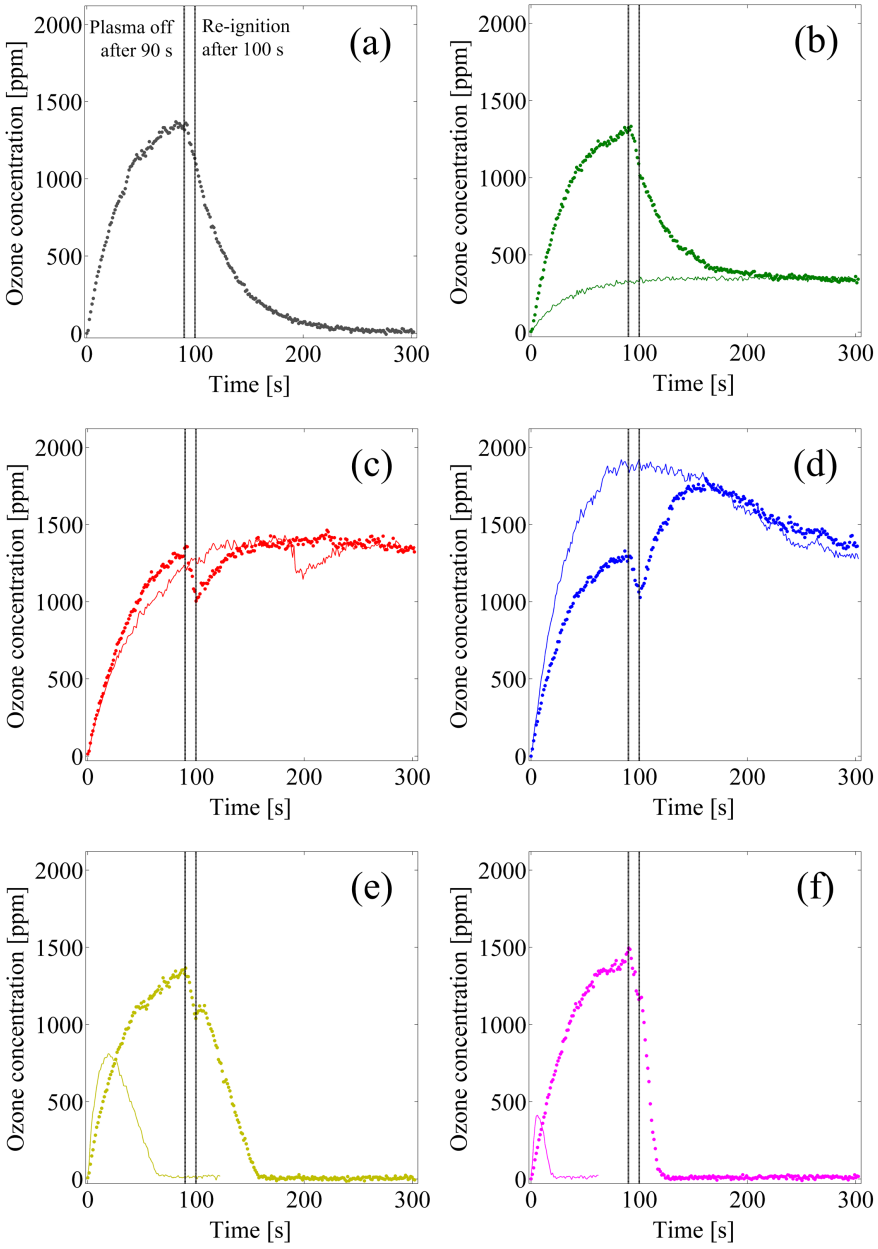

Figure 4.10 Time evolutions of the ozone concentration from the SMD plasma with two-phased ignition. The SMD plasma was ignited at $t = 0$ with an initial frequency f_0 of 500 Hz. The plasma was switched off at $t = 90$ s and re-ignited at $t = 100$ s with a second frequency f_f. Solid dots mark the two-phased ignition. Thin lines mark the respective ozone concentration with no second ignition and $f_0 = f_f$. (a) no re-ignition, (b) $f_f = 100$ Hz, (c) $f_f = 500$ Hz, (d) $f_f = 1$ kHz, (e) $f_f = 3$ kHz and (f) $f_f = 10$ kHz.

was covered by the microdischarges. With the constant lattice spacing of the mesh electrode for different meshes, the available area for the plasma production using M25 was smaller than using M35 and M50 at a fixed power consumption, as shown in table 4.1. When M25 was used, the production of ozone was already suppressed due to the limitation of the volume for the plasma generation. Since the ozone concentration was similar using M35 and M50, it was assumed that a hole diameter of 3.5 mm was sufficient for a homogeneous distribution of the SMD in a single opening of the mesh electrode. From the photographs of the discharge, the estimated length of the microdischarges was 1.8 to 2.0 mm at the applied voltage of 7.0 and 10.0 kV_{pp} and matched approximately the radius of the M35 mesh.

Furthermore, it was possible that the production and recombination rates of ozone and the ozone quenching species were affected by the hole diameter. In the ozone depletion mode, the time required for the complete depletion of ozone with M25 was shorter than with M35 and M50 at the same power consumption. This suggests that the ratio of the production rate of the ozone quenching species to P_{O3} was higher using M25 than using M35 or M50. In addition, it is assumed that the local heat dissipation is increased using M25, because the power is consumed in a smaller area, and possibly promote the thermal dissociation of ozone.

Even though partly large differences in the time evolution, averaged concentration and production rate of ozone were observed, no clear shift of the transition between the different ozone generation modes was found as the geometry for the SMD plasma generation was varied.

Variation of the Time Interval

The time evolution and the averaged concentration of ozone were strongly affected by the pulse frequency f_P. The averaged concentration decreased in the following order: 100 Hz > 10 Hz > 1 kHz > 1 Hz. A possible explanation for the low concentrations of ozone at 1 Hz is given by the comparably long plasma-off time of 500 - 900

ms. It is suggested that the recombination processes of the short-lifetime species were promoted by the low pulse frequency of 1 Hz, which greatly reduced the availability of the short-lifetime reactive species e.g. for the formation of ozone, which requires the atomic oxygen. Consequently, it was expected that the ozone concentration increased with decreasing plasma-off time by increasing f_P, as it was the case in this study up to 100 Hz.

At the pulse frequency of 1 kHz, however, the ozone concentration decreased. This observation suggested that there were more than one mechanism involved in the production and quenching of ozone, and that each of these mechanisms were differently pronounced depending on the pulse frequency. It is possible that the production rate and recombination rate of ozone and the ozone quenching reactive species changed at the high pulse frequency. One possible explanation is that the formation of short-lifetime species was suppressed by the short plasma ignition time of 1 ms, which was the pulse duration corresponding to the pulse frequency of 1 kHz. This could have negatively influenced the production of ozone. Another possible explanation is given by the non-ideal waveform generated by the power supply. The function generator would have made pulses with no sharp edges at the boundaries thus that power was lost with every single pulse. At the pulse frequency of 1 kHz, the number of pulses could have been high enough thus that the accumulated power loss became significant.

In spite of partly large differences in the time evolution, the transition between the different ozone generation modes did not change when the pulse duration was varied over 4 orders of magnitude. These results indicate that the chemistry from the SMD plasma is mainly governed by the power input.

Two-Phased Ignition

The results with f_0 at 500 Hz showed that the saturation concentration and the shape of the time evolution curves of ozone were characteristic for the applied fre-

quency/power consumption and were not affected by the ozone concentration in the gas composition for the SMD plasma.

With f_0 at 10 kHz, the ozone concentration remained at zero after the second plasma ignition regardless of f_F. This result indicates that the remaining products from the plasma with f_0 at 10 kHz in the confined volume quenched ozone and/or atomic oxygen immediately. The ozone prohibition time of 180 s equaled the duration required for a complete exchange of the gas in the confined volume by leakage. The smooth initial increase of the ozone concentration with the exponential shape after the re-ignition indicated that ozone started to be produced again after the ozone quenching reactive species leaked away. These observations support the idea that the volume was saturated with ozone quenching species that prohibited the ozone production and indicate that the lifetime of ozone quenching species is long on the scale of τ.

The plasma production and the driven chemistry are dependent on several parameters as shown in this chapter. The complex chemistry is still under investigation and requires a comprehensive study including plasma physics, chemistry and fluid mechanics. In this study, the ozone concentration was measured at one single position. It is necessary to measure the flow pattern and the distribution of reactive species, which can be highly non-uniform, in the future studies. Thermal convection can be present in a closed volume since the generation of the SMD gives rise to heat dissipation at the electrode.

Chapter 5

Conclusion

The focus of the study was the optimization and better understanding of the inactivating effect of the SMD plasma treatment on a variety of microorganisms. For this purpose, the microbiocidal efficacy of the SMD plasma on vegetative bacteria and bacterial endospores was investigated with a special focus on the chemistry from the plasma. Furthermore, a variety of parameters was modified and the impact on the ozone chemistry from the SMD plasma was evaluated.

The contribution of UV and heat from the SMD plasma to the microbiocidal effect was ruled out. The inactivation of both Gram-negative *E. coli* and Gram-positive *Enterococcus mundtii* bacteria on agar by the SMD plasma treatment was strongly correlated with the concentration of ozone produced by the plasma. Nitrogen reactive species did not play a role under the investigated conditions. A large difference was found in the reduction of the bacterial endospores of *G. stearothermophilus* after 5 minutes of exposure to the SMD plasma, when the humidity for the plasma generation was varied. The response of the sporicidal efficacy was nonlinear at different humidities and no correlation with the concentration of ozone was found. The ozone concentration showed a dynamic, nonlinear response when the geometry and the time interval of the SMD plasma generation was changed. The results indicate that ozone is quenched mainly by long-lifetime species. The production of the long lifetime species was dependent on time and the input power.

Ozone was found to be crucial for the inactivation of bacteria by the SMD plasma, while the humidity plays the key role in the sporicidal effect. The plasma chemistry driven by the SMD plasma, especially the production of ozone, is mainly controlled by the input power It can be influenced by the variation of the geometry and the time interval of the plasma generation.

More detailed studies are required for a better understanding of the findings. Dry substrates for the bacterial samples instead of agar should be used in order to consolidate the major contribution of ozone to the inactivation of bacteria by the SMD plasma treatment. Additionally, the bacterial samples should be treated by the SMD

plasma in the ozone depletion mode. Since a sort of branching of the plasma chemistry was found at the different humidities, the humidity should be varied in smaller steps. The concentration of water-related reactive species, such as hydrogen peroxide, should be monitored and its correlation with the sporicidal efficacy should also be investigated. For the variation of the ozone concentration, the SMD plasma should be generated in one single open area with a variable inner diameter. The ozone measurement could be performed at different distances from the SMD electrode in order to determine the spatial distribution.

List of Acronyms

a	mean distance between neighboring micro-discharges
APPJ	atmospheric pressure plasma jet
AC	alternating current
$\mathcal{C}$	integration constant
CAP	cold atmospheric plasma
CDBD	cascaded barrier discharge
CFU	colony forming unit
d	hole diameter of the mesh electrode
D	diffusion constant
D_C	duty cycle
DBD	dielectric barrier discharge
DBGD	dielectric barrier grating discharge
DC	direct current
DNA	dioxyribonucleic acid
DPA	dipicolinic acid
DSM	German collection of microorganisms
e	elementary charge
E_{kin}	kinetic energy
E_{pot}	potential energy
EtO	ethylene oxide
f_0	input frequency
f_{Ar}	argon fraction
f_f	final frequency
f_{N2}	nitrogen fraction
f_{O2}	oxygen fraction
f_P	pulse frequency
FE-DBD	floating electrode dielectric barrier discharge

g_z	degeneracy for the z ionization state
h	Planck's constant
HAI	health care-associated infection
HELICS	Hospital in Europe Link for Infection Control through Surveillance
HV	high voltage
I	(measured) light intensity
I_0	transmitted light intensity wihtout plasma
IARC	International Agency for Research on Cancer
ICU	intensive care unit
l	mean length of a micro-discharge
k_B	Boltzmann's constant
m_e	mass of an electron
m_i	mass of an i ion
M25	mesh electrode with a hole diameter of 2.5 mm
M35	mesh electrode with a hole diameter of 3.5 mm
M50	mesh electrode with a hole diameter of 5.0 mm
MRSA	methicillin-resistant *Staphylococcus aureus*
MW	microwave
n	concentration of gas particles
N	particle number density
N_D	plasma parameter
n_e	electron number density
n_i	ion number density
$N_i(\mathbf{r})$	spatial distribution of the number density of particle i
N_C	number of cycles in a single pulse
$n_{O3}, n_{O3}(t)$	time dependent ozone concentration
$\bar{n_{O3}}$	averaged ozone concentration
NIOSH	National Institute for Occupational Safety and Health
OAUGDP	one atmospheric uniform glow discharge plasma
OSHA	Occupational Safety and Health Administration

P_{O3}	production rate of ozone
PAW	plasma activated water
PBS	phosphate buffered saline
PECVD	plasma enhanced chemical vapor diposition
PEF	pulsed electric field
PEEK	polyether ether keptone
PS	photosensitizer
r	radial distance
$\bar{r}$	mean interparticle distance
RF	radio frequency
RNA	ribonucleic acid
RNS	reactive nitrogen species
ROS	reactive oxygen species
r.t.	room temperature
SASP	small acid-soluble protein
SEM	scanning electron microscope
SMD	surface micro-discharge
t	time
T	temperature of the system
T_B	burst period
T_e	electron temperature
T_i	ion temperature
TMZ	temozolomide
TSA	Tryptic soy agar
TWA	time weighted average
UV	ultraviolet
V	voltage
VRE	vancomycin-resistant *Enterococcus*
WHO	World Health Organization
x	distance/length of the path

z	ionization state
Z_i	charge number of i ions
α	degree of ionization
γ	coupling paramter
ϵ_0	vacuum permittivity
θ	polar angle
λ	thermal de Broglie wavelength of an electron
λ_D	Debye length
σ	absorption cross section
τ_{diff}	characteristic diffusion time
τ_{MD}	mean lifetime of a micro-discharge
χ_z	ionization energy for the z ionization state
ω_p	plasma frequency
$\omega_p e$	plasma frequency of electrons
$\omega_p i$	plasma frequency of ions

REFERENCES

[1] H. M. Mott-Smith, "History of 'Plasmas'," *Nature*, vol. 233, p. 219, 1971.

[2] U. Kogelschatz, "Atmospheric-pressure plasma technology," *Plasma Physics and Controlled Fusion*, vol. 46, pp. B63–B75, 2004.

[3] R. M. Klevens, J. R. Edwards, C. L. Richards, T. C. Horan, R. P. Gaynes, D. A. Pollock, and D. M. Cardo, "Estimating Health Care-Associated Infections and Deaths in U.S. Hospitals, 2002," *Public Health Reports*, vol. 122, pp. 160–166, 2007.

[4] S. S. Magill *et al.*, "Multistate Point-Prevalence Survey of Health Care-Associated Infections," *The New England Journal of Meidicine*, vol. 370, pp. 1198–1208, 2014.

[5] C. Suetens, S. Hopkins, J. Kolman, and L. D. Högberg, "Point prevalence survey of healthcare-associated infections and antimicrobial use in European acute care hospitals," tech. rep., European Center for Disease Prevention and Control, Stockholm, 2013.

[6] The Hospital in Europe Link for Infection and Control through Surveillance (HELICS), `http://helics.univ-lyon1.fr/` [Accessed June 2011].

[7] F. Vrijens, F. Hukstaert, S. Devriese, and S. van de Sande, "Hospital-acquired infections in Belgian acute-care hospitals: an estimation of their global impact on mortality, length of stay and healthcare costs," *Epidemiology and Infection*, vol. 140, pp. 126–136, 2012.

[8] M. Kanerva, J. Ollgren, M. J. Virtanen, and O. Lyytikäinen, "Estimating the annual burden of health care-associated infections in Finnish adult acute care hospitals," *American Journal of Infection Control*, vol. 37, no. 3, pp. 227–230, 2009.

[9] R. Plowman, N. Graves, M. A. S. Griffin, J. A. Roberts, A. V. Swan, B. Cookson, and L. Taylor, "The rate and cost of hospital-acquired infections occurring in patients admitted to selected specialities

of a district general hospital in england and the national burden imposed," *Journal of Hospital Infection*, vol. 47, pp. 198–209, 2001.

[10] P. Gastmeier and C. Geffers, "Nosokomiale Infektionen in Deutschland: Wie viele gibt es wirklich?," *Deutsche medizinische Wochenschrift*, vol. 133, pp. 1111–1115, 2008. (*In German*).

[11] A. I. Hidron *et al.*, "Antimicrobial-Resistant Pathogens Associated With Healthcare-Associated Infections: Annual Summary of Data Reported to the National Healthcare Saftey Network at the Centers for Disease Control and Prevention, 2006-2007," *Infection Control and Hospital Epidemiology*, vol. 29, no. 11, pp. 996–1011, 2008.

[12] A. K. Chaudhuri, "Infection control in hospitals: has its quality-enhancing and cost-effective role been appreciated?," *Journal of Hospital Infection*, vol. 25, pp. 1–6, 1993.

[13] R. D. Scott, "The Direct Medical Costs of Healthcare-Associated Infections in U.S. Hospitals and the Benefits of Prevention," 2009. (*On behalf of the Division of Healthcare Quality Promotion; the National Center for Preparedness, Detection, and Control of Infectious Diseases; the Coordinating Center for Infectious Diseases and the Centers for Disease Control and Prevention*).

[14] D. Reed and S. A. Kemmerly, "Infection Control and Prevention: A Review of Hospital-Acquired Infections and the Economic Implications," *The Ochser Journal*, vol. 9, pp. 27–31, 2009.

[15] A. F. Widmer, "Surgical hand hygiene: scrub or rub?," *Journal of Hospital Infection*, vol. 83, no. S1, pp. S35–S39, 2013.

[16] B. N. Doebbeling *et al.*, "Removal of Nosocomial Pathogens from the Contaminated Glove: Implications for Glove Reuse and Handwashing," *Annals of Internal Medicine*, vol. 109, no. 5, pp. 394–398, 1988.

[17] L. A. Mermel, M. McKay, J. Dempsey, and S. Parenteau, "*Pseudomonas* Surgical-Site Infections Linked to a Healthcare Worker With Onychomycosis," *Infection Control and Hospital Epidemiology*, vol. 24, no. 10, pp. 749–752, 2003.

[18] S. Weber *et al.*, "An Outbreak of *Staphylococcus aureus* in a Pediatric Cardiothoracic Surgery Unit," *Infection Control and Hospital Epidemiology*, vol. 23, no. 2, pp. 77–81, 2002.

[19] E. K. Koiwai and H. C. Nahas, "Subacute Bacterial Endocarditis Following Caridac Surgery," *Archives of Surgery*, vol. 73, no. 2, pp. 272–278, 1956.

[20] K. Inweregbu, J. Dave, and A. Pittard, "Nosocomial infections," *Continuing Educations in Anaesthesia. Critical Care and Pain*, vol. 5, no. 1, pp. 14–17, 2005.

[21] World Health Organization, *WHO Guidelines on Hand Hygiene in Health Care*, 2009.

[22] J. M. boyce, S. Kelliher, and N. Vallande, "Skin Irritation and Dryness Associated With Two Hand-Hygiene Regimens: Soap-and-Water Hand Washing Versus Hand Antisepsis With an Alcoholic Hand Gel," *Infection Control and Hospital Epidemiology*, vol. 21, no. 7, pp. 442–448, 2000.

[23] E. Larson *et al.*, "Skin reactions related to hand hygiene and selection of hand hygiene products," *American Journal of Infection Control*, vol. 34, pp. 627–635, 2006.

[24] G. E. Morfill, T. Shimizu, B. Steffes, and H.-U. Schmidt, "Nosocomial infections - a new approach towards preventive medicine using plasmas," *New Journal of Physics*, vol. 11, p. 115019, 2009.

[25] Dortmund Data Bank, "`http://www.ddbst.com/en/EED/PCP/VAP_C174.php`" [Accessed May 2014].

[26] L. J. Joslyn, *Disinfection, Sterilization, and Preservation (5th Edition)*, ch. 36, Sterilization by Heat, pp. 695–728. Philadelphia, USA: Lippincott Williams and Wilkins, 2001.

[27] R. K. Oag, "The Resistance of Bacerial Spores to Dry Heat," *Journal of Pathology and Bacetriology*, vol. 51, pp. 137–141, 1940.

[28] L. J. Joslyn, *Disinfection, Sterilization, and Preservation (5th Edition)*, ch. 16, Gaseous Chemical Sterilization, pp. 337–359. Philadelphia, USA: Lippincott Williams and Wilkins, 2001.

[29] A. Downes and T. P. Blunt, "Researches on the Effect of Light upon Bacteria and other Organisms," *Proceedings of the Royal Society of London; Philosophical Transactions of the Royal Society*, pp. 488–500, January 1st 1877.

[30] W. A. M. Hijnen, E. F. Beerendonk, and G. J. Medema, "Inactivation credit of UV radiation for viruses, bacteria and protozoan (oo)cysts in water: A review," *Water Research*, 2006.

[31] E. R. Blatchley and M. M. Peel, *Disinfection, Sterilization, and Preservation (5th Edition)*, ch. 41, Disinfection by Ultraviolet Irradiation, pp. 823–851. Philadelphia, USA: Lippincott Williams and Wilkins, 2001.

[32] T. Carell and R. Epple, "Repair of UV Light Induced DNA Lesions: A Comparative Study with Model Compounds," *European Journal of Organic Chemistry*, no. 7, pp. 1245–1258, 1998.

[33] J. R. Bolton and K. G. Linden, "Standardization of Methods for Fluence (UV Dose) Determination in Bench-Scale UV Experiments," *Journal of Environmental Engineering*, vol. 129, no. 3, pp. 209–215, 2003.

[34] L. J. rose and H. O'Connell, "UV Light Inactivation of Bacterial Biothreat Agents," *Applied and Environmental Microbiology*, vol. 75, no. 9, pp. 2987–2990, 2009.

[35] J. C. H. Chang *et al.*, "UV Inactivation of Pathogenic and Indicator Microorganisms," *Applied Environmental Microbiology*, vol. 49, no. 6, pp. 1361–1365, 1985.

[36] B. A. Jurkiewicz and G. R. Buettner, "Ultraviolet Light-Induced Free Radical Formation in Skin: An Electron Paramagnetic Resonance Study," *Photochemistry and Photobiology*, vol. 59, no. 1, pp. 1–4, 2008.

[37] R. Ogura, M. Sugiyama, J. Nishi, and N. Haramaki, "Mechanism of Lipid Radical Formation Following Exposure of Epidermal Homogenate to Ultraviolet Light," *The Journal of Investigative Dermatology*, vol. 97, pp. 1044–1047, 1991.

[38] B. Bose, S. Agarwal, and S. N. Chatterjee, "UV-A induced lipid peroxidation in liposomal membrane," *Radiation and Environmental Biophysics*, vol. 28, pp. 59–65, 1989.

[39] S. T. Durant, K. S. PAffett, M. Shrivastav, G. S. Timmins, W. F. Morgan, and J. A. Nickoloff, "UV Radiation Induces Delayed Hyperrecombination Associated with Hypermutation in Human Cells," *Molecular and Cellular Biology*, vol. 26, no. 16, pp. 6047–6055, 2006.

[40] National Institute for Occupational Safety and Health (NIOSH), `http://www.cdc.gov/niosh/topics/uvradiation/` [Accessed May 2014].

[41] A. K. Benabbou, Z. Derriche, C. Felix, P. Lejeune, and C. Guillard, "Photocatalytic inactivation of *Escherichia coli*: Effect of concentraion of TiO_2 and microorganism, nature, and intensity of UV radiation," *Applied Catalysis B: Environmental*, vol. 76, pp. 257–263, 2007.

[42] P.-C. Maness *et al.*, "Bactericidal Activity of Photocatalytic TiO_2 Reaction: toward an Understanding of Its Killing Mechanism," *Applied Environmental Microbiology*, vol. 65, no. 9, pp. 4094–4098, 1999.

[43] D. F. Ollis, "Phototcatalytic purification and remediation of contaminated air and water," *Comptes Rendus de l'Académie des Sciences - Series IIC - Chemistry*, vol. 3, no. 6, pp. 405–411, 2000.

[44] T. Matsunaga, R. Tomoda, T. Nakajima, and H. Wake, "Photoelectrochemical sterilization of microbial cells by semiconductor powders," *FEMS Microbiology Letters*, vol. 29, pp. 211–214, 1985.

[45] K. P. Kühn *et al.*, "Disinfection of surfaces by photocatalytic oxidation with titanuium dioxide and UVA light," *Chemosphere*, vol. 53, pp. 71–77, 2003.

[46] B. Sánchez *et al.*, "Photocatalytic elimination of indoor air biological and chemical pollution," *Chemosphere*, vol. 87, pp. 625–630, 2012.

[47] O. Raabe, "Über die Wirkung fluoreszierender Stoffe auf Infusorien," *Zeitschrift für Biologie*, vol. 39, pp. 524–526, 1900.

[48] H. von Tappeiner, "Die photodynamische Erscheinung (Sensibilisierung durch fluoresizierende Stoffe," *Ergebnisse der Physiologie*, vol. 8, no. 1, pp. 698–741, 1909.

[49] W. H. Hausmann, "Die sensibilisierende Wirkung tierischer Farbstoffe und ihre physiologische Bedeutung," *Wiener klinische Wochenschriften*, vol. 21, pp. 1527–1529, 1908.

[50] M. Athar and H. M. D. R. Bickers, "Differential role of reactive oxygen intermediates in photofrin-I- and photofrin-II-mediated photoenhancement of lipid peroxidation in epidermal microsomal membranes," *Journal of Investigative Dermatology*, vol. 90, no. 5, pp. 652–657, 1988.

[51] R. W. Redmond and J. N. Gamlin, "A Compilation of Singlet Oxygen Yields from Biologically Relevant Molecules," *Photochemistry and Photobiology*, vol. 70, no. 4, pp. 391–475, 1999.

[52] T. Maisch, "A New Strategy to Destroy Antibiotic Resistant Microorganisms: Antimicrobial Photodynamic Treatment," *Mini-Reviews in Medicinal Chemistry*, vol. 9, pp. 974–983, 2009.

[53] M. R. Hamblin and T. Hasan, "Phjotodynamic therapy: a new antimicrobial approach to infectious disease?," *Photochemical and Photobiological Sciences*, vol. 3, no. 5, pp. 436–450, 2004.

[54] Z. Malik, H. Ladan, and Y. Nitzan, "Photodynamic inactivation of Gram-negative bacteria: problems and possible solutions," *Journal of Photochemistry and Photobiology B: Biology*, vol. 14, no. 3, pp. 262–266, 1992.

[55] T. J. Dougherty *et al.*, "Photodynamic Therapy," *Journal of the National Cancer Institute*, vol. 90, no. 12, pp. 889–905, 1998.

[56] G. Fridman, G. Friedman, A. Gutsol, A. B. Shekhter, V. N. Vasilets, and A. Fridman, "Applied Plasma Medicine," *Plasma Processes and Polymers*, vol. 5, pp. 503–533, 2008.

[57] M. G. Kong, G. Kroesen, G. Morfill, T. Nosenko, T. Shimizu, J. van Dijk, and J. L. Zimmermann, "Plasma medicine: an introductory review," *New Journal of Physics*, vol. 11, p. 115012, 2009.

[58] M. Laroussi, "Low Temperature Plasma-Based Sterilization: Overview and State-of-the-Art," *Plasma Processes and Polymers*, vol. 2, pp. 391–400, 2005.

[59] E. Stoffels, ""Tissue Processing" with Atmospheric Plasmas," *Contributions to Plasma Physics*, vol. 47, no. 1–2, pp. 40–48, 2007.

[60] G. E. Morfill, M. G. Kong, and J. L. Zimmermann, "Focus on Plasma Medicine," *New Journal of Physics*, vol. 11, p. 115011, 2009.

[61] M. Laroussi, "Sterilization of Contaminated Matter with an Atmospheric Pressure Plasma," *IEEE Transactions on Plasma Science*, vol. 24, no. 3, pp. 1188–1191, 1996.

[62] H. W. Herrmann, I. Henins, J. Park, and H. S. Selwyn, "Decontamination of chemical and biological warfare (CBW) agents using an atmospheric pressure plasma jet (APPJ)," *Physics of Plasmas*, vol. 6, no. 5, pp. 2284–2289, 1999.

[63] G. Lloyd *et al.*, "Gas Plasma: Medical Uses and Developments in Wound Care," *Plasma Processes and Polymers*, vol. 7, pp. 194–211, 2010.

[64] P. T. Jacobs and S.-M. Lin, *Disinfection, Sterilization, and Preservation*, ch. 38. Sterilization Processes Utilizing Low-Temperature Plasma, pp. 747–763. Philadelphia, USA: Lippincott Williams and Williams, 2001.

[65] K.-D. Weltmann, M. Polak, K. Masur, T. von Woedtke, J. Winter, and S. Reuter, "Plasma Processes and Plasma Sources in Medicine," *Contributions to Plasma Physics*, vol. 52, no. 7, pp. 644–654, 2012.

[66] N. Barekzi and M. Laroussi, "Effects of Low Temperature Plasmas on Cancer Cells," *Plasma Processes and Polymers*, vol. 10, pp. 1039–1050, 2013.

[67] M. Vandamme, E. Robert, S. Lerondel, V. Sarron, D. Ries, S. Dozias, J. Soblio, D. Gosset, C. Kieda, B. Legrain, J.-M. Pouvesle, and A. L. Pape, "ROS implication in a new antitumor strategy based on non-thermal plasma," *International Journal of Cancer*, vol. 130, pp. 2185–2194, 2012.

[68] G. Isbary, J. L. Zimmermann, Y.-F. Li, G. E. Morfill, H. M. Thomas, B. Steffes, J. Heinlin, S. Karrer, and W. Stolz, "Non-thermal plasma - More than five years of clinical experience," *Clinical Plasma Medicine*, vol. 1, pp. 19–23, 2013.

[69] J. Heinlin, G. Isbary, W. Stolz, G. Morfill, M. Landthaler, T. Shimizu, B. Steffes, T. Nosenko, J. L. Zimmermann, and S. Karrer, "Plasma applciations in medicine with a special focus on dermatology," *Journal of the European Academy of Dermatology and Venereology*, vol. 25, pp. 1–11, 2011.

[70] Y. P. Raizer, *Gas Dicharge Physics*, ch. 12, Spark and Corona Discharges, pp. 324–377. Germany: Springer-Verlag, 1991.

[71] M. A. Malik, A. Ghaffar, and S. A. Malik, "Water purification by electrical discharges," *Plasma Sources Science and Technology*, vol. 10, pp. 82–91, 2001.

[72] S. Pekárek, "DC corona discharge ozone production enhanced by magnetic field," *The European Physical Journal D*, vol. 56, pp. 91–98, 2010.

[73] M. Korachi, Z. Turan, K. Sentürk, F. Sahin, and N. Aslan, "An investigation into the biocidal effect of high voltage AC/DC atmospheric corona discharges on bacteria, yeasts, fungi and algae," *Journal of Electrostatics*, vol. 67, pp. 678–685, 2009.

[74] V. Joubert *et al.*, "Inactivation of *Bacillus subtilis* var. *niger* of both spore and vegetative forms by means of corona discharges applied in water," *Water Research*, vol. 47, pp. 1381–1389, 2013.

[75] V. Scholtz, J. Julák, and V. Kríha, "The Microbicidal Effect of Low-Temperature Plasma Generated by Corona Discharge: Comparison of Various Microorganisms on an Agar Surface or in Aqueous Suspension," *Plasma Processes and Polymers*, vol. 7, pp. 237–243, 2010.

[76] D. Dobrynin, G. Friedman, A. Fridman, and A. Starikovskiy, "Inactivation of bacteria using dc corona discharge: roles of ions and humidity," *New Journal of Physics*, vol. 13, p. 103033, 2011.

[77] Z. Machala, L. Chládeková, and M. Pelach, "Plasma agents in bio-decontamination by dc discharges in atmospheric air," *Journal of Physics D: Applied Physics*, vol. 43, p. 222001, 2010.

[78] M. Yamamoto, M. Nishioka, and M. Sadakata, "Sterilization by H_2O_2 droplets under corona discharge," *Journal of Electrostatics*, vol. 56, pp. 173–187, 2002.

[79] W. Crookes, "On the Illumination of Lines of Molecular Pressure, and the Trajectory of Molecules," *Philosophical Transactions of the Royal Society of London*, vol. 170, pp. 135–164, 1879.

[80] A. von Engel, R. Seeliger, and M. Steenbeck, "Über die Glimmentladung bei hohen Drücken," *Zeitschrift für Physik*, vol. 85, no. 3-4, pp. 144–160, 1933.

[81] J. R. Roth, S. Nourgostar, and T. A. Bonds, "The One Atmosphere Uniform Glow Discharge Plasma (OAUGDP) - A Platform Technology for the 21st Century," *IEEE Transactions on Plasma Science*, vol. 35, no. 2, pp. 233–250, 2007.

[82] J. R. Roth, P. P. Tsai, C. Liu, M. Laroussi, and P. D. Spence, "One Atmosphere Uniform Glow Discharge Plasma." U.S. Patent: 5 414 324. May 9, 1995.

[83] T. C. Montie, K. Kelly-Wintenberg, and J. R. Roth, "An Overview of Research Using the One Atmosphere Glow Discharge Plasma (OAUGDP) for Sterilization of Surfaces and Materials," *IEEE Transactions on Plasma Science*, vol. 28, no. 1, pp. 41–50, 2000.

[84] K. Kelly-Wintenberg, T. C. Montie, J. R. Roth, A. K. Carr, K. Sorge, L. C. Wadsworth, and P. P. Y. Tsai, "Room temperature sterilization of surfaces and fabrics with a One Atmosphere Uniform Glow Discharge Plasma," *Journal of Industrial Microbiology and Biotechnology*, vol. 20, pp. 69–74, 1998.

[85] M. Vleugels, G. Shama, X. T. Deng, E. Greenacre, T. Brocklehurst, and M. G. Kong, "Atmospheric Plasma Inactivation of Biofilm-Forming Bacteria for Food Safety Control," *IEEE Transactions on Plasma Science*, vol. 33, no. 2, pp. 824–828, 2005.

[86] J. Y. Jeong, S. E. Babayan, V. J. Tu, J. Park, I. Henins, R. F. Hicks, and G. S. Selwyn, "Etching materials with an atmospheric-pressure jet," *Plasma Sources Science and Technology*, vol. 7, pp. 282–285, 1998.

[87] S. E. Babayan, J. Y. Jeong, V. J. Tu, J. Park, G. S. Selwyn, and R. F. Hicks, "Deposition of silicon dioxide films with an atmospheric-pressure plasma jet," *Plasma Sources Science and Technology*, vol. 7, pp. 286–288, 1998.

[88] A. Schütze, J. Y. Jeong, S. E. Babayan, J. Park, G. S. Selwyn, and R. F. Hicks, "The atmospheric-pressure plasma jet: A review and comparison to other plasma sources," *IEEE Transactions on Plasma Science*, vol. 26, no. 6, pp. 1685–1694, 1998.

[89] X. Lu, M. Laroussi, and V. Puech, "On atmospheric-pressure non-equilibrium plasma jets and plasma bullets," *Plasma Sources Science and Technology*, vol. 21, p. 034005, 2012.

[90] M. Laroussi and T. Akan, "Arc-Free Atmospheric Pressure Cold Plasma Jets: A Review," *Plasma Polymers and Processes*, vol. 4, pp. 777–788, 2007.

[91] C. Tendero, C. Tixier, P. Tristant, J. Desmaison, and P. Leprince, "Atmospheric pressure plasmas: A review," *Spectrochimica Acta Part B*, vol. 61, pp. 2–30, 2006.

[92] J. Ehlbeck, U. Schnabel, M. Polak, T. von Woedtke, R. Brandenburg, T. von dem Hagen, and K.-D. Weltmann, "Low temperautre atmospheric pressure plasma sources for microbial decontamination," *Journal of Physics D: Applied Physics*, vol. 44, p. 013002, 2011.

[93] K.-D. Weltmann, E. Kindel, R. Brandenburg, C. Meyer, R. Bussiahn, C. Wilke, and T. von Woedtke, "Atmospheric Pressure Plasma Jet for Medical Therapy: Plasma Parameters and Risk Estimation," *Contribuions to Plasma Physics*, vol. 49, no. 9, pp. 631–640, 2009.

[94] G. Daeschlein, T. von Woedtke, E. Kindel, R. Brandenburg, K.-D. Weltmann, and M. Jünger, "Antibacterial Activity of an Atmospheric Pressure Plasma Jet Against Relevant Wound Pathogens in vitro on a Simulated Wound Environment," *Plasma Processes and Polymers*, vol. 7, pp. 224–230, 2010.

[95] M. Laroussi, C. Tendero, X. Lu, S. Alla, and W. L. Hynes, "Inactivation of Bacteria by the Plasma Pencil," *Plasma Processes and Polymers*, vol. 3, pp. 470–473, 2007.

[96] K.-D. Weltmann, R. Brandenburg, T. von Woedtke, J. Ehlbeck, R. Foest, M. Stieber, and E. Kindel, "Antimicrobial treatment of heat sensitive products by miniaturized atmospheric pressure plasma jets (APPJs)," *Journal of Physics D: Applied Physics*, vol. 41, p. 194008, 2008.

[97] R. Brandenburg, J. Ehlbeck, M. Stieber, T. von Woedtke, J. Zeymer, O. Schlüter, and K.-D. Weltmann, "Antimicrobial Treatment of Heat Sensitive Materials by Means of Atmospheric Pressure RF-Driven Plasma Jet," *Contributions to Plasma Physics*, vol. 47, no. 1-2, pp. 72–79, 2007.

[98] E. Stoffels, A. J. Flikweert, W. W. Stoffels, and G. M. W. Kroesen, "Plasma needle: a non-destructive atmospheric plasma source for fine surface treatment of (bio)materials," *Plasma Sources Science and Technology*, vol. 11, pp. 383–388, 2002.

[99] R. E. J. Sladek and E. Stoffels, "Deactivation of *Escherichia coli* by the plasma needle," *Journal of Physics D: Applied Physics*, vol. 38, pp. 1716–1721, 2005.

[100] M. Laroussi and X. Lu, "Room-temperature atmospheric pressure plasma plume for biomedical applications," *Applied Physics Letters*, vol. 87, p. 113902, 2005.

[101] M. Moisan, Z. Zakrzewski, R. Grenier, and G. Sauvé, "Large Diameter Plasma Generation Using a Waveguide-Based Field Applicator at 2.45 GHz," *Journal of Microwave Power and Electromagnetic Energy*, vol. 30, no. 1, pp. 58–65, 1995.

[102] H. S. Uhm, Y. C. Hong, and D. H. Shin, "A microwave plasma torch and its applications," *Plasma Sources Science and Technology*, vol. 15, pp. S26–S34, 2006.

[103] R. Stonies, S. Schermer, E. Voges, and J. A. C. Broekaert, "A new small microwave plasma torch," *Plasma Sources Science and Technology*, vol. 13, pp. 604–611, 2004.

[104] M. Jasinski, J. Mizeraczyk, Z. Zakrzewski, T. Ohkubo, and J.-S. Chang, "CFC-11 destruction by microwave torch generated atmospheric-pressure nitrogen discharge," *Journal of Physics D: Applied Physics*, vol. 35, pp. 2274–2280, 2002.

[105] K. M. Green, M. C. Borrás, P. P. Woskov, G. J. Flores, K. Hadidi, and P. Thomas, "Electronic Excitation Temperature Profiles in an Air Microwave Plasma Torch," *IEEE Transactions on Plasma Science*, vol. 29, no. 2, pp. 399–406, 2001.

[106] C. H. Kruger, "Nonequilibrium Effects in Thermal Plasma Chemistry," *Plasma Chemistry and Plasma Processing*, vol. 9, no. 4, pp. 435–443, 1989.

[107] C. H. Kruger, T. G. Owano, and C. O. Laux, "Experimental Investigation of Atmospheric Pressure Nonequilibrium Plasma Chemistry," *IEEE Transactions on Plasma Science*, vol. 25, no. 5, pp. 1042–1051, 1997.

[108] H. J. Kim and S. H. Hong, "Comparative Measurements on Thermal Plasma Jet Characteristics in Atmospheric and Low Pressure Plasma Sprayings," *IEEE Transactions on Plasma Science*, vol. 23, no. 5, pp. 852–859, 1995.

[109] T. Shimizu, B. Steffes, R. Pompl, F. Jamitzky, W. Bunk, K. Ramrath, M. Georgi, W. Stolz, H.-U. Schmidt, T. Urayama, S. Fujii, and G. E. Morfill, "Characterization of Microwave Plasma Torch for Decontamination," *Plasma Processes and Polymers*, vol. 5, pp. 577–582, 2008.

[110] W. Lai, H. Lai, and S. P. Kuo, "Decontamination of biological warfare agents by a microwave plasma torch," *Physics of Plasmas*, vol. 12, p. 023501, 2005.

[111] T. Sato, A. Doi, T. Urayama, T. Nakatani, and T. Miyahara, "Inactivation of *Escherichia coli* by a Coaxial Microwave Plasma Flow," *IEEE Transactions on Industry Applications*, vol. 43, no. 5, pp. 1159–1163, 2007.

[112] T. Shimizu, T. Nosenko, G. E. Morfill, T. Sato, H.-U. Schmidt, and T. Urayama, "Characterization of Low-Temperature Microwave Plasma Treatment With and Without UV Light for Disinfection," *Plasma Processes and Polymers*, vol. 7, pp. 288–293, 2010.

[113] J. Ehlbeck, A. Ohl, M. Maaß, U. Krohmann, and T. Neumann, "Moving atmospheric microwave plasma for surface and volume treatment," *Surface and Coating Technology*, vol. 174–175, pp. 493–497, 2003.

[114] S. P. Kuo, O. Tarasenko, S. Popovic, and K. Levon, "Killing of Bactericidal Spores Contained in a Paper Envelope by a Microwave Plasma Torch," *IEEE Transactions on Plasma Science*, vol. 34, no. 4, pp. 1275–1280, 2006.

[115] S. Moreau, M. Moisan, M. Tabrizian, J. Barbeau, J. Pelletier, A. Richard, and L. Yahia, "Using the flowing afterglow of a plasma to inactivate *Bacillus subtilis* spores: Influence of the operating conditions," *Journal of Applied Physics*, vol. 88, no. 2, pp. 1166–1174, 2000.

[116] S. Lerouge, M. R. Wertheimer, and L. Yahia, "Plasma Sterilization: A Review of Parameters, Mechanisms, and Limitations," *Plasma and Polymers*, vol. 6, no. 3, pp. 175–188, 2001.

[117] G. Isbary, G. Morfill, H.-U. Schmidt, M. Georgi, K. Ramrath, J. Heinlin, S. Karrer, M. Landthaler, T. Shimizu, B. Steffes, W. Bunk, R. Monetti, J. L. Zimmermann, R. Pompl, and W. Stolz, "A first prospective randomized controlled trial to decrease bacterial load using cold atmospheric argon plasma on chronic wounds in patients," *British Journal of Dermatology*, vol. 163, pp. 78–82, 2010.

[118] G. Isbary, J. Heinlin, T. Shimizu, J. L. Zimmermann, G. Morfill, H.-U. Schmidt, R. Monetti, B. Steffes, W. Bunk, Y.-F. Li, T. Klaempfl, S. Karrer, M. Landthaler, and W. Stolz, "Successful and safe use of 2 min cold atmospheric argon plasma in chronic wounds: results of a randomized controlled trial," *Biritsh Journal of Dermatology*, vol. 167, pp. 404–410, 2012.

[119] S. Arndt, P. Unger, E. Wacker, T. Shimizu, J. Heinlin, Y.-F. Li, H. M. Thomas, G. E. Morfill, J. L. Zimmermann, A.-K. Bosserhoff, and S. Karrer, "Cold Atmospheric Plasma (CAP) Changes Gene Expression of Key Molecules of the Wound Healing Machinery and Improves Wound Healing *In Vitro* and *In Vivo*," *PLOS ONE*, vol. 8, no. 11, p. e79325, 2013.

[120] W. Siemens, "Ueber die elektrostatische Induktion und die Verzögerung des Stroms in Falschendrähten," *Poggendorffs Annalen der Physik und Chemie*, vol. 102, pp. 66–122, 1857.

[121] U. Kogelschatz, B. Eliasson, and W. Egli, "From ozone generators to flat television screens: history and future potential of dielectric-barrier discharges," *Pure and Applied Chemistry*, vol. 71, no. 10, pp. 1819–1828, 1999.

[122] T. Andrews, "On the Continuity of the Gaseous and Liquid States of Matter," *Philosophical Society of London*, vol. 159, pp. 575–590, 1869.

[123] V. I. Gibalov and G. J. Pietsch, "Dynamics of dielectric barrier discharges in different arrangements," *Plasma Sources Science and Technology*, vol. 21, p. 024010, 2012.

[124] N. Gherardi, G. Gouda, E. Gat, A. Richard, and F. Massines, "Transition from glow silent discharge to micro-discharges in nitrogen gas," *Plasma Sources Science and Technology*, vol. 9, pp. 340–346, 2000.

[125] N. Gherardi and F. Massines, "Mechanisms Controlling the Transition from Glow Silent Discharge to Streamer Discharge in Nitrogen," *IEEE Transactions on Plasma Science*, vol. 29, no. 3, pp. 536–544, 2001.

[126] H.-E. Wagner, R. Brandenburg, K. V. Kozlov, A. Sonnenfeld, P. Michel, and J. F. Behnke, "The barrier discharge: basic properties and applications to surface treatment," *Vacuum*, vol. 71, pp. 417–436, 2003.

[127] A. Bogaerts, E. Neyts, R. Gijbels, and J. van der Mullen, "Gas discharge plasmas and their application," *Spectrochimica Acta Part B*, vol. 57, pp. 609–658, 2002.

[128] A. Fridman, A. Chirokov, and A. Gutsol, "Non-thermal atmospheric pressure discharges," *Journal of Physics D: Applied Physics*, vol. 38, pp. R1–R24, 2005.

[129] F.-J. Trompeter, W. J. Neff, O. Franken, M. Heise, M. Neiger, S. Liu, G. J. Pietsch, and A. B. Saveljew, "Reduction of *Bacillus Subtilis* and *Aspergillus Niger* Spores Using Nonthermal Atmospheric Gas Discharges," *IEEE Transactions on Plasma Science*, vol. 30, no. 4, pp. 1416–1423, 2002.

[130] J. H. Choi, I. Han, H. K. Baik, M. H. Lee, D. W. Han, J. C. Park, I. S. Lee, K. M. Song, and Y. S. Lim, "Analysis of sterilization effect by pulsed dielectric barrier discharge," *Journal of Electrostatics*, vol. 64, pp. 17–22, 2006.

[131] M. Vandamme, E. Robert, S. Pesnel, E. Barbosa, S. Dozias, J. Soblio, S. Lerondel, A. L. Pape, and J.-M. Pouvesle, "Antitumor Effect of Plasma Treatment on U87 Glioma Xenografts: Preliminary Results," *Plasma Processes and Polymers*, vol. 7, pp. 264–273, 2010.

[132] H. Eto, Y. Ono, A. Ogino, and M. Nagatsu, "Low-temperature sterilization of wrapped materials using flexible sheet-type dielectric barrier discharge," *Applied Physics Letters*, vol. 93, p. 221502, 2008.

[133] G. Fridman, M. Peddinghaus, H. Ayan, A. Fridman, M. Balasubramanian, A. Gutsol, A. Brooks, and G. Friedman, "Blood Coagulation and Living Tissue Sterilization by Floating-Electrode Dielectric Barrier Discharge in Air," *Plasma Chemistry and Plasma Processing*, vol. 26, pp. 425–442, 2006.

[134] G. Fridman, A. Shereshevsky, M. M. Jost, A. D. Brooks, A. Fridman, A. Gutsol, V. Vasilets, and G. Friedman, "Floating Electrode Dielectric Barrier Discharge Plasma in Air Promoting Apoptotic Behavior in Melanoma Skin Cancer Cell Lines," *Plasma Chemistry and Plasma Processing*, vol. 27, pp. 163–176, 2007.

[135] G. Fridman, A. D. Brooks, M. Balasubramanian, A. Fridman, A. Gutsol, V. N. Vasilets, H. Ayan, and G. Friedman, "Comparison of Direct and Indirect Effects of Non-Thermal Atmospheric-Pressure Plasma on Bacteria," *Plasma Processes and Polymers*, vol. 4, pp. 370–375, 2007.

[136] S. G. Joshi, M. Paff, G. Friedman, G. Fridman, A. Fridman, and A. D. Brooks, "Control of methicillin-resistant *Staphylococcus aureus* in planktonic form and biofilms: A biocidal efficacy study of nonthermal dielectric-barrier discharge plasma," *American Journal of Infection Control*, vol. 38, pp. 293–301, 2010.

[137] S. G. Joshi, M. Cooper, A. Yost, M. Paff, U. K. Ercan, G. Fridman, G. Friedman, A. Fridman, and A. D. Brooks, "Nonthermal Dielectric-Barrier Discharge Plasma-Induced Inactivation Involves Oxidative DNA Damage and Membrane Lipid Peroxidation in *Escherichia coli*," *Antimicrobial Agents and Chemotherapy*, vol. 55, no. 3, pp. 1053–1062, 2011.

[138] M. Cooper, G. Fridman, D. Staack, A. F. Gutsol, V. N. Vasilets, S. Anandan, Y. I. Cho, A. Fridman, and A. Tsapin, "Decontamination of Surfaces From Extremophile Organismus Using Nonthermal Atmospheric-Pressure Plasmas," *IEEE Transactions on Plasma Science*, vol. 37, no. 6, pp. 866–871, 2009.

[139] M. J. Gallagher, N. Vaze, S. Gangoli, V. N. Vasilets, A. F. Gutsol, T. N. Milovanova, S. Anandan, D. M. Murasko, and A. A. Fridman, "Rapid Inactivation of Airborne Bacteria Using Atmospheric Pressure Dielectric Barrier Grating Discharge," *IEEE Transactions on Plasma Science*, vol. 35, no. 5, pp. 1501–1510, 2007.

[140] F. Leipold, Y. Kusano, F. Hansen, and T. Jacobsen, "Decontamination of a rotating cutting tool during operation by means of atmospheric pressure plasmas," *Food Control*, vol. 21, pp. 1194–1198, 2010.

[141] A. Schwabedissen, P. Lacinski, X. Chen, and J. Engemann, "*PlasmaLabel* - a New Method to disinfect Goods Inside a Closed Package Using Dielectric Barrier Discharges," *Contribution to Plasma Physics*, vol. 47, no. 7, pp. 551–558, 2007.

[142] H. Eto, Y. Ono, A. Ogino, and M. Nagatsu, "Low-Temperature Internal Sterilization of Medical Plastic Tubes Using a Linear Dielectric Barrier Discharge," *Plasma Processes and Polymers*, vol. 5, pp. 269–274, 2008.

[143] Y.-F. Li, T. Shimizu, J. L. Zimmermann, and G. E. Morfill, "Cold Atmospheric Plasma for Surface Disinfection," *Plasma Processes and Polymers*, vol. 9, pp. 585–589, 2012.

[144] M. Heise, T. Lierfeld, O. Franken, and W. Neff, "Single filament charge transfer and UV-emission properties of a cascaded dielectric barrier discharge (CDBD) set-up," *Plasma Sources Science Technology*, vol. 13, pp. 351–358, 2004.

[145] M. Heise, W. Neff, O. Franken, P. Muranyi, and J. Wunderlich, "Sterilization of Polymer Foils with Dielectric Barrier Discharges at Atmospheric Pressure," *Plasma and Polymers*, vol. 9, no. 1, pp. 23–33, 2004.

[146] A. Chirokov, A. Gutsol, A. Fridman, K. D. Sieber, J. M. Grace, and K. S. Robinson, "Analysis of two-dimensional microdischarge distribution in dielectric-barrier discharges," *Plasma Sources Science and Technology*, vol. 13, pp. 623–635, 2004.

[147] U. Kogelschatz, "Dielectric-barrier Discharges: Their History, Discharge Physics, and Industrial Applications," *Plasma Chemistry and Plasma Processing*, vol. 23, no. 1, pp. 1–46, 2003.

[148] H. Ayan, G. Fridman, A. F. Gutsol, V. N. Vasilets, A. Fridman, and G. Friedman, "Nanosecond-Pulsed Uniform Dielectric-Barrier Discharge," *IEEE Transactions on Plasma Science*, vol. 36, no. 2, pp. 504–508, 2008.

[149] N. D. Geyter, R. Morent, and C. Leys, "Penetration of a dielectric barrier discharge plasma into textile structures at medium pressure," *Plasma Sources Science and Technology*, vol. 15, pp. 78–84, 2006.

[150] T. Shimizu, J. L. Zimmermann, and G. E. Morfill, "The bactericidal effect of surface micro-discharge plasma under different ambient conditions," *New Journal of Physics*, vol. 13, p. 023026, 2011.

[151] V. I. Gibalov and G. J. Pietsch, "The development of dielectric barrier discharges in gas gaps and on surfaces," *Journal of Physics D: Applied Physics*, vol. 33, pp. 2618–2636, 2000.

[152] T. Maisch, T. Shimizu, Y.-F. Li, J. Heinlin, S. Karrer, G. Morfill, and J. L. Zimmermann, "Decolonisation of MRSA, *S. aureus* and *E. coli* by Cold-Atmospheric Plasma Using a Porcine Skin Model *In Vitro*," *PLoS One*, vol. 7, no. 4, p. e34610, 2012.

[153] T. Maisch, T. Shimizu, G. Isbary, J. Heinlin, S. Karrer, T. G. Klämpfl, Y.-F. Li, G. Morfill, and J. L. Zimmermann, "Contact-Free Inactivation of *Candida albicans* Biofilms by Cold Atmospheric Air Plasma," *Applied and Environmental Microbiology*, vol. 78, no. 12, pp. 4242–4247, 2012.

[154] T. Maisch, T. Shimizu, A. Mitra, J. Heinlin, S. Karrer, Y.-F. Li, G. Morfill, and J. L. Zimmermann, "Contact-free cold atmospheric plasma treatment of *Deinococcus radiodurans*," *Journal of Indstrial Microbiology and Biotechnology*, vol. 39, pp. 1367–1375, 2012.

[155] T. G. Klämpfl, G. Isbary, T. Shimizu, Y.-F. Li, J. L. Zimmermann, W. Stolz, J. Schlegel, G. E. Morfill, and H.-U. Schmidt, "Cold Atmospheric Air Plasma Sterilization against Spores and Other Microorganisms of Clinical Interest," *Applied and Environmental Microbiology*, vol. 78, no. 15, pp. 5077–5082, 2012.

[156] J. L. Zimmermann, K. Dumler, T. Shimizu, G. E. Morfill, A. Wolf, V. Boxhammer, J. Schlegel, B. Gansbacher, and M. Anton, "Effects of cold atmospheric plasmas on adenoviruses in solution," *Journal of Physics D: Applied Physics*, vol. 44, p. 505201, 2011.

[157] J. Köritzer, V. Boxhammer, A. Schäfer, T. Shimizu, T. G. Klämpfl, Y.-F. Li, C. W. andn S Schwenk-Ziegler, G. E. Morfill, J. L. Zimmermann, and J. Schlegel, "Restoration of sensitivity in Chemo-Resistant Glioma Cells by Cold Atmospheric Plasma," *PLOS ONE*, vol. 8, no. 5, p. e64498, 2013.

[158] S. Arndt, E. Wacker, Y.-F. Li, T. Shimizu, H. M. Thomas, G. E. Morfill, S. Karrer, J. L. Zimmermann, and A.-K. Bosserhoff, "Cold atmospheric plasma, a new strategy to induce senescence in melanoma cells," *Experimental Dermatology*, vol. 22, pp. 284–289, 2013.

[159] A. Mitra, Y.-F. Li, T. G. Klämpfl, T. Shimizu, J. Jeon, G. E. Morfill, and J. L. Zimmermann, "Inactivation of Surface-Borne Microorganisms and Increased Germination of Seed Specimen by Cold Atmospheric Plasma," *Food and Bioprocess Technology*, vol. 7, no. 3, pp. 645–653, 2013.

[160] J. L. Zimmermann, T. Shimizu, V. Boxhammer, and G. E. Morfill, "Disinfection Through Different Textiles Using Low-Temperature Atmospheric Pressure Plasma," *Plasma Processes and Polymers*, vol. 9, pp. 792–198, 2012.

[161] G. Isbary, J. Köritzer, A. Mitra, Y.-F. Li, T. Shimizu, J. Schroeder, J. Schlegel, G. E. Morfill, W. Stolz, and J. L. Zimmermann, "*Ex vivo* human skin experiments for the evaluation of safety of new cold atmospheric plasma devices," *Clinical Plasma Medicine*, vol. 1, pp. 36–44, 2013.

[162] V. Boxhammer, Y.-F. Li, J. Köritzer, T. Shimizu, T. Maisch, H. M. Thomas, J. Schlegel, G. E. Morfill, and J. L. Zimmermann, "Investigation of the mutagenic potential of cold atmospheric plasma at bactericidal dosages," *Mutation Research*, vol. 753, pp. 23–28, 2013.

[163] C. Welz, S. Becker, Y.-F. Li, T. Shimizu, J. Jeon, S. Schwenk-Ziegler, H. M. Thomas, G. Isbary, G. E. Morfill, U. Harréus, and J. L. Zimmermann, "Effects of cold atmospheric plasma on mucocal tissue culture," *Journal of Physics D: Applied Physics*, vol. 46, p. 045401, 2013.

[164] V. Boxhammer, G. E. Morfill, J. R. Jokipii, T. Shimizu, T. Klämpfl, Y.-F. Li, J. Köritzer, J. Schlegel, and J. L. Zimmermann, "Bacericidal actionn of cold atmospheric plasma insolution," *New Journal of Physics*, vol. 14, p. 113042, 2012.

[165] T. Shimizu, Y. Sakiyama, D. B. Graves, J. L. Zimmermann, and G. E. Morfill, "The dynamics of

ozone generation and mode transition in air surface micro-discharge plasma at atmospheric pressure," *New Journal of Physics*, vol. 14, p. 103028, 2012.

[166] J. S. Townsend, *Electricity in Gases*. Clarendon Press, 1915.

[167] Y. B. Golubovskii, V. A. Maiorov, J. Behnke, and J. F. Behnke, "Influence of interaction between charged particles and dielectric surface over a homogeneous barrier discharge in nitrogen," *Journal of Physics D: Applied Physics*, vol. 35, pp. 751–761, 2002.

[168] A. N. Kontaratos, "On the Functional Dependence of Townsend's First Ionization Coefficient," *Applied Science Research, Section A*, vol. 12, no. 1, pp. 27–32, 1965-1966.

[169] L. B. Loeb and J. M. Meek, "The Mechanism of Spark Discharge in Air at Atmospheric Pressure. I," *Journal of Applied Physics*, vol. 11, pp. 438–447, 1940.

[170] G. Steinle, D. Neundorf, W. Hiller, and M. Pietralla, "Two-dimensional simulation of filaments in barrier discharges," *Journal of Physics D: Applied Physics*, vol. 32, pp. 1350–1356, 1999.

[171] D. Braun, V. Gibalov, and G. Pietsch, "Two-dimensional modeling of the dielectric barrier discharge in air," *Plasma Sources Science and Technology*, vol. 1, no. 3, pp. 166–174, 1992.

[172] A. Fridman, *Plasma Chemistry*, ch. 4. Electric Discharges in Plasma Chemistry, pp. 157–258. Cambridge University Press, 2008.

[173] K. H. Wagner, "Die Entwicklung der Elektronenlawine in den Plamakanal, untersucht mit Bildverstärker und Wischverschluß," *Zeitschrift für Physik*, vol. 189, pp. 465–515, 1966.

[174] A. J. Davies, C. S. Davies, and C. J. Evans, "Computer simulation of rapidly developing gaseous discharges," *Proceedings of the Institution of Electrical Engineers - London*, vol. 118, no. 6, pp. 816–823, 1971.

[175] H. Raether, "Die Entwicklung der Elektronenlawine in den Funkenkanal," *Zeitschrift für Physik*, vol. 112, no. 7–8, pp. 464–489, 1939.

[176] H. Raether, "Zur Entwicklung von Kanalentladungen," *Archiv für Elektrotechnik*, vol. 34, pp. 49–56, 1940.

[177] A. J. Palmer, "A physical model on the initiation of atmospheric-pressure glow discharges," *Applied Physics Letters*, vol. 25, no. 3, pp. 138–140, 1974.

[178] A. A. Kulikovksy, "Positive streamer in a weak field in air: A moving avalanche-to-streamer tansition," *Physical Review E*, vol. 57, no. 6, pp. 7066–7074, 1998.

[179] A. L. Ward, "Effect of Space Charge in Cold-Cathode Gas Discharges," *Physical Review*, vol. 112, no. 6, pp. 1852–1857, 1958.

[180] U. K. und B Eliasson and W. Egli, "Dielectric-Barrier Discharges. Principles and Applications," *Journal de Physique IV*, vol. 7, no. C4, pp. 47–66, 1997. Conference: 23rd International Conference on Phenomena in Ionized Gases, Toulouse, France.

[181] T. Shimizu, Y. Iwafuchi, G. E. Morfill, and T. Sato, "Formation of thermal flow fields and chemical transport in air and water by atmospheric plasma," *New Journal of Physics*, vol. 13, p. 053025, 2011.

[182] M. Moisan, J. Barbeau, S. Moreau, J. Pelletier, M. Tabrizian, and L. Yahia, "Low-temperature sterilization usinig gas plasmas: a review of the experiments and an analysis of the inactivation mechanisms," *International Journal of Pharmaceutics*, vol. 226, pp. 1–21, 2001.

[183] M. Moisan, J. Barbeau, M.-C. Crevier, J. Pelletier, N. Philip, and B. Saoudi, "Plasma sterilization. Methods and mechanisms," *Pure and Applied Chemistry*, vol. 74, no. 3, pp. 349–358, 2002.

[184] X. Deng, J. Shi, and M. G. Kong, "Physical Mechanisms of Inactivation of *Bacillus subtilis* Spores Using Cold Atmospheric Plasmas," *IEEE Transactions on Plasma Science*, vol. 34, no. 4, pp. 1310–1316, 2006.

[185] M. Laroussi, "Nonthermal Decontamination of Biological Media by Atmospheric-Pressure Plasmas: Review, Analysis, and Prospects," *IEEE Transactions on Plasma Science*, vol. 30, no. 4, pp. 1409–1415, 2002.

[186] M. Laroussi and F. Leipold, "Evaluation of the roles of reactive species, heat, and UV radiation in the inactivation of bacterial cells by air plasmas at atmospheric pressure," *International Journal of Mass Spectrometry*, vol. 233, pp. 81–86, 2004.

[187] M. K. Boudam, M. Moisan, B. Saoudi, C. Popovici, N. Gherardi, and F. Massines, "Bacterial spore inactivation by atmospheric-pressure plasmas in the presence or absence of UV photons as obtained with the same gas mixture," *Journal of Physics D: Applied Physics*, vol. 39, pp. 3494–3507, 2006.

[188] Y. Sakiyama and D. B. Graves, "Efficient modeling of atmospheric pressure surface microdischarge plasma chemistry," *Plasma Sources Science and Technology*, vol. 22, p. 012003, 2013.

[189] Y. Sakiyama, D. B. Graves, H.-W. Chang, T. Shimizu, and G. E. Morfill, "Plasma chemistry model of surface microdischarge in humid air and dynamics of reactive neutral species," *Journal of Physics D: Applied Physics*, vol. 45, p. 425201, 2012.

[190] R. Dorai and M. J. Kushner, "A model for plasma modification of polypropylene using atmospheric pressure discharges," *Journal of Physics D: Applied Physics*, vol. 36, pp. 666–685, 2003.

[191] D. B. Graves, "The emerging role of reactive oxygen and nitrogen species in redox biology and some implications for plasma applications to medicine and biology," *Journal of Physics D: Applied Physics*, vol. 45, p. 263001, 2012.

[192] A. J. H. Sale and W. A. Hamilton, "Effects of High Electric Fields on Microorganisms: I. Killing on Bacteria and Yeasts," *Biochimica et Biophysica Acta*, vol. 148, pp. 781–788, 1967.

[193] K. H. Schoenbach, F. E. Peterkin, R. W. Alden, and S. J. Beebe, "The Effect of Pulsed Electric Fields on Biological Cells - Experiments and Applications," *IEEE Transactions on Plasma Science*, vol. 25, no. 2, pp. 284–292, 1997.

[194] A. Mizuno and Y. Hori, "Destruction of Living Cells by Pulsed High-Voltage Application," *IEEE Transactions on Industry Applications*, vol. 24, no. 3, pp. 387–394, 1988.

[195] H. Hülsheger, J. Potel, and E.-G. Niemann, "Killing of Bacteria with Electric Pulses of High Field Strength," *Radiation and Environmental Biophysics*, vol. 20, pp. 53–65, 1981.

[196] W. A. Hamilton and A. J. H. Sale, "Effects of High Electric Fields on Microorganisms: II. Mechanism of Action of the Lethal Effect," *Biochimica et Biophysica ACta*, vol. 148, pp. 789–800, 1967.

[197] S. Ravinshankar, H. Zhang, and M. L. Kempkes, "Pulsed Electric Fields," *Food Science and Technology International*, vol. 14, no. 5, pp. 429–432, 2008.

[198] D. Dobrynin, G. Fridman, G. Friedman, and A. Fridman, "Physical and biological mechanisms of direct plasma interaction with living tissues," *New Journal of Physics*, vol. 11, p. 115020, 2009.

[199] D. A. Mendis, M. Rosenberg, and F. Azam, "A Note on Possible Electrostatic Disruption of Bacteria," *IEEE Transactions on Plasma Science*, vol. 28, no. 4, pp. 1304–1306, 2000.

[200] M. Laroussi, D. A. Mendis, and M. Rosenberg, "Plasma interaction with microbes," *New Journal of Physics*, vol. 5, pp. 41.1–41.10, 2003.

[201] E. Stoffels, Y. Sakiyama, and D. B. Graves, "Cold Atmospheric Plasma: Charged Species and Their Interactions With Cells and Tissues," *IEEE Transactions on Plasma Science*, vol. 36, no. 4, pp. 1441–1457, 2008.

[202] A. T. Poortinga, J. Smit, H. C. van der Mei, and H. J. Busscher, "Electric Field Induced Desorption of Bacteria from a Conditioning Film Covered Substratum," *Biotechnology and Bioengineering*, vol. 76, no. 4, pp. 395–399, 2001.

[203] J. Raiser and M. Zenker, "Argon plasma coagulation for open surgical and endoscopic applications: state of the art," *Journal of Physics D: Applied Physics*, vol. 39, pp. 3520–3523, 2006.

[204] P. Brandt, 2012. Discussions on the modeling of the gas exchange processes with different geometries.

[205] T. C. Manley, "The Electric Characteristics of the Ozonator Discharge," *Journal of The Electrochemical Society*, vol. 84, no. 1, pp. 83–96, 1943.

[206] E. C. Y. Inn and Y. Tanaka, "Absorption Coefficient of Ozone in the Ultraviolet and Visible Regions," *Journal of the Optical Society of America*, vol. 43, no. 10, pp. 870–873, 1953.

[207] E. C. Y. Inn and Y. Tanaka, "Ozone Absorption Coefficients in the Visible and Ultraviolet Region," *Advances in Chemistry*, vol. 21, pp. 263–268, 1959.

[208] M. Griggs, "Absorption Coefficients of Ozone in the Ultraviolet and Visible Regions," *The Journal of Chemical Physics*, vol. 49, no. 2, pp. 857–859, 1968.

[209] J. A. R. Samson, *Techniques of Vacuum Ultraviolet Spectrscopy*. New York, USA: John Wiley & Sons Ltd., 1967.

[210] R. D. Hudson, "Critical Review of Ultraviolet Photoabsorption Cross Sections for Molecules of Astrophysical and Aeronomic Interest," *Reviews of Geographics and Space Physics*, vol. 9, no. 2, pp. 305–406, 1971.

[211] L. T. Molina and M. J. Molina, "Absolute Absorption Cross Sections of Ozone in the 185- to 350-nm Wavelength Range," *Journal of Geophysical Research*, vol. 91, no. D13, pp. 14501–14508, 1986.

[212] J. M. Willey, L. M. Sherwood, and C. J. Woolverton, *Prescott's Microbiology*. New York, USA: McGraw-Hill, 8th ed., 2011.

[213] J. G. Cappuccino and N. Sherman, *Microbiology: Laboratory Manual*. Boston, USA: Cummings et al., 9th and international ed., 2011.

[214] W. F. Meggers, C. H. Corliss, and B. F. Scribner, *Tables of Spectral-Line Intensities Part I - Arranged by Elements*. National Bureau of Standards Monograph, 1975.

[215] A. Kramida, Y. Ralchenko, and J. Reader, "NIST Atomic Spectra Database (ver. 5.1)," 2013. [Online]. Available: http://physics.nist.gov/asd [2014, August 4]. National Institute of Standards and Technology, Gaithersburg, MD, USA.

[216] A. D. Grossman, "Genetic Networks Controlling the Initiation of Sporulation and the Development of Genetic Competence in *Bacillus subtilis*," *Annual Review of Genetics*, vol. 29, pp. 477–508, 1995.

[217] J. A. Hoch, "Regulation of Phosphorelay and the Initiation of Sporulation in *Bacillus subtilis*," *Annual Review of Microbiology*, vol. 47, pp. 441–465, 1993.

[218] P. Stragier and R. Losick, "Molecular Genetics of Sporulation in *Bacillus subtilis*," *Annual Review of Genetics*, vol. 30, pp. 297–341, 1996.

[219] G. Horneck, D. M. Klaus, and R. L. Mancinelli, "Space Microbiology," *Microbiology and Molecular Biology Reviews*, vol. 74, no. 1, pp. 121–156, 2010.

[220] W. L. Nicholson, N. Munakata, G. Horneck, H. J. Melosh, and P. Setlow, "Resistance of *Bacillus* Endospores to Extreme Terrestrial and Extraterrestrial Environments," *Microbiology and Molecular Biology Reviews*, vol. 64, no. 3, pp. 548–572, 2000.

[221] P. Setlow, "Mechanisms for the Prevention of Damage to DNA in Spores of *Bacillus* Species," *Annual Review of Microbiology*, vol. 49, pp. 29–54, 1995.

[222] G. Horneck, P. Rettberg, G. Reitz, J. Wehner, U. Eschweiler, K. Strauch, C. Panitz, V. Starke, and C. Baumstark-Khan, "Protection of Bacterial Spores in Space, A Contribution to the Discussion on Panspermia," *Origins of Life and Evolution of the Biosphere*, vol. 31, pp. 527–547, 2001.

[223] S. Shimizu, S. Barczyk, P. Rettberg, T. Shimizu, T. Klaempfl, J. L. Zimmermann, T. Hoeschen, C. Linsmeier, P. Weber, G. E. Morfill, and H. M. Thomas, "Cold atmospheric plasma - A new technology for spacecraft component decontamination," *Planetary and Space Sciences*, vol. 90, pp. 60–71, 2014.

[224] W. L. Nicholson, A. C. Schuerger, and M. S. Race, "Migrating microbes and planetary protection," *Trends in Microbiology*, vol. 17, no. 9, pp. 389–392, 2009.

[225] K. Stapelmann, M. Fiebrandt, M. Raguse, P. Awakowicz, G. Reitz, and R. Moeller, "Utilization of Low-Pressure Plasma to Inactivate Bacterial Spores on Stainless Steel Screws," *Astrobiology*, vol. 13, no. 7, pp. 597–606, 2013.

[226] P. Setlow, "Spores of *Bacillus subtilis*: their resistance to and killing by radiation, heat and chemicals," *Journal of Applied Microbiology*, vol. 101, pp. 514–525, 2006.

[227] O. Yardimci and P. Setlow, "Plasma Sterilization: Opportunities and Microbial Assessment Strategies in Medical Device Manufacturing," *IEEE Transactions on Plasma Science*, vol. 38, no. 4, pp. 973–981, 2010.

[228] A. O. Henriques and C. P. Moran, "Structure, Assembly, and Function of the Spore Surface Layers," *Annual Review of Microbiology*, vol. 61, pp. 555–588, 2007.

[229] C. Redmond, L. W. J. Baillie, S. Hibbs, A. J. G. Moir, and A. Moir, "Identification of proteins in the exosporium of *Bacillus anthracis*," *Microbiology*, vol. 150, pp. 355–363, 2004.

[230] L. N. Waller, N. Fox, K. F. Fox, A. Fox, and R. L. Price, "Ruthenium red staining for ultrastructural visualization of a glycoprotein layer surrounding the spore of *Bacillus anthracis* and *Bacillus subtilis*," *Journal of Microbiological Methods*, vol. 58, pp. 23–30, 2004.

[231] E.-M. Lai, N. D. Phadke, M. T. Kachmann, R. Giorno, S. Vazquez, J. A. Vazquez, J. R. Maddock, and A. Driks, "Proteomic Analysis of the Spore Coats of *Bacillus subtilis* and *Bacillus anthracis*," *Journal of Bacteriology*, vol. 185, no. 4, pp. 1443–1454, 2003.

[232] S. J. Todd, J. G. Moir, M. J. Johnson, and A. Moir, "Genes of *Bacillus cereus* and *Bacillus anthracis* Encoding Proteins of the Exosporium," *Journal of Bacteriology*, vol. 185, no. 11, pp. 3373–3378, 2003.

[233] A. Driks, "*Bacillus subtilis* Spore Coat," *Microbiology and Molecular Biology Reviews*, vol. 63, no. 1, pp. 1–20, 1999.

[234] P. J. Piggot and D. W. Hilbert, "Sporulation of *Bacillus subtilis*," *Current Opinion in Microbiology*, vol. 7, pp. 579–586, 2004.

[235] B. Setlow, A. E. Cowan, and P. Setlow, "Germination of spores of *Bacillus subtilis* with dodecylamine," *Journal of Applied Microbiology*, vol. 95, pp. 637–648, 2003.

[236] D. L. Popham, J. Helin, C. E. Costello, and P. Setlow, "Analysis of the Peptidoglycan Structure of *Bacillus subtilis* Endospores," *Journal of Bacteriology*, vol. 178, no. 22, pp. 6451–6458, 1996.

[237] D. L. Popham, M. E. Gilmore, and P. Setlow, "Roles of Low-Molecular-Weight Penicillin-Binding Proteins in *Bacillus subtilis* Spore Peptidogylcan Synthesis and Spore Properties," *Journal of Bacteriology*, vol. 181, no. 1, pp. 126–132, 1999.

[238] T. C. Beaman and P. Gerhardt, "Heat Resistance of Bacterial Spores Correlated with Protoplast Dehydration, Mineralization, and Thermal Adaption," *Applied and Environmental Microbiology*, vol. 52, no. 6, pp. 1242–1246, 1986.

[239] S. Nakashio and P. Gerhardt, "Protoplast Dehydration Correlated with Heat Resistance of Bacterial Spores," *Journal of Bacteriology*, vol. 162, no. 2, pp. 571–578, 1985.

[240] B. Setlow, K. A. McGinnis, K. Ragkousi, and P. Setlow, "Effects of Major Spore-Specific DNA Binding Proteins on *Bacillus subtilis* Sporulation and Spore Properties," *Journal of Bacteriology*, vol. 182, no. 24, pp. 6906–6012, 2000.

[241] G. R. Bender and R. E. Marquis, "Spore Heat Resistance and Specific Mineralization," *Applied and Environmental Microbiology*, vol. 50, no. 6, pp. 1414–1421, 1985.

[242] J. A. Lindsay and W. G. Murrell, "Solution Spectroscopy of Dipicolinic Acid Interaction with Nucleic Acids: Role in Spore Heat Resistance," *Current Microbiology*, vol. 13, pp. 255–259, 1986.

[243] A. Magge, A. C. Granger, P. G. Wahome, B. Setlow, V. R. Vepachedu, C. A. Loshon, L. Peng, D. Chen, Y.-Q. Li, and P. Setlow, "Role of Dipicolinic Acid in the Germination, Stability, and Viability of Spores of *Bacillus subtilis*," *Journal of Bacteriology*, vol. 190, no. 14, pp. 4798–4807, 2008.

[244] P. Setlow, "I will survive: DNA protection in bacterial spores," *TRENDS in Microbiology*, vol. 15, no. 4, pp. 172–180, 2007.

[245] B. Setlow and P. Setlow, "Role of DNA Repair in *Bacillus subtilis Spore Resistance*," *Journal of Bacteriology*, vol. 178, no. 12, pp. 3486–3495, 1996.

[246] P. Fajardo-Cavazos, C. Salazar, and W. L. Nicholson, "Molecular Cloning and Characterization of the *Bacillus subtilis* Spore Photoproduct Lyase (*spl*) Gene, Which Is Involved in Repair of UV Radiation-Induced DNA Damage during Spore Germination," *Journal of Bacteriology*, vol. 175, no. 6, pp. 1735–1744, 1993.

[247] P. Setlow, "Resistance of Spores of *Bacillus* Species to Ultraviolet Light," *Environmental and Molecular Mutagenesis*, vol. 38, pp. 97–104, 2001.

[248] J. A. Jernigan *et al.*, "Bioterrorism-Related Inhalational Anthrax: The First 10 Cases Reported in the United States," *Emerging Infectious Diseases*, vol. 7, no. 6, pp. 933–944, 2001.

[249] T. V. Inglesby *et al.*, "Anthrax as a Biological Weapon, 2002 Updated Recommendations for Management," *The Journal of the American Medical Association*, vol. 287, no. 17, pp. 2236–2252, 2002.

[250] K. Lee, K.-H. Paek, W.-T. Ju, and Y. Lee, "Sterilization of Bacteria, Yeast, and Bacterial Endospores by Atmospheric-Pressure Cold Plasma using Helium and Oxygen," *The Journal of Microbiology*, vol. 44, no. 3, pp. 269–275, 2006.

[251] K. S. Lassen, J. E. Johansen, and R. Grün, "Comparison of Two Radio-Frequency Plasma Sterilization Processes Using Microspot Evaluation of Microbial Inactivation," *Journal of Biomedical Materials Research Part B: Applied Biomaterials*, vol. 78B, no. 1, pp. 189–195, 2005.

[252] P. Muranyi, J. Wunderlich, and M. Heise, "Sterilization efficiency of a cascaded dielectric barrier discharge," *Journal of Applied Microbiology*, vol. 103, pp. 1535–1544, 2007.

[253] A. D. Morris, G. B. McCombs, T. Akan, W. Hynes, M. Laroussi, and S. L. Tolle, "Cold Plasma Technology: Bactericidal Effects on *Geobacillus Stearothermophilus* and *Bacillus Cereus* Microorganisms," *The Journal of Dental Hygiene*, vol. 83, no. 2, pp. 55–61, 2009.

[254] J. Feichtinger, A. Schulz, M. Walker, and U. Schumacher, "Sterilization with low-pressure microwave plasmas," *Surface and Coatings Technology*, vol. 174-175, pp. 564–569, 2003.

[255] S. Hury, D. R. Vidal, F. Desor, J. Pelletier, and T. Lagarde, "A parametric study of the destruction efficiency of *Bacillus* spores in low pressure oxygen-based plasmas," *Letters in Applied Microbiology*, vol. 26, pp. 417–421, 1998.

[256] T. G. Klämpfl, *Cold atmospheric plasma decontamination against nosocomial bacteria*. PhD thesis, Technische Universität München, Fakultät für Medizin, Institut für Pathologie, January 2014.

[257] C. R. Wilke and C. Y. Lee, "Estimation of Diffusion Coefficients for Gases and Vapors," *Industrial and Engineering Chemistry*, vol. 47, no. 6, pp. 1253–1257, 1955.

[258] J. H. Rohling, J. Shen, C. Wang, J. Zhou, and C. E. Gu, "Determination of binary diffusion coefficients of gases using photothermal deflection technique," *Applied Physics B - Lasers and Optics*, vol. 87, pp. 355–362, 2007.

[259] M. Hähnel, T. von Woedtke, and K.-D. Weltmann, "Influence of the Air Humidity on the Reduction of *Bacillus* Spores in a Defined Environment at Atmospheric Pressure Using a Dielectric Barrier Discharge," *Plasma Processes and Polymers*, vol. 7, pp. 244–249, 2010.

[260] U. Schnabel, M. Andrasch, K.-D. Weltmann, and J. Ehlbeck, "Inactivation of Vegetative Microorganisms and *Bacillus atrophaeus* Endospores by Reactive Nitrogen Species (RNS)," *Plasma Processes and Polymers*, vol. 11, pp. 110–116, 2014.

[261] G. Kamgang-Youbi, J.-M. Herry, T. Meylheuc, J.-L. Brisset, M.-N. Bellon-Fontaine, A. Doubla, and M. Naitali, "Microbial inactivation using plasma-activated water obtained by gliding electric discharges," *Letters in Applied Microbiology*, vol. 48, pp. 13–18, 2008.

[262] M. J. Pavlovich, H.-W. Chang, Y. Sakiyama, D. S. Clark, and D. B. Graves, "Ozone correlates with antibacterial effects from indirect air dielectric barrier discharge treatment of water," *Journal of Physics D: Applied Physics*, vol. 46, p. 145202, 2013.

[263] Y. J. Jung, B. S. Oh, and J.-W. Kang, "Synergistic effect of sequential or combined use of ozone and UV radiation for the disinfection of *Bacillus subtilis* spores," *Water Research*, vol. 42, pp. 1613–1621, 2008.

[264] K. Oehmigen, M. Hähnel, R. Brandenburg, C. Wilke, K.-D. Weltmann, and T. von Woedtke, "The Role of Acidification for Antimicrobial Activity of Atmospheric Pressure Plasma in Liquids," *Plasma Processes and Polymers*, vol. 7, pp. 250–257, 2010.

[265] P. M. Foegeding, "Ozone inactivation of *Bacillus* and *Clostridium* spore populations and the importance of the spore coat to resistance," *Food Microbiology*, vol. 2, pp. 123–134, 1985.